Long Term and Short Term Deflection of GFRP Prestressed Concrete Slabs

by

Mahendra Singh

A Thesis submitted to the Faculty of Graduate Studies of

The University of Manitoba

in partial fulfilment of the requirements of the degree of

MASTER OF SCIENCE

Department of Civil Engineering

University of Manitoba

Winnipeg, Manitoba, Canada

Abstract

This thesis investigates the performance of GFRP pretensioned concrete slabs and compares their flexural behaviour with GFRP reinforced and steel prestressed concrete slabs. A total of 12 slabs were cast in this program. The slab mid-span deflections are theoretically predicted and the results indicate that the short-term response of GFRP prestressed concrete slabs can be predicted well by the existing methods. Long-term deflection behaviour has been estimated using the Age Adjusted Effective Modulus Method by incorporating three creep and shrinkage models. A large influence of creep and shrinkage models on the theoretical determination is observed and the use of long term multipliers is not suitable for GFRP prestressed concrete members. The slabs were instrumented for long-term monitoring using strain gauges and fibre-optic sensors. It was concluded that the electrical strain gauges can be successfully used for long-term strain monitoring.

Acknowledgements

I gratefully acknowledge the guidance provided by my advisor Dr. Dagmar Svecova in achieving the conducive results for this project. The proactive decisions resulting from her knowledge and foresight had valuable contributions in the fulfillment of my master's degree. I am also thankful for her patience and the confidence she has shown in me.

I would like to acknowledge the Department of Jobs and the Economy Manitoba for their financial support obtained through the ISIS Canada Resource Centre. I would also like to thank Specialty Construction Products Ltd. and Lafarge Winnipeg Precast for becoming partners in this project.

I would like to express my gratitude towards Mr. David Donald from Lafarge Winnipeg and Mr. Tom Berry, Mr. Paul Champagne, Mr. Muhamed Arapovic and Mr. Scott Tye from the Lafarge precast plant for their co-operation in this project.

I would like to thank Dr. Dean McNeill and Dr. Douglas Thomson for giving their time to me in understanding the response of electrical strain gauges.

I would like to express my gratitude to Dr. Hugues M. Vogel, Ms. Evangeline Murison and Mr. Mirpayam Nabipaylashgari for patiently guiding me through the process of instrumentation.

The technical support from Mr. Chad Klowak, the laboratory manager of the W.R. McQuade Structures Laboratory and the technicians Mr. Brendan Pachal and Mr. Grant Whiteside is gratefully acknowledged.

I would like to thank my family for their understanding and patience. The constant support provided by my parents, brother, sisters, and my wife had inspired me to successfully complete this project.

Table of Contents

List of Tables

List of Figures

List of Symbols

A_g = Gross cross-sectional area of member

A_t = Transformed area of uncracked section

A_n = Net cross-sectional area of concrete

A_p = Total area of prestressing rebars/tendons

$C_0(t,t_0)$ = Compliance function for basic creep

$C_d(t,t_0,t_c)$ = Additional compliance function for drying creep

CR = Prestress loss due to creep (MPa)

e = Eccentricity of reinforcement of uncracked section

e_{pn} = Eccentricity of rebars/strands with respect to net cross-sectional area

E_c = Modulus of elasticity of concrete

E_{ci} = Modulus of elasticity of concrete at prestress transfer

E_{ct0} = Modulus of elasticity of concrete at the time of loading

E_p = Modulus of elasticity of prestressed reinforcement

E_s = Modulus of elasticity of steel

E_{gfrp} = Modulus of elasticity of GFRP

f_r = Modulus of rupture of concrete

f'_c = Compressive strength of concrete (MPa)

f_{cgp} = Stress in concrete at the C.G. of reinforcement just after the transfer of prestress

f_{pu} = Ultimate strength of prestressing tendons (MPa)

f_{st} = Stress in prestressing steel at transfer (MPa)

f_{sj} =Jacking stress in prestressing steel (MPa)

f_{py} =Yield strength of prestressed steel; $0.9f_{pu}$ for low relaxation strands (MPa)

I_e = Effective moment of inertia

I_g = Gross moment of inertia of the cross-section

I_{cr} = Moment of inertia of cracked section about neutral axis

I_{crp} = Moment of inertia of cracked prestressed section about neutral axis

I_n = Moment of inertia of net concrete section

I_t = Transformed moment of inertia of uncracked section

$J(t,t_0)$ = Compliance at time t

L = Span of member

L_{ucr} = Uncracked length of the member measured from the support

m_x = Bending moment due to unit load at the point of interest

M_{dec} = Decompression moment

M_x = Bending moment along the span

M_a = Maximum bending moment due to the applied load along the span

M_{sw} = Maximum bending moment due to self weight of member

M_{cr} = Bending moment at which the tensile stresses in concrete exceeds the modulus of rupture due to self weight plus applied load

M_{Pcr} = Bending moment at which the tensile stresses in concrete exceeds the modulus of rupture due to applied load

P_e = Total effective Prestressing force after transfer

P_i = Total prestressing force in rebar/tendon before transfer of prestress

P_c = Total prestressing force after time dependent losses in rebar/tendons

q1 = Instantaneous strain due to unit stress at a time of about 10 -9 second

REL_1 = Loss in prestress due to relaxation before the transfer of prestress (MPa)

REL_2 = Loss in prestress due to relaxation after the transfer of prestress (MPa)

REL_g = Relaxation in GFRP rebar

SH = Prestress loss due to shrinkage (MPa)

t_0 = Age of concrete in days at the time of loading

t_c = Age of concrete at the end of moist curing

t = Age of concrete in days

y_{bt} = Distance between bottom concrete face and centroid of transformed section

y_{bg} = Distance between bottom concrete face and centroid of gross section

α_{ESG} = CTE of Material used for thermal output by manufacturer

α_R = CTE of Reinforcement

β_d = Coefficient of reduction in deflection calculations

β_c = Coefficient that describes the development of creep with time

δ = Deflection at the point of imaginary unit load

$\varepsilon_{sh}(t,t_c)$ = Shrinkage strain at the age of 't' days

ε_{abs} = Absolute Strain

ε = Measured Strain

ε_{app} = Thermal Output of ESG from Manufacturer

ξ = Time dependent factor for sustained load from ACI 318M-11

ρ_f = Reinforcement ratio for GFRP

ρ_{fb} = Reinforcement ratio for balanced section

σ_{si} = Initial prestressing stress in GFRP (MPa)

$\Delta_{(cp+sh)}$ = Additional deflection due to creep and shrinkage under sustained load (mm)

$(\Delta_i)_{sus}$ = Immediate deflection due to sustained load (mm)

Δf_{pES1} = Elastic shortening loss at the transfer of prestress

$\Delta\sigma$ = Loss due to elastic shortening

$\phi(t,t_0)$ = Creep coefficient at time t

ϕ_u = Ultimate creep coefficient for the standard conditions

ϕ_0 = Notional creep coefficient

Ω = Ohm

List of Abbreviations

AAEMM	= Age-Adjusted Effective Modulus Method
ACI	= American Concrete Institute
ASTM	= American Society for Testing and Materials
CAN/CSA	= Canadian Standards Association
CEB	= Comité Euro-International du Béton (Euro-International Concrete Committee)
CFRP	= Carbon Fiber Reinforced Polymer
CTE	= Coefficient of Thermal Expension
ESG	= Electrical Strain Gauge
Eq	= Equation
FRP	= Fiber Reinforced Polymer
FOS	= Fibre Optic Sensor
GFRP	= Glass Fiber Reinforced Polymer
ISIS	= Intelligent Sensing for Innovative Structures
LVDT	= Linear Variable Displacement Transducer
NA	= Neutral Axis
NTS	= Not to scale
SHM	= Structural Health Monitoring
STC	= Self Temperature Compensation

1. Introduction

1.1. General

The use of GFRP in concrete structures has a promising future considering its durability under natural environmental conditions (Mufti et. al. 2007) and makes it a suitable substitute to steel reinforcement. However, GFRP has two major design limitations, first is its low modulus of elasticity and second is the rupture of GFRP bars at sustained high stress levels (Somes 1963). The low modulus of elasticity of GFRP reduces the cracked stiffness of the member in comparison with other reinforcing materials such as steel or CFRP. As a result the member undergoes large deflections and experiences wider cracks. This limitation has a more adverse effect on structures with thinner cross-sections. Also, in the long term GFRP reinforced members crack at the tension face at much lower stress values than obtained from the modulus of rupture, due to shrinkage restraint stresses (Scanlon and Murray 1982, Gilbert 1999, Scanlon and Bischoff 2008) and the cracked zone progressively increases with time. The cumulative effect of the increase in the number of cracks with wider crack widths results in large deflections which increase with age.

This serviceability issue can be handled by increasing the initial stiffness of the member with the help of the right amount of the total prestressing force to compensate for the deflection due to dead weight. This increase in stiffness will not only reduce the long term deformation, but also will not allow the progressive growth of cracks in numbers and extent (by keeping the tensile stresses in concrete much below the modulus of

rupture) and the member can satisfy the permissible limits prescribed in the governing codes against the time dependent deformations.

1.2. Objectives and Scope

Earlier in finding the solution to the rapid deterioration of concrete slabs supporting the markers for Veterans Affairs Brookside Cemetery, Winnipeg, Canada, (Figure 1-1) the steel prestressed slabs were replaced by GFRP reinforced slabs to address the issue of steel corrosion in harsh environmental conditions and increasing the service life of slab and marker assemblies (Mufti et. al. 2004).

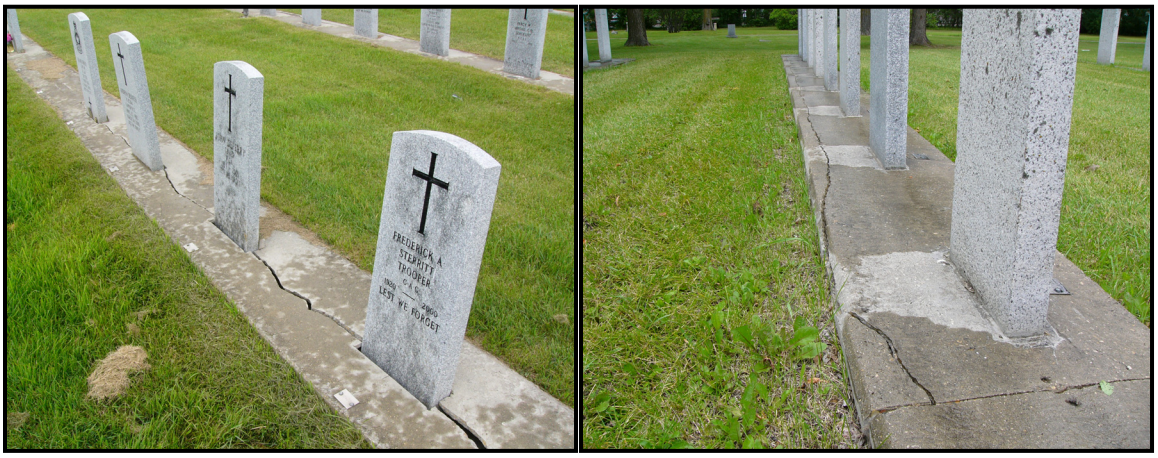

Figure 1-1 Deterioration of Existing Brookside Cemetery Slabs

A field trial slab was constructed that included a structural health monitoring system. Over a period of 30 months of observation the slab had undergone excessive deflection (Mufti et. al. March 2007) as shown in Figure 1-2. The maximum deflection permitted by CAN/CSA-S806-12 is $l_n/240$, however the deflection observed was much beyond the permissible limit. This failure of serviceability is due to incorrect support conditions in the field by not placing the gravel bed below the slab, that caused the slab to crack prematurely, low modulus of elasticity of the GFRP rebars and the shallow depth of the slab.

To satisfy the serviceability requirements the following options were considered:

- Meet the minimum depth Criteria as per CAN/CSA S806-12
- Increasing the amount of reinforcement
- Modifying the support conditions
- Changing the design philosophy to prestressed concrete

Since the depth is restricted by the design requirement, the best way to increase the stiffness of slab is to prestress the GFRP rebars. Prestressing will not only help in generating an upward camber, it will also decrease the stresses responsible for deflection due to creep by reducing the effect from moment due to dead weight. In addition the effect of shrinkage restraint stresses can be reduced by properly including the amount of total prestressing force.

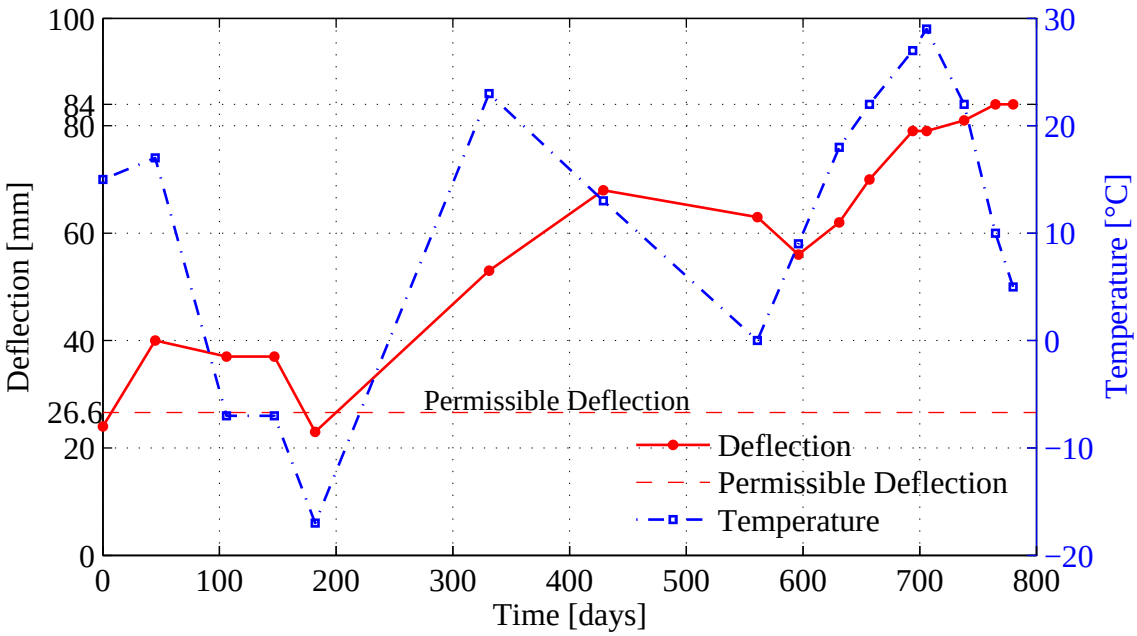

Figure 1-2 SHM of Field Trial Beam at Veteran Affairs Brookside Cemetery; Mufti at al. (2007)

Thus to study the effect of creep and shrinkage on the prestressed GFRP slabs in comparison with non-prestressed slabs and slabs prestressed with steel, a research

program has been developed to gather the long term deflection of slabs and strains in the rebars/strands. One additional set of slabs (four slabs) was also constructed and tested until failure to obtain the short term response of the slabs.

1.3. Research Significance

So far the research and field applications conducted in the field of prestressing with GFRP has been done with the prestressing level from 40% to 60% of the ultimate strength of tendon/rebar. This limit is much beyond the prescribed 25% limit mentioned in Canadian code CSA S6-06. Due to the creep rupture of GFRP rebar under sustained stress, the lower stress limit adopted by the CSA S6-06 is well justified. Thus it becomes essential to study the behaviour of concrete members close to the prescribed limits and to validate these limits mentioned in the code. The verification of the prescribed limit of prestressing level of GFRP as an internal reinforcement will be checked through long term deflection, loss in prestressing strain, degradation of GFRP bar at the end of experimental program and change in short term load-deflection response after 10 years of service life. Another important piece of information missing from the code is the relaxation of GFRP, and very limited data is available in the literature.

The long term observation of these prestressed slabs is also aimed to study the suitability of general purpose strain gauges for long term strain monitoring in GFRP reinforcement/tendons.

There are some well known creep and shrinkage models available for long term analysis. This research also checks the suitability of these models with the age adjusted effective modulus method for predicting the behaviour of pretentioned GFRP reinforced members.

This research can also be used to observe the effects of shrinkage restraint stresses in the reduction of cracking moment with time for slabs with reinforcement less than 1%.

The test results obtained from the destructive testing on one set of slabs will check the accuracy of the estimation of deflection through the effective moment of inertia approach mentioned in the codes.

1.4. Organization of Thesis

The thesis has been subdivided into five sections/chapters and the detailed test results and calculations are presented in appendixes.

The first chapter discusses the significance and importance of this research and also briefly describes the work done in the research.

Chapter two is devoted for the previous research performed in the area of prestressing with GFRP. The chapter describes the methods employed to obtain the theoretical prediction of the long term behaviour of slabs. The calculated results are used later on to compare with the experimental values.

Chapter three describes the details of experiments performed, including the instrumentation and DAQ. In this chapter the limitations of the instrumentation and DAQ is also been discussed to understand the accuracy of results.

Chapter four demonstrates the comparison between the theoretical and experimental results. Also, the possible causes of the deviation from the test results are discussed.

Chapter five summarizes the findings of this research and suggests future possibilities with GFRP prestressing.

There are three appendixes in this thesis Appendix-A provides the results obtained from testing concrete and GFRP. Appendix-B contains the test results for short term and long term testing of slabs including the prestressing data. Appendix-C describes the procedure of theoretical analysis.

2. Literature Review

Long term observations in the area of GFRP prestressed beams/slabs is rare and mostly the research is done on the GFRP reinforced members. The research in the area of FRP prestressing is mostly limited to CFRP and AFRP. Since CAN/CSA S6-06 permits prestressing with GFRP, thus it become essential to study the behaviour of a structural member prestressed with GFRP with different level of prestressing for its long term behaviour.

The idea of prestressing with GFRP is not new and in the past some researchers implemented it in real life structures as discussed in section 2.1

2.1. Prestressing with GFRP

Nearly half a century ago efforts were started to study the possibility of using GFRP as a prestressing material. Some of the well known efforts are described in the following literature review.

2.1.1. Laboratory Investigations

Somes (1963) tested eight beams prestressed with resin-bonded glass-fibre tendons to failure. The prestress level in the tendons was kept between 40 to 50% of ultimate strength, thus the number of tendons was kept as a variable to change the prestressing force, while another variable considered was the depth of the beams. Out of eight beams, three failed prematurely within a few days and the reason provided was surface damage during compaction of the concrete. Two point loading was employed to test the beams with dial gauges for deflection measurement and mechanical strain gauges to measure the

strains on the concrete surface. The results obtained from the tests were compared with the theoretical calculations using the strain compatibility approach. The author encountered a few issues regarding the anchorage, susceptibility to surface damage and rupture of glass fibre tendons.

In 1966, the United States Army Corps of Engineers, at Waterways Experimental Station, Vicksburg, Mississippi published a report authored by Wines et al. (1966). The report describes the experimental investigation on prestressing with glass fibre tendons for concrete members. In the experiments, concrete beams pretentioned with glass fibre are tested in flexure until failure. In addition the author recommends the use of expanding cement for anchoring the tendons for prestressing them. In this report the author mentioned that long-duration load tests had started and will be published in the next report, however we were unable to get any details regarding the next report.

Taerwe et. al. (1992) conducted an experiment at Magnel Laboratory of Ghent University on three 2 m long and one 20 m long beams post-tensioned with glass fibre tendons prestressed to 49.3 % of 1520 MPa (total prestressing force 66 kN) and 49.0% of 1606 MPa (total prestressing force 660 kN) respectively through the tendon trade name Polystal bar. The glass fibre tendons were grouted after prestressing except in one 2 m long beam and all were tested to failure with two point loading. All the beams were reinforced with steel in addition to glass fibre tendons, the author reported 60% contribution of reinforced steel in the total capacity of the beams.

Sen et al.(1992) reported a research project sponsored by the Florida Department of Transportation in cooperation with the U.S. Department of Transportation on the Feasibility of Fiberglass Pretensioned Piles in a Marine Environment. In this study the

suitability of concrete members pretensioned with glass fiber tendons for short term, long term and impact response was examined. The research included 63 specimens of beams, columns and piles pretensioned with S-2 fibre glass and steel.

In the static beam tests Sen et al.(1992), the experimental and nonlinear FEM study was performed to determine the response of prestressed beams pretentioned with three 9.5 mm S-2 glass/epoxy strands and compared with the steel prestressed beams with equal amount of total prestressing force. The steel and fibre glass reinforcement were jacked to 80% and 50% respectively. The research compares the elastic, ultimate response, ductility and checks the possibility of applying the flexure design rules in theoretical analysis. From the experiment the author observed the same precracking response for all beams however post cracking stiffness was lower in glass fibre beams while the failure characteristics and the failure load were similar.

Sen et al.(1992) did the fatigue study on separate set of beams, loaded from 40% to 60% of ultimate capacity subjected to 2 million cycles at 3 Hz. The glass fibre strands were pretensioned with a minimum of 42% and a maximum of 56% of ultimate tensile strength. The surviving beams were than statically tested to failure with only slightly less ultimate capacity.

Sen et al.(1992) also performed the durability tests with an interval of three months up to 20 months. Half of the studied beams were precracked along the top and bottom faces and placed in a 15% salt solution with wet and dry cycle exposure, the other half were controlled specimens for studying the difference between cracked and uncracked specimens. For cracked specimens the effectiveness was lost after 6 months and for uncracked specimens this period was 15 months.

Columns were also tested by Sen et al.(1992) under axial and eccentric loading and the results were similar to the equivalent steel prestressed columns.

Sen et al.(1992) did the tests on pretensioned fibre glass piles by driving the piles through drop hammer under normal driving conditions the glass fibre pretensioned piles responded well. However, when the drop height was increased some damage was recorded in the fibre glass ties.

2.1.2. Field Applications

In addition to the laboratory tests, prestressing with GFRP was also implemented in the field. Some of the activities are categorized below on the basis of their geographical locations. In Europe the following structures were built.

- Lunen'sche-Gasse Bridge, Germany (1980): The single span experimental bridge uses Polystal GFRP unbonded tendons for prestressing.
- Ulenberg-Strasse Bridge, Dusseldorf, Germany (1986): A highway bridge prestressed with glass fibre bars (Polystal) have span lengths of 21.3 m and 25.6 m with service tensile loads of 0.47 P_u.
- Marienfelde Bridge, Berlin, Germany (1988): A two span bridge was prestressed with external glass fiber bars.
- Schiessbergstrasse Bridge, Leverkusen, Germany (1991): A three span bridge at Leverkussen, Germany was prestressed with glass fibre tendons.
- Notsch Bridge, Austria (1991): This three span bridge was post-tensioned with Polystal glass fibre tendons.

Some of the North American structures are listed below.

- Rapid City Bridge, South Dakota (1992): One third of the 9 m span post-tensioned bridge uses GFRP cables to prestress the deck slab supported on three longitudinal girders. The final prestress level reported was 0.5 P_u
- Pile caps of waterfront structure; Port Hueneme, California (1994): The pile caps were post-tensioned with GFRP cables

In Japan the pre-tensioning with GFRP was performed on the following structure.

- Iwafune Golf Club cable stayed-bridge, Japan (1992): The birdge was partially prestressed with GFRP and CFRP with initial prestressing force of 0.3 P_u.

2.2. Analysis Guidelines

The theoretical determination of deflection is obtained by the method of virtual work. Once the curvature function is formulated along the span of the member, the deflection can be determined by integrating the curvature along the span using Eq 2-1.

$$\delta = \int_0^L \frac{m_x \, M_x}{E_c \, I_e} \, dx \qquad \text{Eq 2-1}$$

Where, L is the span of member, δ is the deflection at the point of imaginary unit load, m_x is the bending moment due to unit imaginary load at the location of δ, M_x is the bending moment along the span, E_c is the modulus of elasticity of concrete, and I_e is the effective moment of inertia of cross-section.

The analysis of uncracked section for GFRP Prestressed, GFRP reinforced and steel prestressed slabs is based on the mechanics theory with little or no difference between different code procedures.

With the occurrence of discrete cracking, the tension in the reinforcing bar between two cracks is shared by concrete through the bond between concrete and reinforcement. This

phenomenon is known as tension stiffening. Different codes have adopted different procedures to account for the effect of tension stiffening through effective moment of inertia and also the difference is in the application of effective moment of inertia along the span. The code procedures are discussed in the next section.

The concept of effective moment of inertia was introduced by Branson (1965) and was empirically derived for non-prestressed elements with steel reinforcement; the approach can be extended to the prestressed/partially prestressed members by introducing decompression moment in the equation of effective moment of inertia by reducing the cracking moment and applied moment by decompression moment. The decompression moment (M_{dec}) is the moment required to produce zero stresses at extreme compression fibre (Naaman et al. 1979, Siriaksorn et al. 1979). Nawy et al. (1977) describes decompression moment as the moment required to eliminate the stresses generated in concrete at the level of rebars/tendons. In this thesis the definition provided by Naaman et al. (1979) and Siriaksorn et al. (1979) has been adopted. The decompression moment can be calculated by the following equation.

$$M_{dec} = P_e\, e + \frac{P_e\, I_t}{A_t\, y_{bt}} \qquad \text{Eq 2-2}$$

Where, M_{dec} is decompression moment, P_e is the total effective prestressing force after transfer, e is eccentricity of reinforcement of uncracked section, I_t is the transformed moment of inertia of uncracked section, A_t is transformed area of uncracked section, y_{bt} is the distance between bottom concrete face and centroid of transformed section.

A few historically adopted methods to apply the decompression moment are compared by Rao and Dilger (1992) to determine their suitability in terms of computational effort and accuracy of results.

Once the effective moment of inertia is modified with decompression moment, the concept of determination of deflection remains the same for prestressed and non-prestressed members.

Intelligent Sensing for Innovative Structures (ISIS Canada) and American Concrete Institute (ACI) recommends determining the maximum moment along the span of simply supported beam (or between the points of contraflexure), the maximum moment obtained will be used to determine the cracked properties of the section, which in turn is used to calculate the cracked moment of inertia. Thus the variation of effective moment of inertia along the span is a function of external moment alone for that span at the point of maximum moment. The corresponding deflection can be obtained by integrating the curvature as illustrated in Eq 2-1.

The cross-sectional analysis has been done by strain compatibility approach with the assumption of plane section before and after bending remains plane and by assuming perfect bond between reinforcement and concrete. For short term (when the member is loaded up-to failure) analysis the experimental stress strain results obtained from the cylinder test are used in cross-sectional analysis by translating the relation to cubic form. The stress response of GFRP is linear up to failure and the modulus of elasticity was obtained from the tension tests performed on four GFRP rebars in accordance with CAN/CSA S806-12.

For service load conditions a linear variation of stress versus strain is assumed for concrete, in case of steel strands at a prestress level of 65 percent the same assumption is also valid since the variation in stresses over the period of time is not significant enough to change the modulus of elasticity of steel strands.

2.3. Deflection Calculation Approaches

Short term and long term deflection includes the deflection due to camber, self-weight plus external loading, creep, shrinkage and relaxation of rebars/strands. In this section the calculations of these deflections are explained.

In the estimation of time dependent deflection through long term multipliers Gross et al. (2003) observed that the results obtained from these estimates do not address the additional deformation due to the occurrence of cracks due to shrinkage and temperature effects. Thus in such cases the estimated deflection considerably underestimated the observed deflections.

Mota et al.(2006) analysed 197 beams and slabs to determine the reliability of deflection estimation through available approaches for FRP reinforced members. It was concluded that the accuracy of deflection is highly dependent on the cracking moment which in turn depends on modulus of rupture. It was found that provisions of CSA A23.3 and CEB-FIP MC-90 provide accurate results for estimating the values of modulus of rupture. The study concluded that as the applied moment approaching cracking moment, the prediction of deflection between individual methods starts diverging from the experimental results. The deflection estimates then improve for higher moments.

2.3.1. CAN/CSA S806-12

The code does not permit the use of GFRP for prestressing, however under service load conditions it permits the stresses in GFRP rebars to go upto 25% of their ultimate strength.

The deflection is determined on the bases of integration of curvature along the span of a structural member. For the calculation of the deflection of a cracked member the code suggests to consider a trilinear variation of curvature. The trilinear variation consists of three slopes; first, in uncracked zone the curvature is calculated from transformed moment of inertia; second, the continuity between the cracked and uncracked section is joined by a straight vertical line; and third, the cracked section curvature is obtained from cracked moment of inertia. To determine the deflection of a simply supported member the trilinear variation of curvature can be formulated using virtual work method as shown in Eq 2-3

$$\delta = 2\int_{0}^{L_{ucr}} \frac{m_x\, M_x}{E_c\, I_t}\, dx + 2\int_{L_{ucr}}^{\frac{L}{2}} \frac{m_x\, M_x}{E_c\, I_{cr}}\, dx \qquad \text{Eq 2-3}$$

Where, L_{ucr} is the uncracked length of the member measured from the support, I_{cr} is the moment of inertia of cracked section about neutral axis.

It shall be noted that the determination of cracked moment of inertia at one particular load is based on the maximum moment along the span, thus the cracked moment of inertia has been considered constant in the region (L - $2 \times L_{ucr}$) where external moment is greater than cracking moment. Also the decompression moment is not applicable here due to the consideration of trilinear variation of curvature.

For long term analysis CAN/CSA S806-12 suggests, in the absence of detailed analysis that the time dependent multipliers shall be used to predict the deformation of non-prestressed flexural members.

The long term deformation of prestressed members shall be calculated using the change in stresses in concrete and reinforcement due to creep and shrinkage of concrete and relaxation of reinforcement. This implies that the age adjusted effective modulus method can be used to determine the long term deformation of a structural member prestressed with FRP.

2.3.2. CAN/CSA S6-06

As per clause 16.8.5.2 of Canadian Highway Bridge Design Code, CSA S6-06 permits the use of GFRP for prestressing with the permissible jacking stress of 29 percent, and transfer stress of 25 percent of the ultimate strength.

2.3.3. ISIS Approach

The estimation of deflection before cracking is obtained using linear elastic analysis through transformed moment of inertia. After the occurrence of cracks the deflection for non-prestressed members is obtained through the effective moment of inertia approach on the bases of work done by Mota et al. (2006). The suggested effective moment of inertia is given in Eq 2-4

$$I_e = \frac{I_t I_{cr}}{I_{cr} + \left(1 - 0.5\left(\frac{M_{cr}}{M_a}\right)^2\right)(I_t - I_{cr})} \qquad \text{Eq 2-4}$$

Where, M_{cr} is the bending moment at which the tensile stresses in concrete exceeds the

modulus of rupture of concrete, M_a is the maximum bending moment due to the applied load along the span.

The approach of calculating the effective moment of inertia can be extended for prestressed members by the incorporation of decompression moment. The modified effective moment of inertia is given by Eq 2-5.

$$I_e = \frac{I_t I_{cr}}{I_{crp} + \left(1 - 0.5\left(\frac{M_{cr} - M_{dec}}{M_a - M_{dec}}\right)^2\right)\left(I_t - I_{crp}\right)} \quad \text{Eq 2-5}$$

Where, I_{crp} is moment of inertia of cracked prestressed section about neutral axis.

The deflection of the flexural member is predicted through Eq 2-6

$$\delta = 2\int_0^{\frac{L}{2}} \frac{m_x\, M_x}{E_c\, I_e}\, dx \quad \text{Eq 2-6}$$

For long term deflection ISIS Design Manual 5 (2008) recommends the use of modifiers suggested by Currier(1995). However the manual suggests prestressing with CFRP & AFRP only, thus the multipliers for GFRP are absent.

2.3.4. ACI Approach

The ACI method of determination of deflection for cracked sections addresses the effect of tension stiffening based on Branson's equation of effective moment of inertia. As per ACI 440.1R the effective moment of inertia for non-prestressed GFRP reinforced beam can be obtained from Eq 2-7

$$I_e = \left(\frac{M_{cr}}{M_a}\right)^3 \beta_d\, I_g + \left[1 - \left(\frac{M_{cr}}{M_a}\right)^3\right] I_{cr} \leq I_g \quad \text{Eq 2-7}$$

Where, β_d is coefficient of reduction, for non-prestressed FRP reinforced members and can be calculated from Eq 2-8, I_g is gross moment of inertia of the cross-section.

$$\beta_d = \frac{1}{5}\left(\frac{\rho_f}{\rho_{fb}}\right) \leq 1.0 \qquad \text{Eq 2-8}$$

Where, ρ_f is the reinforcement ratio for GFRP, ρ_{fb} is reinforcement ratio for balanced section.

For prestressed GFRP members, the deflection as per ACI 440.4R-04 is given by Eq 2-9. It should be noted that the formula written below is modified with the decompression moment.

$$I_e = \left(\frac{M_{cr} - M_{dec}}{M_a - M_{dec}}\right)^3 \beta_d \, I_g + \left[1 - \left(\frac{M_{cr} - M_{dec}}{M_a - M_{dec}}\right)^3\right] I_{crp} \leq I_g \qquad \text{Eq 2-9}$$

Where β_d for members prestressed with FRP shall be calculated from Eq 2-10

$$\beta_d = 0.5 \times \left[\frac{E_p}{E_s} + 1\right] \leq 1.0 \qquad \text{Eq 2-10}$$

Where, E_p is modulus of elasticity of prestressed reinforcement, E_s is modulus of elasticity of steel.

The code adopt the same fundamental approach in the calculation of deflections as used for steel reinforced members with an additional reduction coefficient β_d accounted for low modulus of elasticity of FRP material to consider the lesser degree of tension stiffening.

The deflection of the flexural member is predicted through the following Eq 2-11

$$\delta = 2\int_0^{\frac{L}{2}} \frac{m_x \, M_x}{E_c \, I_e} \, dx \qquad \text{Eq 2-11}$$

For additional deformations due to long term effects from creep and shrinkage ACI 440.1R recommends to use the modified factors used in ACI 318 based on the results obtained from Brown (1997) and Vijay et al. (1998) and is determined from Eq 2-12.

$$\Delta_{(cp+sh)} = 0.6\,\xi\,(\Delta_i)_{sus} \qquad \text{Eq 2-12}$$

Where, $\Delta_{(cp+sh)}$ is the additional deflection due to creep and shrinkage under sustained load, $(\Delta_i)_{sus}$ is the immediate deflection due to sustained load, ξ is time dependent factor for sustained load and can be obtained from ACI 318M-11.

2.3.5. Modified Bischoff's Method

Bischoff and Gross (2011) suggested a closed form solution to account for the changing stiffness of the member due to the change in the external loading which is important to consider for the slabs with low reinforcement ratio.

The deflection equation considers two separate moments of inertia, gross moment of inertia for the uncracked span and effective moment of inertia for cracked region. The effective moment of inertia for cracked span is given by the following Eq 2-13

$$I_e = \frac{I_{cr}}{1 - \left(1 - \frac{I_{cr}}{I_g}\right)\left(\frac{M_{cr}}{M_a}\right)^2} \leq I_g \qquad \text{Eq 2-13}$$

Eq 2-13 can be modified by including decompression moment for prestressed GFRP/Steel reinforced members and is represented below in Eq 2-14

$$I_e = \frac{I_{crp}}{1 - \left(1 - \frac{I_{crp}}{I_g}\right)\left(\frac{M_{cr} - M_{dec}}{M_a - M_{dec}}\right)^2} \leq I_g \qquad \text{Eq 2-14}$$

Now the following integral in Eq 2-15 can be used to obtain the deflection for simply supported member as per the modified Bischoff's approach

$$\delta = 2\int_{0}^{L_{ucr}} \frac{m_x\, M_x}{E_c\, I_g}\, dx + 2\int_{L_{ucr}}^{\frac{L}{2}} \frac{m_x\, M_x}{E_c\, I_e}\, dx \qquad \text{Eq 2-15}$$

To avoid this computational effort, Bischoff and Gross (2011) also proposed the closed form solution by including the integration factor for some standard cases of boundary conditions and type of loading. However in this thesis the deflections have been obtained from the integral approach since both will lead to the same final result.

2.4. Cracking Moment

The cracking moment in the analysis has been adopted as per the suggestion from the study performed by Mota et al.(2006) and is given by the Eq 2-16 below

$$M_{cr} = f_r \times \frac{I_g}{y_{bt}} \qquad \text{Eq 2-16}$$

Modulus of rupture of concrete (normal density concrete) is obtained from Eq 2-17

$$f_r = 0.6 \times \sqrt{\mathrm{f'}_c} \qquad \text{Eq 2-17}$$

Where, f_r is modulus of rupture of concrete and f'_c is compressive strength of concrete.

2.5. Camber

Both over and under estimation of the camber is not preferred due to its direct linkage to the prestress losses. In calculating the camber the main influencing factors are total prestressing force, self-weight of the member and support conditions. The camber can be calculated from the standard structural analysis techniques such as virtual work method, moment area theorems or others. In this thesis virtual work approach is used.

2.6. Losses

2.6.1. Elastic Shortening Loss

Loss due to elastic shortening ($\Delta\sigma$) can be obtained from the following Eq 2-18 considering gross-sectional properties.

$$\Delta\sigma = \frac{P_i}{A_g} + \frac{P_i\, e^2}{I_g} - \frac{M_{sw}\, e}{I_g} \qquad \text{Eq 2-18}$$

Where, P_i is total prestressing force in rebar/tendon before transfer of prestress, M_{sw} is the maximum bending moment due to self weight of member, A_g is gross cross-sectional area of member.

The above relation determines the loss due to prestressing with acceptable degree of error.

An exact calculation of loss of prestress due to elastic shortening can be obtained by solving two inter dependent equations Eq 2-19 and Eq 2-20. These equations were derived from strain compatibility between reinforcement and concrete, and equilibrium of forces (Al-Omaishi et al. 2009).

Eq 2-19 is obtained from the assumption of compatibility of strains between reinforcement and concrete.

$$\frac{\Delta f_{pES1}}{E_p} = \frac{f_{cgp}}{E_{ci}} \qquad \text{Eq 2-19}$$

Where, Δf_{pES1} is elastic shortening loss at the transfer of prestress, E_{ci} is Modulus of elasticity of concrete at prestress transfer, f_{cgp} is Stress in concrete at the C.G. of reinforcement just after the transfer of prestress.

Eq 2-20 is derived from the equilibrium of forces across the cross-section with the help of classical elastic analysis.

$$f_{cgp} = \left(P_i - A_p \Delta f_{pES1}\right)\left(\frac{1}{A_n} + \frac{e_{pn}^2}{I_n}\right) - \left(\frac{M_{sw} e_{pn}}{I_n}\right) \qquad \text{Eq 2-20}$$

Where, A_p is total area of prestressing rebars/tendons, A_n is net cross-sectional area of concrete, e_{pn} is eccentricity of rebars/strands with respect to net cross-sectional area, I_n is moment of inertia of net concrete section.

2.6.2. Anchorage Seating Loss

Due to the uncertainties linked to these losses, in this project it was decided to determine the losses experimentally. There are two options available namely measuring the elongation and loss in strain obtained from strain gauges. The first method is a crude estimate of seating loses due to the visual observation with the help of ruler having least count of 0.5 mm. The second method is more accurate since the actual change in rebar strains were being recorded with the least count of one micron. In this analysis anchorage seating losses are obtained from loss in rebar strains.

2.6.3. Relaxation Loss

In this project two different materials have been used to prestress the slabs, low relaxation steel strands and GFRP rebars.

For low relaxation steel strands the relaxation is obtained from the code equations. As per CAN/CSA S6 the relaxation of low relexation strands before the transfer of prestress is calculated from the following Eq 2-21

$$REL_1 = \frac{log(24 \times t)}{45}\left(\frac{f_{sj}}{f_{py}} - 0.55\right) f_{sj} \qquad \text{Eq 2-21}$$

Where, REL_1 is the loss in prestress due to relaxation before the transfer of prestress, t is the age of concrete in days, f_{sj} is the jacking stress in prestressing steel, f_{py} is yield strength of prestressed steel ($0.9f_{pu}$ for low relaxation strands), f_{pu} is ultimate strength of prestressing tendons.

In the absence of accurate methods as per CAN/CSA S6 the post transfer relaxation is calculated from the following relation in Eq 2-22

$$REL_2 = \left[\frac{f_{st}}{f_{pu}} - 0.55\right]\left[0.34 - \frac{CR + SH}{1.25\, f_{pu}}\right]\frac{f_{pu}}{3} \geq 0.002\, f_{pu} \qquad \text{Eq 2-22}$$

Where, REL_2 is loss in prestress due to relaxation after the transfer of prestress, f_{st} is stress in prestressing steel at transfer, CR is prestress loss due to creep, SH is prestress loss due to shrinkage.

However, in case of GFRP rebars most of the design codes do not permit the use for prestressing and thus the relaxation equations are not available from codes. In such case, a relation (Eq 2-23) presented by Issa (1995) for S-2 glass fibres at a stress level of 45% is used in the calculations.

$$REL_g = \frac{\sigma_{si}}{100}\{0.75 \log(t \times 24) + 1.5\} \qquad \text{Eq 2-23}$$

Where, REL_g is relaxation in GFRP rebar, σ_{si} is the initial prestressing stress in GFRP

2.6.4. Creep Behaviour of Concrete

Creep of concrete depends on many factors, and as such is relatively complex to predict accurately.

The temperature in Canadian weather conditions ranges from -40°C to +35°C. This extensive variation of temperature also effects the creep behaviour of concrete. Fahmi et al. (1972) conducted an experimental investigation to determine the effect of temperature on creep of concrete under 50% and 100% humidity levels. He found that the creep strain increases with the thermal loading as illustrated in Figure 2-1 (Fahmi et al. 1972).

In the current research, a similar behaviour with the sudden increase in temperature was recorded in terms of increase in strain and deflection, when the slabs temperature was abruptly changed from -0.5°C to 22°C by relocating the test slabs from outside environment to inside the lab.

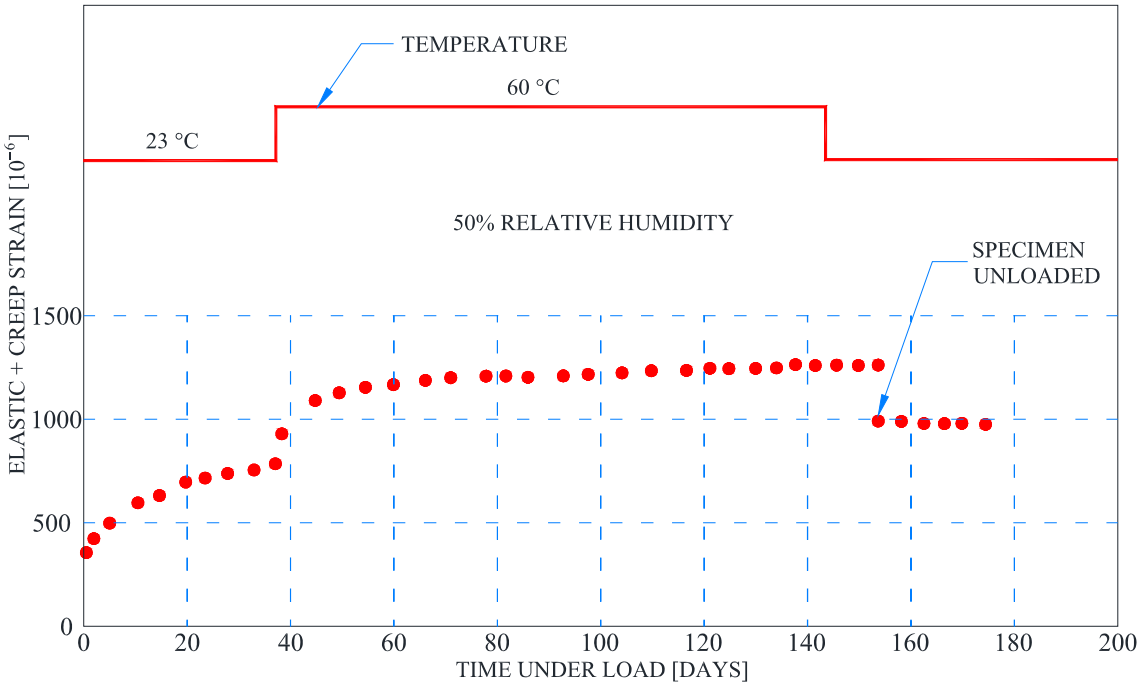

Figure 2-1 Temperature Effects on Creep Behaviour of Concrete; Fahmi et al. (1972)

Creep is often represented through compliance, ACI 209.2R-08 measures compliance through the following Eq 2-24

$$Compliance = \frac{(Elastic\ strain + Basic\ Creep + Drying\ Creep)}{Stress} \qquad \text{Eq 2-24}$$

The total strain observed in a specimen is represented through the following Eq 2-25

$$Total\ Strain = Shrinkage\ strain + Compliance \times Stress \qquad \text{Eq 2-25}$$

In this thesis three creep models have been adopted for determining their suitability to the slabs in this experiment, exposed to the outside environmental conditions.

2.6.4.1. ACI 209R-92 Creep Model (1992)

This is one of the simplest methods to determine creep and shrinkage in concrete. The creep coefficient at any time 't' is obtained from the ultimate values by multiplying the factors offset from the standard conditions.

The model was originally developed for precast prestressed industry. Ironically it imposes the limitation of minimum age of 7 days at the time of loading. It implies that for precast members subjected to early age loading it may not provide satisfactory estimation of creep.

ACI 209R-92 (1992) calculates creep in terms of creep coefficient given by the following Eq 2-26

$$\phi(t, t_0) = \frac{(t - t_0)^{\psi}}{d + (t - t_0)^{\psi}} \phi_u \qquad \text{Eq 2-26}$$

Where, $\phi(t,t_0)$ is creep coefficient at time t, t_0 is the age of concrete in days at the time of loading, d and ψ are the constants which take into account the member shape and size, ϕ_u (Eq 2-27) is the ultimate creep coefficient for the standard conditions. For conditions other than standard it can be obtained by multiplying the factors given in Eq 2-28.

$$\varphi_u = 2.35\,\gamma_c \qquad \text{Eq 2-27}$$

$$\gamma c = \gamma_{c,to}\,\gamma_{c,RH}\,\gamma_{c,vs}\,\gamma_{c,s}\,\gamma_{c,\psi}\,\gamma_{sh,\alpha} \qquad \text{Eq 2-28}$$

Where

γ_c = Cumulative correction factor

$\gamma_{c,to}$ = Age of loading factor for creep

$\gamma_{c,RH}$ = Ambient relative humidity factor

$\gamma_{c,vs}$ = Coefficient for volume-surface variation

$\gamma_{c,s}$ = Correction factors for slump variation

$\gamma_{c,\psi}$ = Fine aggregate factor

$\gamma_{sh,\alpha}$ = Air content factor

Compliance at time *t* can be obtained from the calculated creep coefficient from the following Eq 2-29

$$J(t,t_0) = \frac{1+\phi(t,t_0)}{E_{ct0}} \qquad \text{Eq 2-29}$$

Where, $J(t,t_0)$ is compliance at time *t*, E_{ct0} is modulus of elasticity of concrete at the time of loading.

2.6.4.2. CEB MC90-99 Creep Model (1999)

This method is advantageous when the temperature deviation is large from the standard conditions. The method considers the effect of temperature by changing the maturity of concrete during curing and after curing. The method can handle the temperature range of 5°C to 30°C. The effect of temperature can be finely incorporated by reducing the time steps at the expense of computational effort. The model assumes linear variation of creep with stress up to 40% of its strength and the stress in concrete for the determination of creep is limited to 40% of ultimate strength.

Compliance at any time *t* is calculated from Eq 2-30

$$J(t,t_0) = \left[\frac{1}{E_{ct0}} + \frac{\phi(t,t_0)}{E_c}\right] \qquad \text{Eq 2-30}$$

The creep coefficient can be calculated from the following Eq 2-31

$$\phi(t, t_0) = \phi_0 \, \beta_c \, (t - t_0) \qquad \text{Eq 2-31}$$

Where

ϕ_0 = Notional creep coefficient

β_c = coefficient that describes the development of creep with time

2.6.4.3. Bažant-Baweja B3 Creep Model (1995)

This method is claimed to be good for both simple and complicated structures. It also considers the age at loading of one day, that is important to the test slabs considered in this project. Since the prediction of creep by this method is governed by compliance function, thus it eliminated the error due to the estimation of elastic modulus of concrete.

The compliance at the age of '*t*' days can be calculated from the following Eq 2-32

$$J(t, t_0) = q_1 + C_0(t, t_0) + C_d(t, t_0, t_c) \qquad \text{Eq 2-32}$$

Where

q_1 = Instantaneous strain due to unit stress at a time of about 10^{-9} second

$C_0(t,t_0)$ = Compliance function for basic creep

$C_d(t,t_0,t_c)$ = Additional compliance function for drying creep

2.6.5. Shrinkage

Shrinkage in concrete is primarily due to drying and chemical change in concrete. It is a time dependent phenomenon and is accounted in terms of drying shrinkage and autogenous shrinkage forms.

Drying shrinkage is primarily due to loss of water from concrete and it continues for years. Drying shrinkage occurs due to evaporation, thus factors like surface area of the cross-section and the nature of pours in concrete are the major influencing factors. These

factors are influenced by the surrounding humidity level, volume to surface ratio, water cement ratio, aggregate content etc.

Chemical shrinkage occurs mainly due to the hydration process and is termed as autogenous shrinkage.

Other than the above two types, concrete also undergoes shrinkage due to dissipation of heat of hydration and plastic shrinkage. Plastic shrinkage occurs during setting and is responsible for cracks during setting.

Accurate prediction of shrinkage becomes critical when dealing with members having large surface area to volume ratio with low reinforcement. In such cases with flexural members, the cracking moment can reduce substantially. This reduction in cracking moment due to shrinkage of concrete can estimated by the previously discussed methods by Gilbert (1999), Scanlon & Bischoff (2008).

In this thesis three shrinkage models have been adopted to predict the long term behaviour of test slabs namely, ACI 209R-92, CEB MC90-99 and Bažant-Baweja B3 shrinkage model. They will be discussed in the following sections.

2.6.5.1. ACI 209R-92 Shrinkage Model (1992)

ACI 209 defines the shrinkage strains at any time in terms of ultimate shrinkage values. ACI209.2R-08 (2008) concludes that "*ACI 209R-92 model overestimates measured shrinkage at low shrinkage values (equivalent to short drying times) and underestimates at high shrinkage values (typical of long drying times)*". The ultimate shrinkage strain under non-standard conditions can be obtained from the following Eq 2-33

$$\varepsilon_{shu} = 780 \times 10^{6}(\gamma_{sh,tc}\,\gamma_{sh,RH}\,\gamma_{sh,vs}\,\gamma_{sh,s}\,\gamma_{sh,\psi}\,\gamma_{sh,c}\,\gamma_{sh,\alpha}) \qquad \text{Eq 2-33}$$

Where

ε_{shu} = Ultimate shrinkage strain

$\gamma_{sh,tc}$ = Initial moist curing coefficient

$\gamma_{sh,RH}$ = Ambient relative humidity coefficient

$\gamma_{sh,vs}$ = Coefficient for the variation of size

$\gamma_{sh,s}$ = Slump correction factor

$\gamma_{sh,\psi}$ = Fine aggregate factor

$\gamma_{sh,c}$ = Cement content factor

$\gamma_{sh,\alpha}$ = Air content factor

Shrinkage at the age of *t* days is calculated from Eq 2-34

$$\varepsilon_{sh}(t, t_c) = \frac{(t - t_c)^{\alpha}}{f + (t - t_c)^{\alpha}} \varepsilon_{shu} \qquad \text{Eq 2-34}$$

Where, ε_{sh} (t,t_c) is shrinkage strain at the age of '*t*' days, t_c is age of concrete at the end of moist curing, *f* and α are the constants for a given member shape and size.

2.6.5.2. CEB MC90-99 Shrinkage Model (1999)

This model calculates the shrinkage (Eq 2-35) or swelling in terms of drying shrinkage (Eq 2-37) and autogenous shrinkage(Eq 2-36).

$$\varepsilon_{sh}(t, t_c) = \varepsilon_{cas}(t) + \varepsilon_{cds}(t, t_c) \qquad \text{Eq 2-35}$$

Where, ε_{cas} (t) is autogenous shrinkage and ε_{cds} (t,t_c) is drying shrinkage.

The autogenous shrinkage is obtained from the following Eq 2-36

$$\varepsilon_{cas}(t) = \varepsilon_{cas0}(f_{cm28}) \times \beta_{as}(t) \qquad \text{Eq 2-36}$$

$\varepsilon_{cas0}(f_{cm28})$ is notional autogenous shrinkage coefficient that depends on the compressive strength of concrete and the type of cement, $\beta_{as}(t)$ calculates the time development of autogenous shrinkage. The drying shrinkage is represented below.

$$\varepsilon_{cds}(t, t_c) = \varepsilon_{cds0}(f_{cm28})\, \beta_{RH}(h) \beta_{ds}(t, t_c) \quad \text{Eq 2-37}$$

$\varepsilon_{cdso}(f_{cm28})$ is notional drying shrinkage coefficient that depends on the type of cement and concrete strength, $\beta_{RH}(h)$ defines the effect of relative humidity and $\beta_{ds}(t,t_c)$ takes into account the age of concrete.

2.6.5.3. Bažant-Baweja B3 Shrinkage Model (1995)

This model calculates the mean shrinkage at any time through ultimate shrinkage by Eq 2-38 written below

$$\varepsilon_{sh}(t, t_c) = -\varepsilon_{sh\infty}\, k_h\, S(t - t_c) \quad \text{Eq 2-38}$$

Where

$\varepsilon_{sh\infty}$ = Ultimate shrinkage

k_h = Humidity dependent factor

$S(t\text{-}t_c)$ = Time function for shrinkage

2.7. Age Adjusted Effective Modulus Method

For long term behaviour of concrete members Trost (1967) refined the effective modulus method by introducing the term χ for relaxation problems and termed it as relaxation coefficient. Later on Bazant (1972) found it suitable for creep and relaxation problems and developed the formulation and introduced it as aging coefficient to modify the effective modulus and termed it "age-adjusted effective modulus."

This method (for long term effects) is suitable for problems where the aging of concrete becomes significant and thus concrete is subjected to variable stress history, which is essentially for the cases of early loading of members. The primary target of aging coefficient is to modify the effective modulus of concrete to consider the effects on creep strain due to the variability involved in the stress history of a structure under constant

load with the increase in time. The age adjusted effective modulus can be represented by the following Eq 2-39.

$$E"_e(t,t_0) = \frac{E_c(t_0)}{1+\chi(t,t_0)\,\phi(t,t_0)} \qquad \text{Eq 2-39}$$

Where χ is aging coefficient that can be obtained through Volterra's integral through relaxation function (Bazant 1972). For precast, prestressed concrete members Tadros (1985) suggested that the range of aging coefficient lies between 0.6 and 0.9, for simplicity a constant value of 0.7 was recommended.

The age-adjusted effective modulus method for cracked and uncracked sections with and without prestressing has been implemented as illustrated by Gilbert (2010).

The formulation of this method can be understood by considering an element with uniaxial loading subjected to constant stress. The total strain at time '*t*' in the element is represented by Eq 2-41.

$$\varepsilon(t,t_0) = \varepsilon_e(t_0) + \varepsilon_{cr}(t,t_0) + \varepsilon_{sh}(t,t_0) \qquad \text{Eq 2-40}$$

$$\varepsilon(t,t_0) = \frac{\sigma_c(t_0)}{E_c(t_0)}[1+\phi(t,t_0)] + \frac{\Delta\sigma_c(t)}{E_c(t_0)}\,[1+\chi(t,t_0)\,\phi(t,t_0)] + \varepsilon_{sh}(t,t_0)$$

$$\varepsilon(t,t_0) = \frac{\sigma_c(t_0)}{E_e(t,t_0)} + \frac{\Delta\sigma_c(t)}{E"_e(t,t_0)} + \varepsilon_{sh}(t,t_0) \qquad \text{Eq 2-41}$$

Where, $\varepsilon(t,t_0)$ is the total strain at any time *t*, $\varepsilon_e(t_0)$ is the initial elastic strain, $\varepsilon_{cr}(t,t_0)$ and $\varepsilon_{sh}(t,t_0)$ are the strain due to creep and shrinkage respectively, $\sigma_c(t_0)$ and $E_c(t_0)$ are the concrete stress and modulus of elasticity at the time of loading, $\Delta\sigma_c(t)$ is the change in concrete stress with time, $E_e(t,t_0)$ is the effective modulus of concrete.

In the current study, due to the time lag in the application of superimposed dead weight with respect to the application of self weight of slabs, the method of superposition is implemented in the determination of deflection due to creep and shrinkage of concrete.

3. Experimental work

3.1. General

The research aims to investigate the short term and long term behaviour of concrete slabs prestressed with GFRP, steel tendons, or reinforced with GFRP. The long term observation includes the variation in deflection, strain in longitudinal bars and properties of concrete with time. In short term study strain in longitudinal bars, deflection, number of cracks, crack pattern with load and ultimate moment capacity of the slabs are considered.

Four types of slabs were cast; each type contains three test slabs listed in Table 3-1.

Table 3-1 Types of Test Slabs

Slab Type	Number of samples
Slabs prestressed to 65% of ultimate strength with steel tendons	3
GFRP reinforced slabs	3
GFRP slabs prestressed to 24% of ultimate strength of GFRP	3
GFRP slabs prestressed to 35% of ultimate strength of GFRP	3

The slabs prestressed with steel tendons were cast under the same industrial conditions as for the Brookside Cemetery, Winnipeg, Manitoba. In addition to the above first set, non prestressed GFRP slabs were also cast at Lafarge precast plant. Remaining two types were constructed at University's of Manitoba W.R. McQuade Heavy Structures Laboratory in the same prestressing beds.

3.2. Design and Details of Test Specimens

The design details of steel prestressed slabs were kept the same as the Brookside Cemetery slabs manufactured by Lafarge. The details of the GFRP reinforced slabs were kept the same as the steel prestressed and GFRP prestressed samples as shown in Figure 3-1. The reinforcement details and its arrangement can be referred in Table 3-2 and Figures 3-2 to 3-6.

Table 3-2 Slab Details

Slab Name	Clear Cover [mm]	Reinforcement Type & number	Prestressing Percentage	Test Performed	f´c [MPa]
S-65-1	50	4 - Steel Strands	65% to 70%	Long Term	69.7
S-65-2	50	4 - Steel Strands	65% to 70%	Long Term	66.5
S-65-3	50	4 - Steel Strands	65% to 70%	Short Term	74.2
F-0-1	60	6 - GFRP bars	0%	Long Term	75.2
F-0-2	50	6 - GFRP bars	0%	Long Term	69.2
F-0-3	50	6 - GFRP bars	0%	Short Term	75.5
F-24-1	45	6 - GFRP bars	24%	Long Term	72.1
F-24-2	45	6 - GFRP bars	24%	Long Term	46
F-24-3	45	6 - GFRP bars	24%	Short Term	67.1
F-35-1	40	6 - GFRP bars	35%	Long Term	72.1
F-35-2	40	6 - GFRP bars	35%	Long Term	46
F-35-3	40	6 - GFRP bars	35%	Short Term	67.1

The top surface of the slab is trapezoidal in shape, thus to achieve a good finished surface the slabs were cast upside down. In Table 3-2 the first letter of slab name "S" or "F" represents the type of prestressing/reinforcing material where "S" stands for low

relaxation steel strand and "F" stands for GFRP bar. The number after the first letter indicates the effective prestressing level with respect to the ultimate strength of strand/bar. The last number distinguishes between the identical samples.

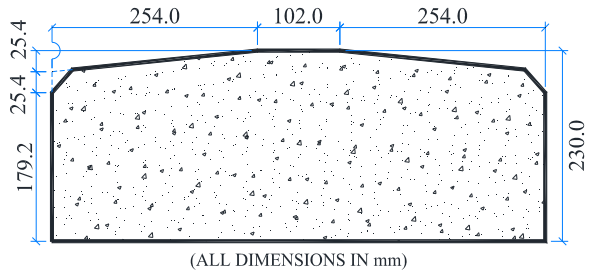

Figure 3-1 Details of Slab Cross-Section

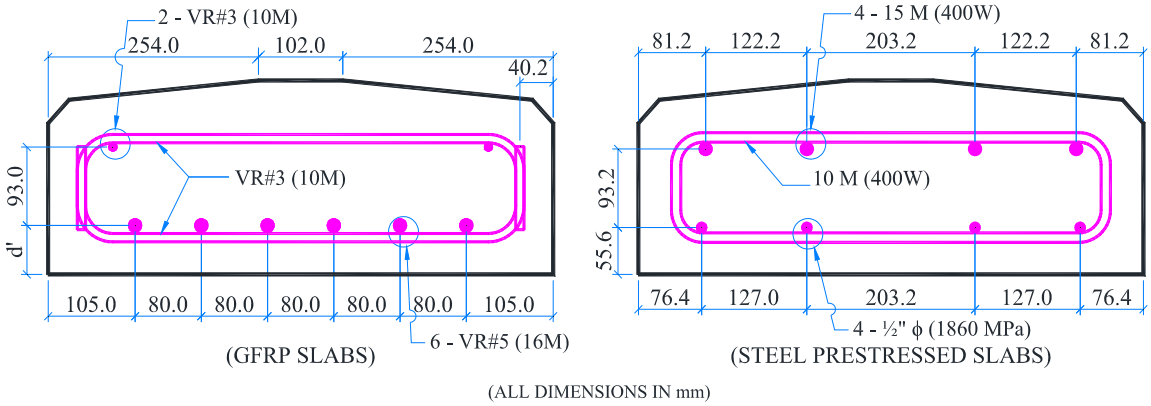

Figure 3-2 Reinforcement Details of Slab

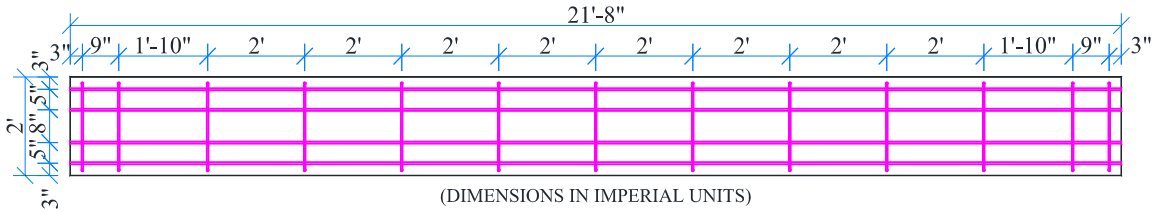

Figure 3-3 Stirrup Arrangement in Steel Prestressed Slab

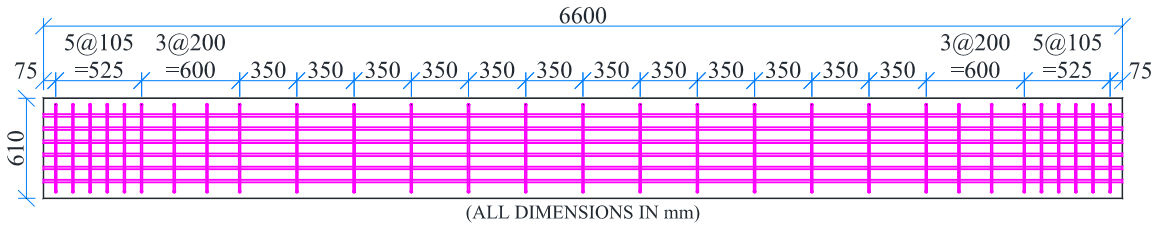

Figure 3-4 Stirrup location in GFRP Reinforced/Prestressed Slabs (TYP)

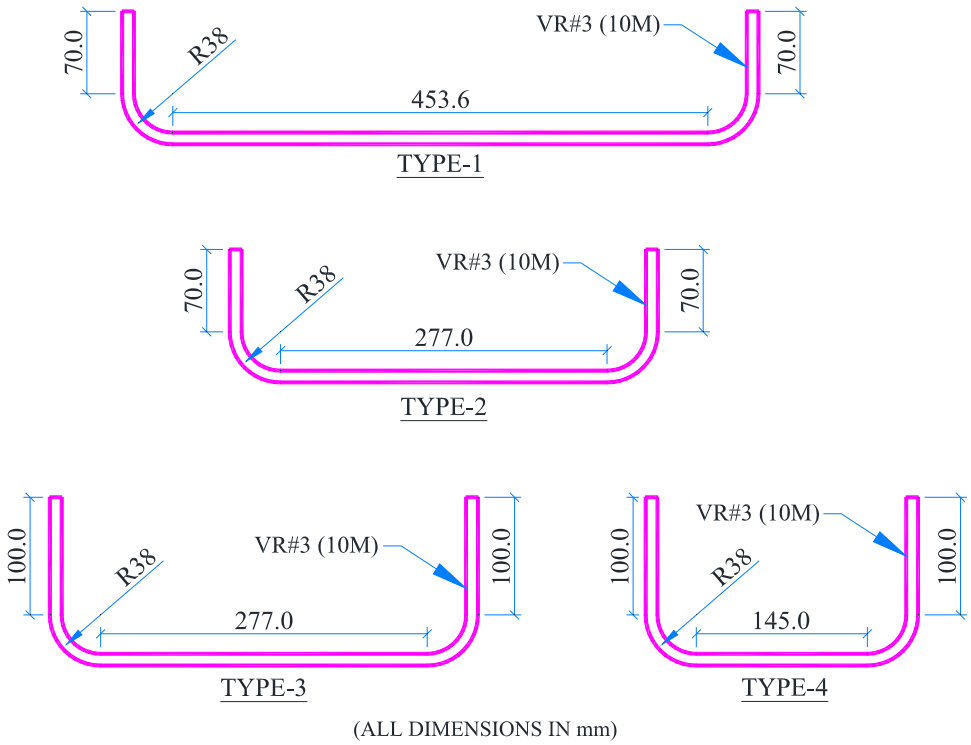

Figure 3-5 Details Of Stirrups in the Slabs

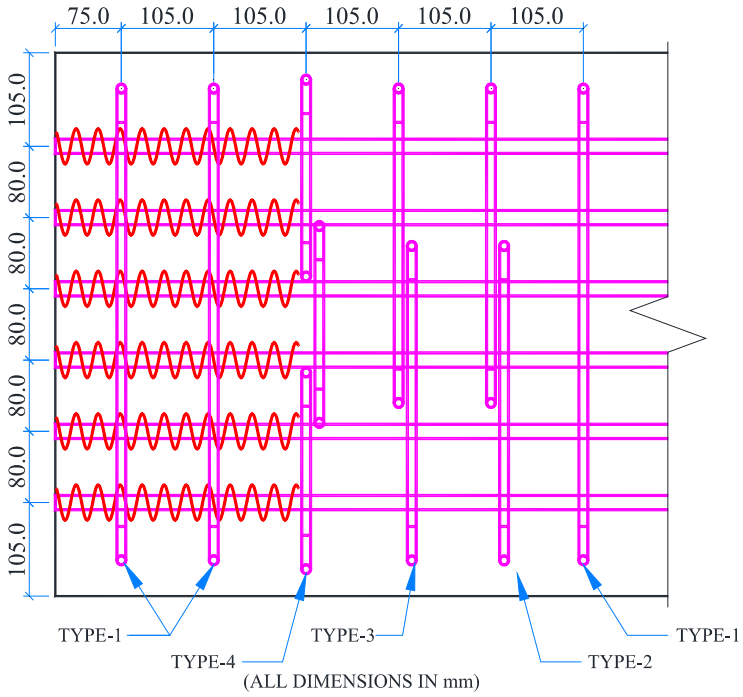

Figure 3-6 Reinforcement Arrangement at End of Slab

The chronological order of construction and testing is listed in Table 3-3. A total of four slabs tested to failure, and the remaining slabs were used for long-term monitoring. The

slabs reserved for long term monitoring were loaded with five point loads listed in Table 3-4 on June 27, 2013.

Table 3-3 Casting and Testing Sequence of Slabs

Slab Name	Cast Date	Formwork Removal Date	Pre-cracking Date	Testing date
S-65-1	25-Sept-2012	26-Sept-2012	13-June-2013	-
S-65-2	09-Oct-2012	10-Oct-2012	12-June-2013	-
S-65-3	12-Oct-2012	15-Oct-2012	-	23-May-2013
F-0-1	25-Sept-2012	26-Sept-2012	18-June-2013	-
F-0-2	09-Oct-2012	10-Oct-2012	17-June-2013	-
F-0-3	12-Oct-2012	15-Oct-2012	-	16-May-2013
F-24-1	26-April-2013	29-April-2013	11-June-2013	-
F-24-2	12-March-2013	15-March-2013	10-June-2013	-
F-24-3	19-Feb-2013	22-Feb-2013	-	19-April-2013
F-35-1	26-April-2013	29-April-2013	11-June-2013	-
F-35-2	12-March-2013	15-March-2013	10-June-2013	-
F-35-3	19-Feb-2013	22-Feb-2013	-	03-April-2013

To capture the camber/initial deflection, deflection due to creep, cracking, loading and to interlink all these progressive deflections, stainless steel rulers were embedded on the side face of the slabs at the time of casting.

3.3. Test Setup

Out of the total of 12 slabs, four were tested till failure and the remaining eight were monitored for long term behaviour. For long term observation the slabs were loaded with the dead weight as listed in Table 3-4 with the help of concrete blocks shown in Figure 3-7 and Figure 3-10. The concrete blocks represent the granite markers at the cemetery. It

was attempted to keep the weight of all the blocks equal to 68 kg however the achieved loads varied between 73.6 to 77 kg and are listed in Table 3-4. The load contribution of concrete blocks varied from 20.2% to 22.9 % with respect to the self-weight of the slabs.

Table 3-4 Long Term Five Point Loading Details

Slab ID	P1 [kg]	P2 [kg]	P3 [kg]	P4 [kg]	P5 [kg]
S-65-1	74.4	74.5	74.9	75.2	73.8
S-65-2	76.6	76	76.2	76.6	76.3
F-0-1	74	76.5	74.1	76.4	74.8
F-0-2	76.1	76	75.4	77	76.7
F-24-1	74.8	74	76.5	74.9	75.1
F-24-2	76.1	76.4	75.7	76.6	76.6
F-35-1	73.4	75.7	73.6	76.2	76.8
F-35-2	74.2	73.9	76	75.8	74.5

Figure 3-7 Long Term Loading

Before loading the slabs, they were pre-cracked for a better comparison of creep behaviour of prestressed slabs with non-prestressed slabs. Theoretically precracking should not influence the long term behaviour of a prestressed member (other than residual deflection) if the external load does not overcome the compressive stresses generated due to prestressing.

In this research we want to also observe the influence of cracks on the durability/long term behaviour of GFRP prestressed slabs in comparison with the steel prestressed slabs. Thus, at the end of 10 years a material degradation study will be performed on prestressed/non-prestressed GFRP bars and steel strands to compare their deterioration under natural environmental conditions.

The pre-cracking and failure load were applied through four point bending mechanism with the help of 5000 kN MTS machine. Since this is a displacement-controlled machine, thus the loading was applied in terms of mm/minutes. All the four points were either hinge or roller supports for free rotation at support and loading points as illustrated in Figure 3-8. The load from MTS was transferred to the slab on two points across the section through 3 spreader beams.

The loading rate for precracking the slabs was kept constant. The loading rate for ultimate testing was progressively increased due to large deflection before failure of slabs as discussed in Appendix-B. A schematic arrangement of long term test setup is shown in Figure 3-9 and Figure 3-10.

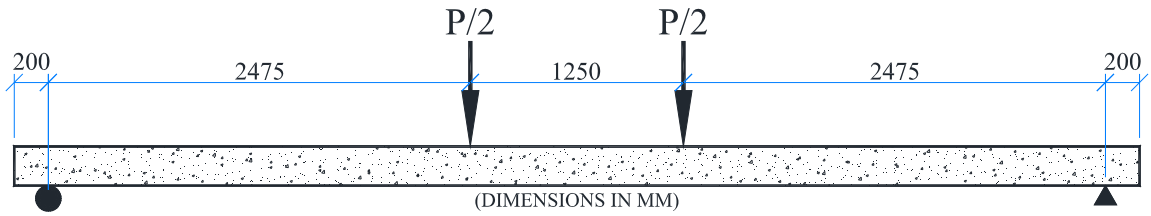

Figure 3-8 Loading Scheme for Testing and Precracking

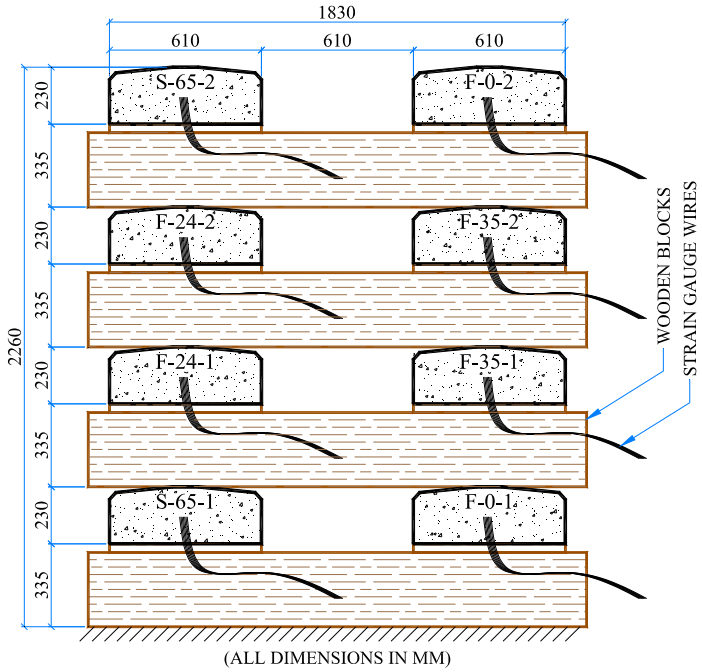

Figure 3-9 Long Term Test Setup (End View)

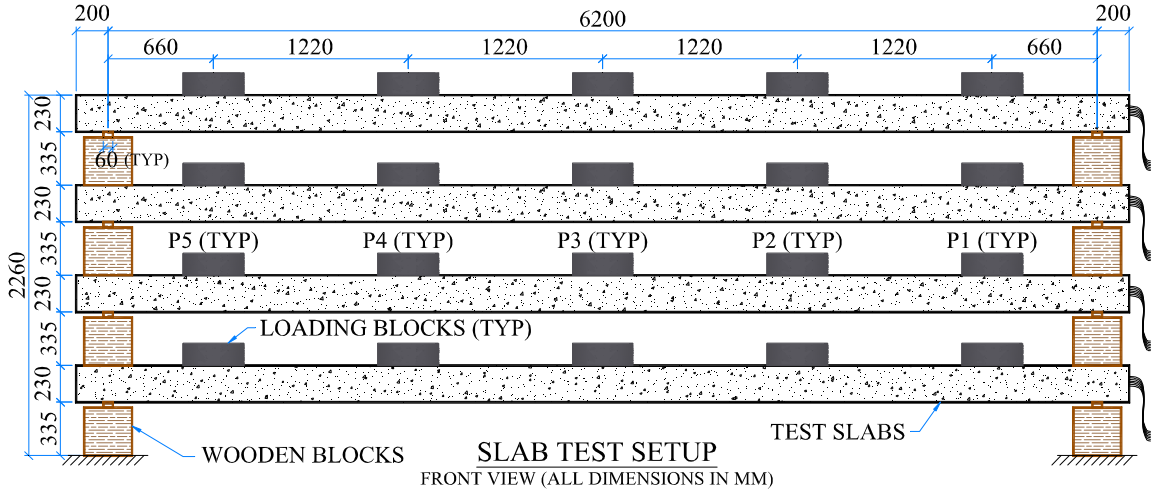

Figure 3-10 Long Term Test Setup (Elevation)

3.4. Reinforcement Details

The GFRP rebars and stirrups used in reinforcing and prestressing were manufactured with a trade name Pultrall V-Rod. The GFRP rebars were tested for the modulus of elasticity and ultimate strength. The remaining information is taken from the manufacturer's data sheet. Table 3-5 summarises the properties of GFRP.

Table 3-5 Properties of GFRP Bars from Manufacturer

Reinforcement	Diameter [mm]	Longitudinal coefficient of thermal expansion [per °C]	Nominal cross-sectional area [mm^2]	Nominal Tensile strength [MPa]		Nominal Tensile modulus [MPa]	
				Manufacturer	Experimental	Manufacturer	Experimental
Longitudinal	15.875	6.4×10^{-6}	197.933	751	863.4	48200	54954
Longitudinal	9.525	5.5×10^{-6}	71.256	856	-	45400	-
Stirrups	9.53	5.5×10^{-6}	71.256	856	-	45400	-

For the steel prestressed slabs low relaxation steel strands and galvanized bars were provided by Lafarge Winnipeg. The details are listed in Table 3-6

Table 3-6 Steel Reinforcement Details

Type of Reinforcement	Diameter/Size	Grade
Steel Strand	12.7 mm ϕ	1860 MPa
Rebar	15 M	400 W
Stirrup	10 M	400 W

3.5. Concrete

Concrete for slabs was acquired from two Lafarge facilities. The first six slabs (three GFRP non-prestressed and three steel prestressed slabs) were cast at Lafarge precast plant

and the concrete was obtained from their mixer. The concrete for remaining six GFRP prestressed slabs was ordered from Lafarge ready mix plant.

The mix design adopted by both facilities was same except retarder was added by the ready mix plant. Due to the use of retarder, the prestressed GFRP slabs did not achieve the required strength after one day and the prestress transfer process was executed on day three. Even though the mix design for all the concrete batches as reported by Lafarge was the same, in one of the concrete batches for slabs F-24-2 and F-35-2, the air content measured at University of Manitoba laboratory was found approximately double (15%) from all other concrete batches. Tests done on the concrete at University of Manitoba laboratories suggest that the properties obtained from both facilities were substantially different.

The targeted concrete design strength was 60 MPa. However, the concrete strengths obtained from tests ranged between 46 MPa and 75 MPa and are listed in Table 3-2. Since the mix design is proprietary of Lafarge it is not possible to publish it in this report, however for the analysis purpose Lafarge has provided the mix design details that were used where needed.

The wet concrete was tested for temperature, slump and air content. For compressive strength, split cylinder test and modulus of elasticity, 4 inch in diameter and 8 inches long concrete cylinders were cast. In addition, to get the complete stress-strain relationship strain gauges was installed on some cylinders as shown in Figure 3-11.

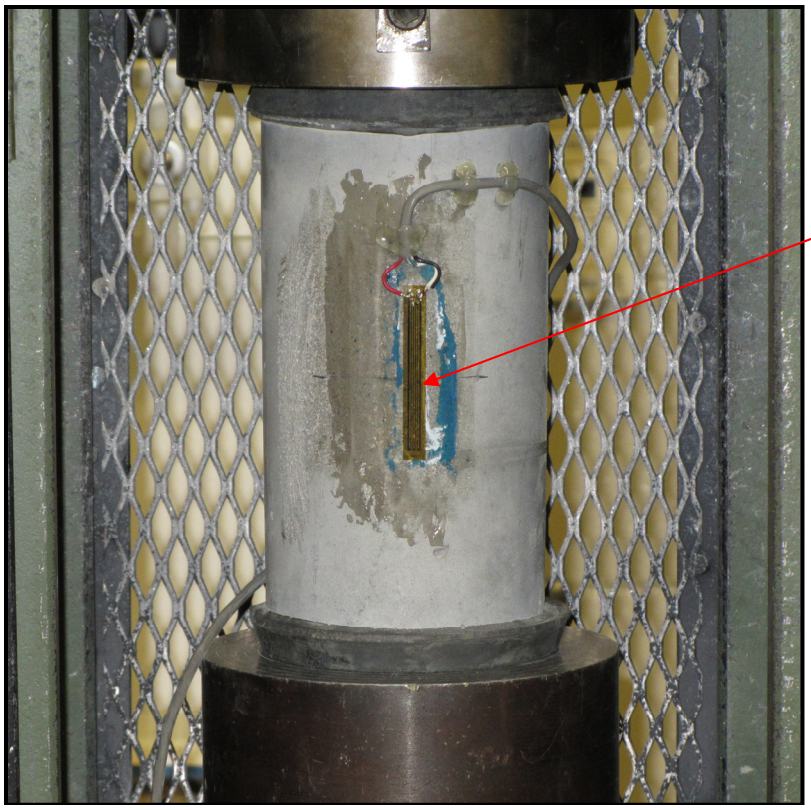

Figure 3-11 Compression Test with ESG

Figure 3-12 Split Cylinder Test Setup

The compression test and modulus of elasticity tests were done in accordance with ASTM Code C39/C39M (2012) and C469 (2010) respectively. The stress rate varied from 375 to 425 pounds/sec. The setup for split cylinder test was done as instructed in ASTM C496/C496M (2011). Compressometer with the attached dial gauge was used to record the modulus of elasticity according to the procedure confirming to ASTM code C469 (2010). The distance measured at rotating yoke from pivot rod to the vertical plane passing through support points on concrete cylinder and from the same vertical plane to the dial gauge was not same, thus the dial gauge reading has been suitably modified as explained in ASTM C469 (2010). The modulus of elasticity was determined from the stress obtained at 50×10^{-6} strain and the strain obtained at 40% of ultimate stress.

Concrete cylinders were tested at the age of 1, 3, 7, 14, 28 days and at the time of cracking/testing of slabs with some exceptions for testing on day one. For the cylinders cast at Lafarge, the cylinder tests on day one was performed on their equipment, all other testing was performed at the University of Manitoba using 300,000 pound hydraulically operated machine. The cylinders subjected to compression were capped with sulphur to avoid fracturing of corners before their ultimate capacity was reached.

3.6. Prestressing Setup

The GFRP and steel prestressed slabs were cast and stressed in the self-stressing foamwork received from Lafarge. In the case of steel strands the prestressing force was transferred to the strands through conventional method by means of chucks holding on to the steel plates. However this method cannot be applied to the GFRP bars and for the smooth transfer of stress, the ends of GFRP rebars were grouted in the steel anchorage

tubes using expansive grout (Blister). The diameter and length of the anchorage was in accordance with CSA-S806.

Since the length of the GFRP rebars to be anchored was 8385 mm, it was possible to bring them to semicircular shape without any damage and afterwards they were held in position with the help of jig as shown in Figure 3-13, the jigs at both the ends were supported by two steel columns spaced as shown in Figure 3-14.

Figure 3-13 Anchor Installation on GFRP

Figure 3-14 Setup for Anchor Installation

The transfer of the prestressing force to GFRP rebars was done with the help of couplers, as shown in Figure 3-15 and Figure 3-16. The prestressing arrangement for GFRP rebars is schematically explained in Figure 3-17.

To avoid the possibility of non-uniform stressing in the rebars/strands, the prestressing and transfer sequence has been done in the symmetrical fashion from the center of slab towards the outer edges, as illustrated in Figure 3-18.

To measure the load applied through the hydraulics, a load cell was placed between the loading jack and chuck as shown in Figure 3-19. The strains in the bars were considered as the governing criteria for the application of load since the losses during the stress transfer from jack varied depending on the slip in the chuck. The elongation in the bars was also recorded for cross verification of prestressing level.

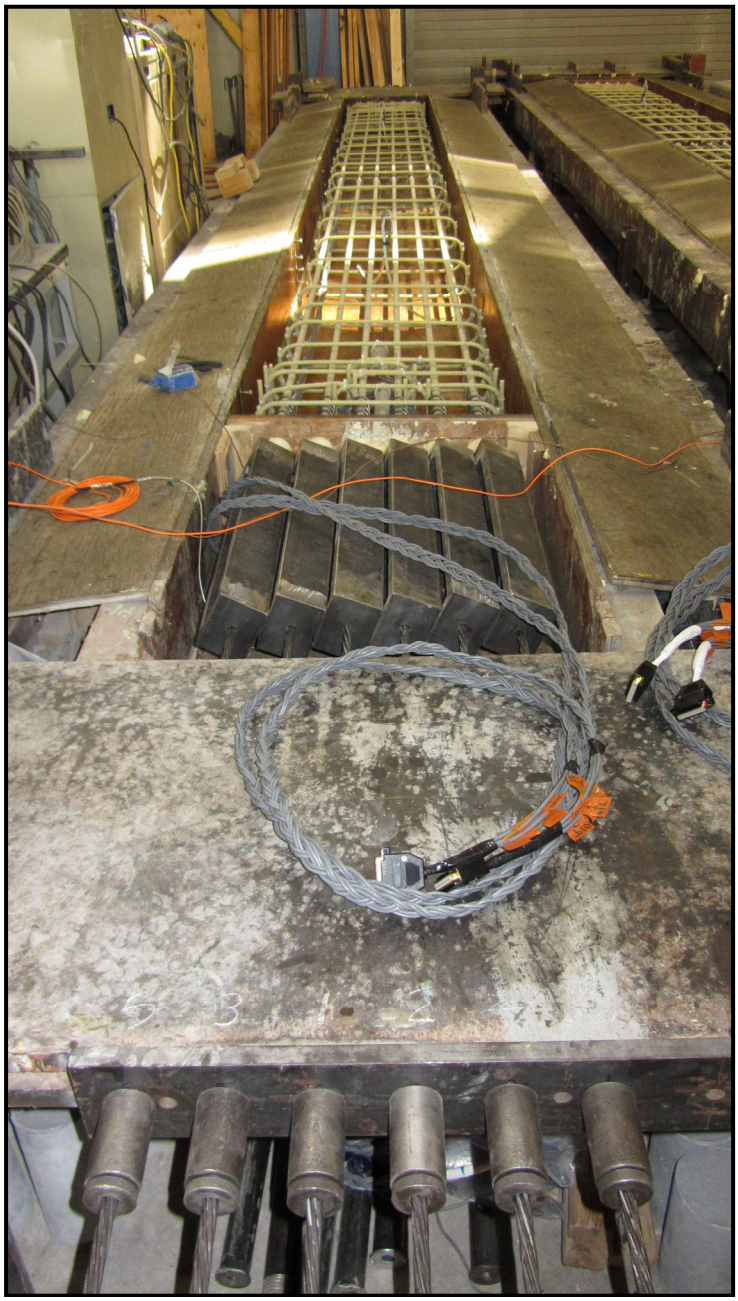

Figure 3-15 Prestressing Bed

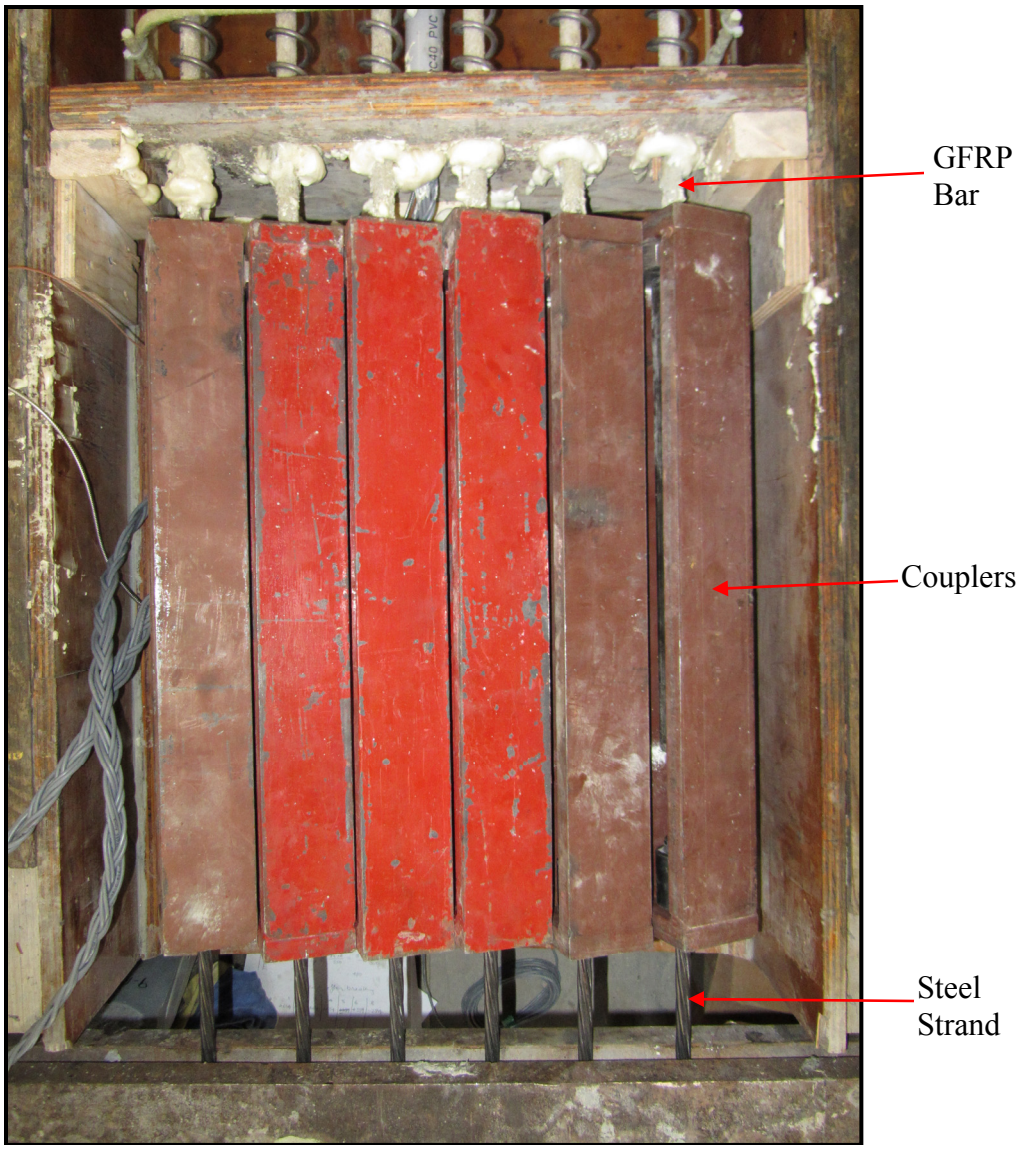

Figure 3-16 Couplers for Transferring Prestress from Steel Strand to GFRP Bars

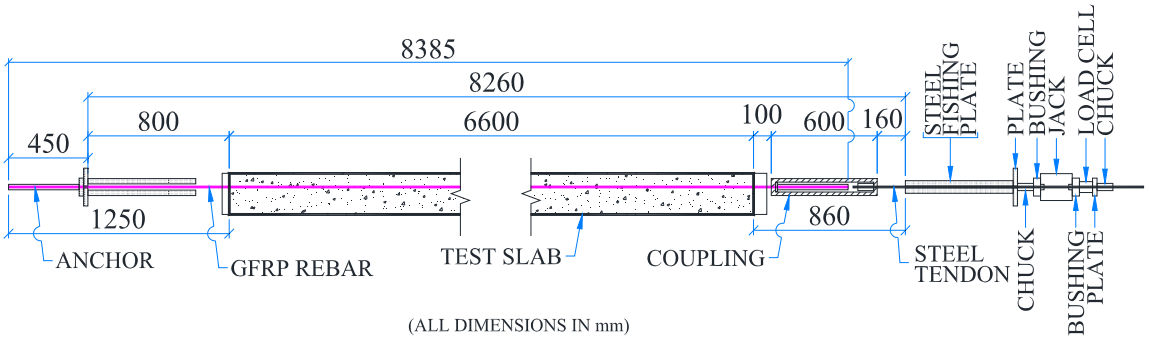

Figure 3-17 Prestressing Arrangement (Elevation)

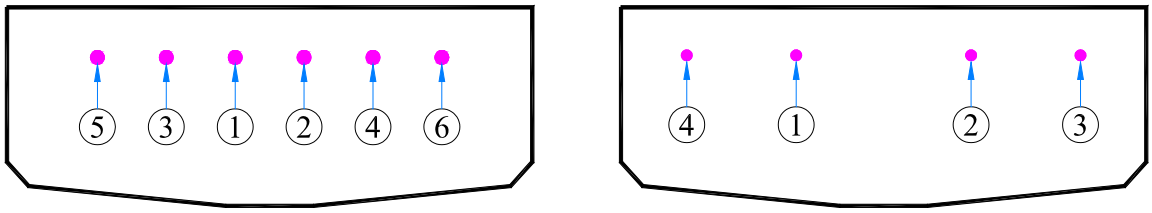

STRESSING & TRANSFER SEQUENCE (GFRP SLABS)

STRESSING & TRANSFER SEQUENCE (STEEL SLABS)

Figure 3-18 Stressing and Transfer Sequence (GFRP and Steel)

Figure 3-19 Hydraulic Jack and Load Cell Setup

3.7. Instrumentation

3.7.1. Electrical Strain Gauges (ESG)

Electrical strain gauges were used to capture the strains in the longitudinal GFRP bars and steel strands. These gauges were installed at mid-span of the slabs.

Considering the duration and exposure to the outside environment, 6.35 mm gauge length 350 Ω gauges with two different self-temperature compensations were used on GFRP bars. However due to installation difficulties on steel strands the 350 Ω gauges were replaced by 2 mm, 120 Ω gauges. 50.8 mm, 120 Ω strain gauges were used to record the strains in concrete cylinders during compression tests for modulus of elasticity and to acquire the stress-strain relationship of concrete. Two 50.8 mm, 120 Ω strain gauges were installed on each slabs tested till failure to get the strain profile of the cross-section at mid span of slabs as shown in Figure 3-20. The properties of the strain gauges are represented in Table 3-7

Table 3-7 Electrical Strain Gauge Design Specifications†

Grid Resistance	350 Ω	350 Ω	120 Ω	120 Ω
Manufacturer	Micro-Measurements			TML
STC Number	06	03	06	-
Gauge Factor	2.115	2.11	2.105	2.11
Gauge Length [mm]	6.35	6.35	50.8	2
Thermal Output equation for Gauges [10^{-6}/ºC]	a0 + a1×T + a1×T2 + a1×T3 + a1×T4			
Thermal output Coefficients@ G.F. of 2.0 [for temperature in ºC]	a0 = -88 a1 = 5.86 a2 = -9.96×10^{-2} a3 = 4.73×10^{-4} a4 = -5.89×10^{-7}	a0 = -1.6×10^{2} a1 = 8.86 a2 = -1.02×10^{-1} a3 = 2.76×10^{-4} a4 = 0.0	a0 = -98.7 a1 = 6.43 a2 = -1.06×10^{-1} a3 = 4.81×10^{-4} a4 = -5.72×10^{-7}	a0 = -29.7 a1 = 2.73 a2 = -7.23×10^{-2} a3 = 5.3×10^{-4} a4 = -1.4×10^{-6}
Material used for thermal output coefficient from manufacturer	1018 Steel	Molybdenum	1018 Steel	SS 400
CTE of Material used for thermal output coefficient [10^{-6}/ºC]	12.1	4.9	12.1	11.8

†Table compiled from manufacturer's data sheets

One of the tasks of this project is to study the long term suitability of strain gauges for strain measurement in outside environment. This includes the variation of strains with change in temperature and the compatibility of the gauges with the specific type of materials.

During the long term observation, the slabs were exposed to outside environment and the variation of strains due to temperature became major influencing factor due to their sensitivity towards change in temperature. Thus it became essential to correct the strains for their thermal output in order to get the correct strains in the reinforcement.

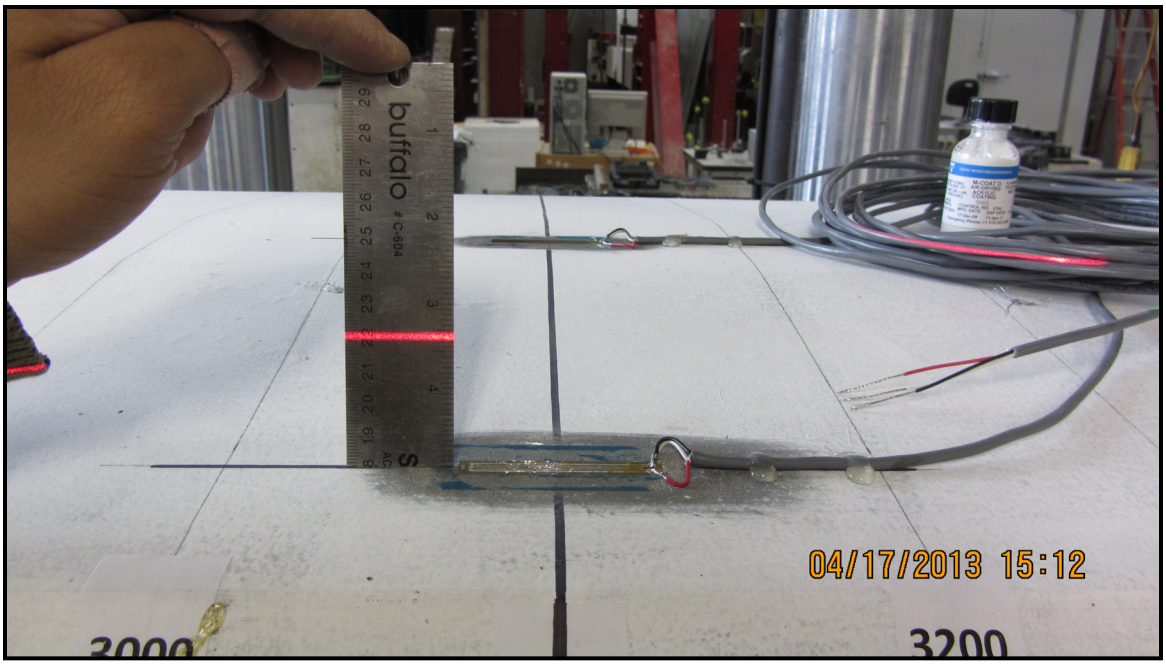

Figure 3-20 ESG on the Top Face of Slab

Different methods can be adopted to compensate for the thermal output of the strain gauges. First a dummy gauge can be used. Dummy gauge is a strain gauge mounted on a bar that is not subjected to any stresses due to load. Another way to compensate for thermal output is to use the manufacturer's recommended equations. Strain gauges are manufactured for use with material of specific coefficient of thermal expansion (CTE). If the strain gauges are used on material with different CTE as the one used to determine the thermal output by the manufacturer, the thermal output has to be adjusted for the test material. This mismatch in CTE between the test material and the material used for obtaining thermal output of a self temperature compensating strain gauge is termed as self-temperature compensation (STC) mismatch. The mismatch restricts from direct application of correction provided by manufacturer to the recorded strains.

However, this STC mismatch can be corrected by subtracting excess correction obtained from the difference between the CTE used by the manufacturer with the CTE of test material in the thermal output equation provided by manufacturer. Figure 3-21 shows the

the CTE of GFRP (test material) and steel (used by manufacturer to obtain thermal output). Figure 3-22 shows the thermal output of the same strain gauge on steel 1018 and GFRP rebars that is also expressed in Eq 3-1.

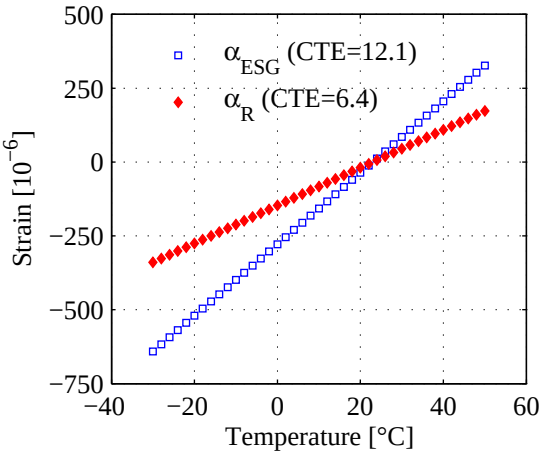

Figure 3-21 CTE of GFRP (6.4/ºC) & 1018 Steel (12.1/ºC)

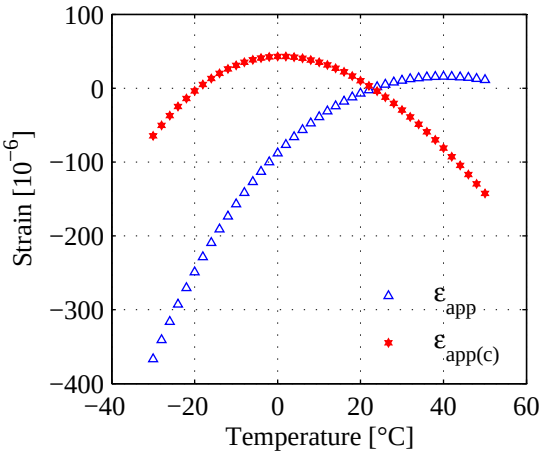

Figure 3-22 Thermal Output for 350 Ω with STC-06 on Steel 1018 and Proposed Corrected Output for GFRP

$$\varepsilon_{corrected} = \varepsilon - \left[\varepsilon_{app} - (\alpha_{\mathrm{ESG}} - \alpha_{\mathrm{R}})\right]$$

or $$\varepsilon_{corrected} = \varepsilon - \varepsilon_{app(c)} \qquad \text{Eq 3-1}$$

Where, $\varepsilon_{corrected}$ is the thermal compensated strain, ε is the strain recorded from the DAQ, ε_{app} is the thermal output from manufacturer, α_{ESG} is the strain due to change in temperature of the material used by manufacturer to obtain the thermal output of strain gauge from a standard temperature, α_R is the strain due to change in temperature of the test material from the standard temperature.

In the current study, two different strain gauges are used for GFRP. The difference between the two is in the thermal output of the strain gauges. The thermal output provided by manufacturer is tuned for a CTE of 12.1 and 4.9 per degree Celsius. Some manufacturers differentiate the strain gauges by a specific self-compensation number. In

this thesis, the two types of strain gauges used on GFRP will be differentiated by the self-compensation number as mentioned in Table 3-7. . For steel, the thermal output of strain gauges are provided on the material with CTE of 12.1 per degree Celsius.

Other than above mentioned procedure for thermal output of strain gauges, dummy gauges were also installed in each slab to get the thermal output of strain gauges for GFRP and steel strands. However this procedure has the dependency of strain readings on one dummy gauge and any error in the dummy readings will be transferred to all the strain gauges in a slab.

For bonding and protecting the strain gauges the following installation procedure was adopted. First, the bars were sanded using a belt sander to remove sand coating. Once the GFRP fibres were about to get exposed, a finer sand paper was used to expose the fibres. During sanding, care was taken to minimise the removal of GFRP fibres. Once the fibres were exposed, the surface was cleaned with acetone that served as a degreasing agent. The strain gauges were then transferred to the bars aligned in proper locations using the manufacturer's recommended tape.

Figure 3-23 Strain Gauges and FOS in Formwork

The strain gauges were bonded using M-Bond AE-10 adhesive and held in place using clamps for minimum of 24 hours as shown in Figure 3-24(a). A minimum curing time of 24 hours was given before soldering the wires on to the strain gauges. After soldering, the strain gauges were coated with M-Coat B nitrite rubber and Teflon tape was applied over the rubber coating before protecting it with butyl rubber and finally wrapping with Linerless Rubber Splicing Tape. The step by step procedure has been illustrated in Figure 3-24, the installed strain gauges and FOS has been shown in Figure 3-23

For steel tendons due to space limitations on the wires, it was not possible to install the same 350 Ω gauges. Thus 120 Ω gauges from Tokyo Sokki Kenkyujo Co., Ltd. were installed. The 120 Ω strain gauges from TML came along with the lead wires. For durability reasons the lead wires were replaced with more durable wires. The procedure adopted to install the ESG's on steel strands was similar to the procedure of ESG installation on GFRP bars.

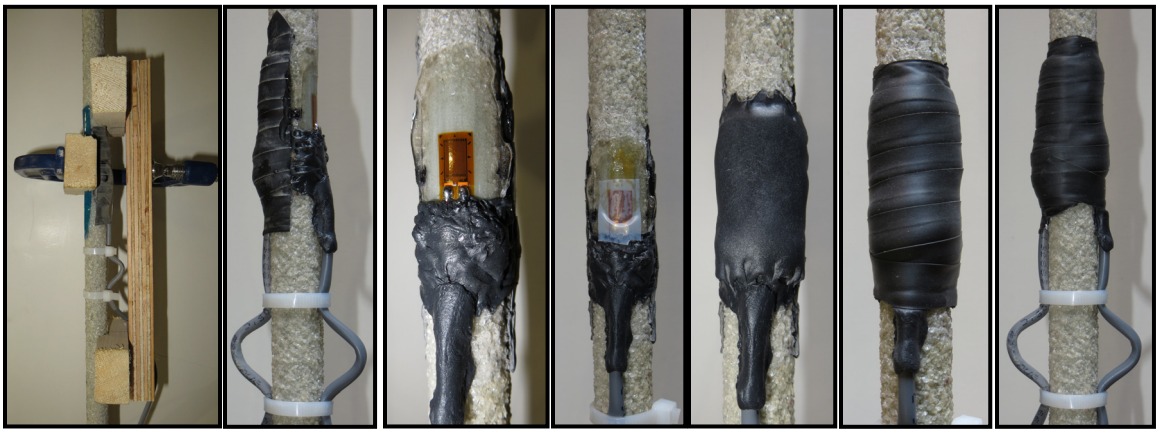

(a) (b) (c) (d) (e) (f) (g)

Figure 3-24 Step by Step Strain Gauge Installation on GFRP rebar
(a) Bonding of Strain Gauges using M-Bond AE-10 Adhesive, (b & c) Lead Wires Soldered to Strain Gauges, (d) Strain Gauge Coated with M-Coat B Nitrite Rubber and Teflon Tape as Applied Over the Rubber Coating, (e) Strain Gauge Protected with Butyl Rubber, (f & g) All the Protecting Components Secured by Linerless Rubber Splicing Tape

For the installation of dummy gauge, a nearly six inch piece of reinforcement was taken and the strain gauge was installed on one end of the rebar/strand. To get the thermal output from this piece of rebar/strand, it is essential that the rebar must expand and contract freely. Thus, its one end was kept in contact with concrete for fast transfer of temperature and, the other end of rebar containing strain gauge was kept inside the plastic tube for free expansion/contraction. To keep the strain gauge end of rebar isolated from concrete, the plastic tube was filled with expending foam.

The details of the installed strain gauges are presented in the Table 3-8

Table 3-8 Details of Strain Gauges and FOS Installed on Slabs

ESG ID	350 Ω (STC-06)		350 Ω (STC-03)		120 Ω		FOS	
Gauge Length	6.35 mm		6.35 mm		2 mm		1.700 to 2.006 mm	
Slab ID	Micro-Measurements				TML		FISO	
	Main	Dummy	Main	Dummy	Main	Dummy	Main	Dummy
S-65-1	-	-	-	-	4	2	1	1
S-65-2	-	-	-	-	4	1	-	-
S-65-3	-	-	-	-	4	1	-	-
F-0-1	6	1	-	-	-	-	1	1
F-0-2	6	1	-	-	-	-	1	-
F-0-3	6	1	-	-	-	-	-	-
F-24-1	6	1	6	1	-	-	1	-
F-24-2	6	1	-	-	-	-	1	-
F-24-3	6	1	-	-	-	-	-	-
F-35-1	6	1	6	1	-	-	1	-
F-35-2	6	1	-	-	-	-	1	-
F-35-3	6	1	-	-	-	-	-	-

3.7.2. Fibre Optic Sensors

One of the tasks of the project is to compare the strain values obtained from fibre optic sensors (FOS) and strain gauges. The selection of fibre optics was mainly based on the availability of strain range and compatibility with the existing DAQ. Both these criteria's were met by the FOS from FISO; the strain range of FOS ranges from -2000×10^{-6} to 8000×10^{-6}.

Total nine FOS were installed on the reinforcing bars in the slabs kept for long term monitoring. Out of these nine, two FOS were installed as dummy gauges; one each on GFRP bar and steel strand. The number of installed FOS has been listed in Table 3-8

However, the installation of FOS was not done as recommended by the manufacturer and two FOS were lost during installation and another one during prestressing. The remaining six FOS are functional. Out of these six only four of them are giving the satisfactory strain readings. The FOS were installed by aligning them on the reinforcement and securing it with the instant adhesive glue over the micro-capillary, rather than about 3 mm away from it. Due to this the micro-capillary was not in direct contact with the reinforcement and had a thick layer of quick glue below it with air bubbles. Once the glue was set, epoxy AE-10 was applied on the exposed fibre. This has resulted in little reliability in the strain readings obtained from FOS.

3.7.3. Thermocouples

Temperature recording is one of the important and critical parts in correcting the strains obtained from strain gauges. The thermocouples used were manufactured by Omega Engineering, Inc and the properties are listed in Table 3-9

Table 3-9 Thermocouple Properties

Material	Diameter [mm]	Gauge	Insulation	Part#
Copper-Constantan	0.51	24	Teflon	5TC-TT-T-24-36

3.7.4. Deflection Measurement

3.7.4.1. Linear Variable Displacement Transducers (LVDTs)

LVDT's were used to measure the deflection during precracking and testing of slabs. For the slabs tested till failure, six LVDTs were used to capture the deflection under load at the location of all five rulers and an additional LVDT was installed at midspan (Figure 3-26) to check for the twisting of the slab during testing. However both the LVDTs has recorded the same reading and twisting was not observed. Two LVDTs were placed at the support points to observe the deflection due to the compression of the rubber pads as shown in Figure 3-25. It was found that the deflection was negligible, thus the two LVDTs at the support points were not installed for precracking the slabs.

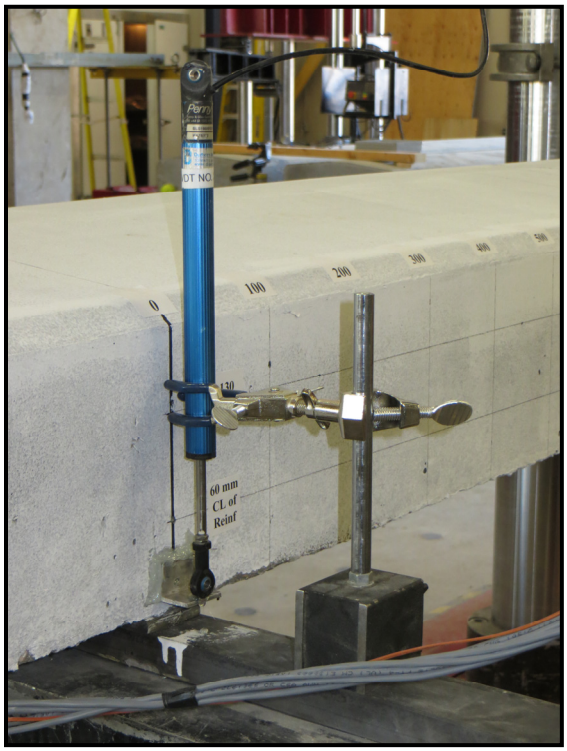

Figure 3-25 LVDT at Supports

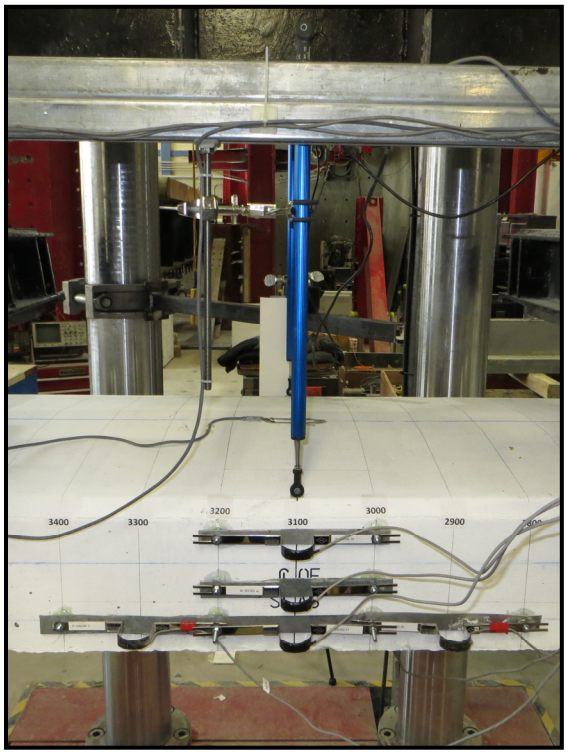

Figure 3-26 Midspan LVDT

The LVDTs were placed at the same location of embedded rulers in the slabs as listed in Table 3-10. The location of rulers is illustrated in Figure 3-27.

Table 3-10 LVDT Location on Test Slabs

Ruler	R1/R5	R2/R4	R3	R4/R2	R5/R1
LVDT number	LVDT-16	LVDT-25	LVDT-24 LVDT-26	LVDT-27	LVDT-22

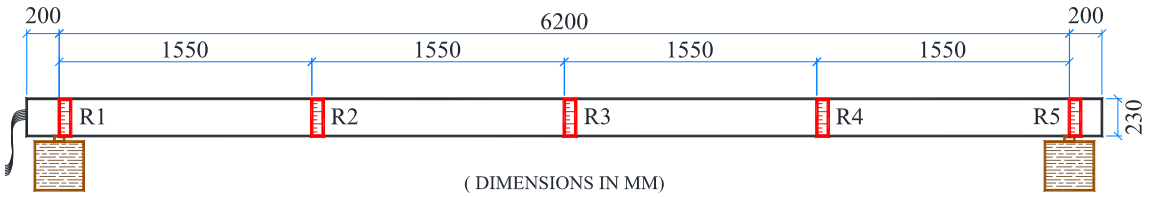

Figure 3-27 Location of Rulers/LVDTs for Deflection Measurement

To get accurate readings, the LVDTs were recalibrated before each destructive testing. However for precracking of eight slabs, calibration was done only two times due to the absence of impact on the LVDT's during cracking.

3.7.4.2. Laser Level and Rulers

The long term deflections of slabs are captured with the help of laser level and five rulers inserted in each slabs at the time of casting. Inserting the steel rulers in the slab at the support points has to provide the datum point and all the deflection readings were calculated with respect to these two rulers. Thus it became essential to record a set of readings before lifting and cutting the bars/strands. This first set of reading will be used as a correction factor to all other readings and has enabled to capture the camber/initial deflection. The method adopted to record the deflection has been graphically presented in Figure 3-28

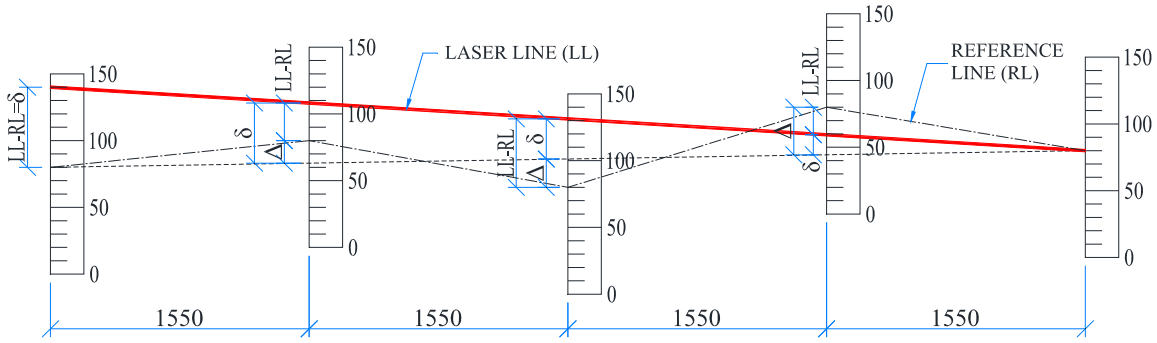

Figure 3-28 Graphical Representation of Deflection Calculation

Since the accuracy of this method to measure the deflection was unknown, thus five sets of deflection readings were taken by placing the laser level at five different locations on the same set of rulers. When analysed, the difference in the deflection readings was within 0.2 mm, thus it can be comfortably claimed that the presented results will be accurate within 1 mm.

To measure the deflection, the readings on rulers are recorded by taking high resolution photos. Taking the pictures enabled us to review the results in future.

Before the use of laser level, for the slabs cast at Lafarge Winnipeg, the deflections were captured by the use of water level pipe. Here also high resolution pictures were recorded for future reference. The continuity of the readings was not compromised because the procedure adopted for both laser and water level pipe had the same reference points.

This method of deflection measurement has been adopted due to the compulsion of moving the slabs from Lafarge to the University. They also had to be moved around the structural lab for pre-cracking. By the use of laser and rulers it became possible to get the complete deflection history of the slabs.

Since self-weight of the slab is a dominating load, thus care has been taken to maintain the same support conditions at all times to avoid creep reversal phenomenon.

For the slabs cast at the University, on day one nearly 3 to 4 deflection readings were recorded under the influence of self-weight of the slab. Later on, the time interval was progressively increased. For the slabs cast at Lafarge, limited time window for capturing the deflection was available, and therefore initially it was recorded only once a day.

3.7.5. Electrical Pi-Gauges

TML Pi-Gauges (Displacement Transducers) were used to record the longitudinal strain at concrete surface across the depth of slab during testing/precracking. The typical arrangement is shown in Figure 3-29. The location of Pi-Gauges across the section at mid-span is shown in Figure 4-9.

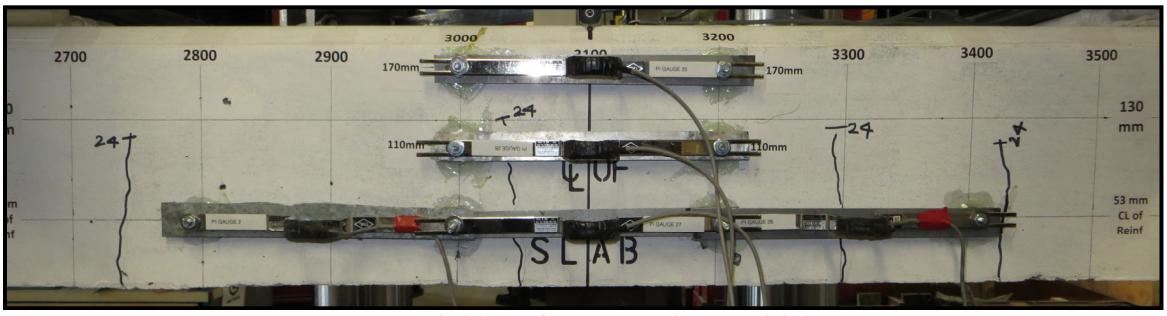

Figure 3-29 Pi-Gauges on Slab F-24-3

Total of six 200 mm gauge length Pi-gauges were used on each slab tested to failure, five on the side face and one at the bottom. Before each installation the gauges were calibrated on the calibration table. While calibrating it was observed that the scale factor slightly varies with the range of strain and also with the sign of strains (compressive or tensile) thus each Pi-gauge was calibrated for a different strain range keeping them close to the predicted maximum strain readings to achieve maximum accuracy.

The strains obtained were used to plot the strain profile along the depth of the slab and to capture crack width with the variation of the applied load.

3.7.6. Data Acquisition Systems

3.7.6.1. P-3500 Strain Indicator

P-3500 (Figure 3-31) Strain Indicator with SB-10 from Vishay Measurements Group, Inc. is being used for long term monitoring of strains. Quarter-bridge with three lead wire connection is being used for strain recording for both 120 Ω and 350 Ω gauges. The fine balance switch of P-3500 was kept at 5.00 and the 'AMP ZERO' was set to zero reading for the reference dummy gauge and all the readings were taken from the same instrument settings.

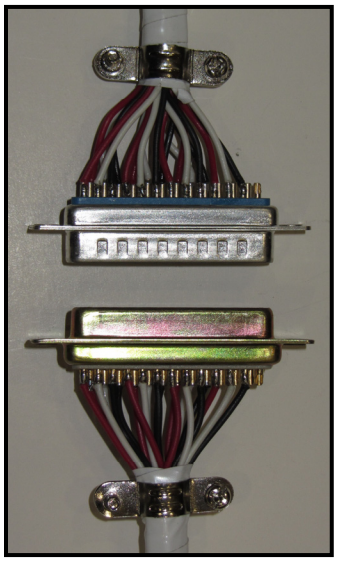

Figure 3-30 DB-25 Connector

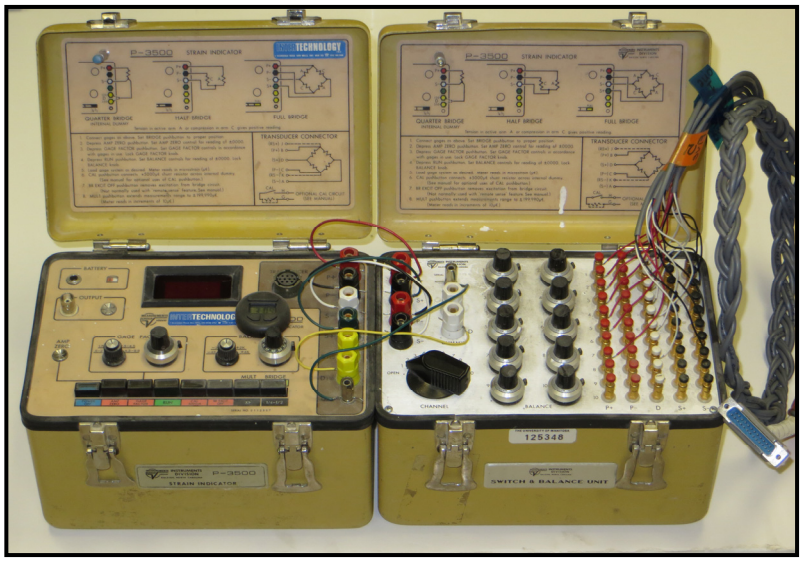

Figure 3-31 P-3500 Strain Indicator

To get accurate strain readings from the strain gauges, the readings were acquired from DAQ during early morning time when the sun rays were not over the slabs to avoid differential temperature in the slab. Also, at early morning the variation of temperature in the surrounding area is minimal, thus P-3500 itself is not subjected to differential temperature. In the initial trial it was observed that P-3500 shall be given minimum of nearly one and one half hours before taking the readings. This provides the sufficient window to the DAQ for stabilizing with the surrounding temperature and humidity level.

Also the readings were avoided in rainy conditions when the humidity levels went beyond 90%.

To avoid the error due to the electromagnetic interference from AC line all the readings were taken by powering the Strain Indicator with batteries. To facilitate easy switching of connections between strain gauges and DAQ a DB-25 connector was installed on each of the test slabs and P-3500. A photograph of the connection is shown in Figure 3-30.

3.7.6.2. DAQ from National Instruments

This DAQ (Figure 3-32) was used for recording the data during testing and cracking of the slabs. The data acquired was obtained from 350 Ω and 120 Ω strain gauges, LVDT's, Pi-Gauges and the loading from MTS machine.

Figure 3-32 DAQ – National Instruments

3.7.6.3. Fibre Optic Sensors Readout Units (DMI-16 and FTI-10)

Two fibre optic sensor readout units DMI-16 and FTI-10 from FISO Technologies, inc. were used to obtain the strain data from FOS. Both the units were checked against each other and the difference was only 2×10^{-6} thus the readings were not dependent on the readout units and they can be combined without correcting the strain values.

FTI-10

This is a single channel handheld readout unit and can be connected to only one FOS at a time. In this project it has been used mainly to obtain the discrete strain values during long term observation due to its ease of transporting it from one place to other

Figure 3-33 FTI-10

DMI-16

This FISO read out unit has 16 channels and it was used to record the strains during prestressing, curing and loading under self weight for the few initial days.

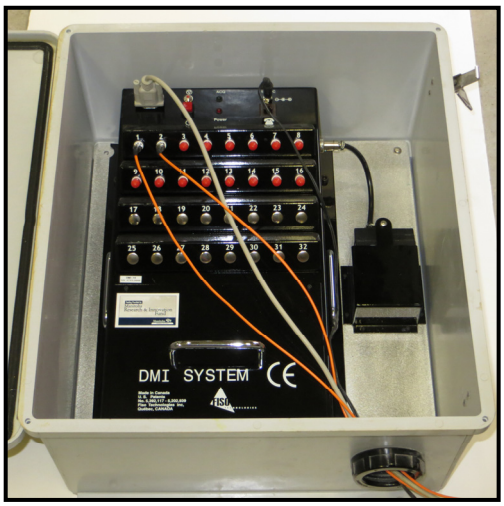

Figure 3-34 DMI-16

3.7.6.1. TC-31K Digital Strainmeter

To measure the temperature from thermocouples embeded inside the concrete, digital strainmeter TC-31K from Tokyo Sokki Kenkyujo Co., Ltd. is being used. This hendheld unit can be operated by battery power and was suitable for this project.

Figure 3-35 TC-31K

4. Experimental Results and Analysis of Data

In this chapter the results obtained from the experimental investigation are compared and discussed with the theoretical calculations. The comparison includes the load- deflection behaviour and the suitability of existing methods for predicting deflection for prestressed GFRP slabs. The observation includes the moment curvature results and the strain profile across the section to compare the accuracy achieved in the analysis with explanations of some possible reasons for deviation.

The main aim of this experiment is to determine the long term behaviour of GFRP prestressed concrete slabs. For long term deflection ACI 440.4R-04 (2004) and CSA S806-12 (2012) recommend the use of long term multipliers of immediate deflection results. However long term deflections obtained from long term multipliers are entirely dependent on the immediate deflections. Thus any small error included in the immediate deflection will be having the same multiplying effect on the long term deflection results. This requires an accurate determination of immediate deflection by considering the actual material properties of concrete and GFRP.

A detailed long term analysis has been performed with age adjusted effective modulus method incorporating the creep and shrinkage obtained from ACI 209R-92 (1992), CEB MC90-99 (1999) and Bažant-Baweja B3 model (1995) and examining their suitability for GFRP prestressed members.

4.1. Load-Deflection Analysis

The design details of all tested samples, including total prestressing force after anchorage seating loss in the slabs are listed in Table 4-1 below.

Table 4-1 Prestressing Details

Slab Type	Number of Samples	Total Prestressing Force	Corresponding Prestress Levels	Reinforcement Type
S - 65	3	P (480 kN)	65 %	Steel Strands
F - 0	3	0	0	GFRP
F - 24	3	0.5 P (240 kN)	24 %	GFRP
F - 35	3	0.75 P (360 kN)	35 %	GFRP

The primary guideline in deciding the level of prestressing was the prescribed limit in CSA S6-06 (2006). The second guideline was the amount of total prestressing force with respect to the conventional slabs cast for Brookside Cemetery at Winnipeg. Both criteria lead to the values outlined in Table 4-1. These limits will allow us to validate the prestressing limit in GFRP rebar.

The total axial stiffness of the reinforcing bars/ prestressing tendons is presented in Table 4-2. For steel prestressing tendons CSA A23.3-04 (2004) suggests the value of modulus of elasticity from 190 000 to 200 000 MPa, Lafarge Winnipeg has reported the modulus at 65% prestress as shown in Table 4-2

Table 4-2 Axial Rigidity of Longitudinal Reinforcement

Reinforcement Material	Total Area of Reinforcement [mm^2]	Modulus of Elasticity [MPa]	Axial Rigidity [10^6 N]
Low Relaxation Steel	396	198000	79.2
GFRP	1187.6	54950	65.26

The GFRP reinforced/prestressed slabs have 17.6% less axial rigidity than steel prestressed slabs. Thus the two major variables between steel and GFRP prestressed slabs are the axial rigidity and prestressing force.

Out of total of 12 test slabs, destructive testing was performed on each type of slab, thus short term tests were performed on 4 slabs. The support conditions were kept similar to long term loading i.e. the span of slabs was 6200 mm. Load deflection results of all four slabs are shown in Figure 4-1

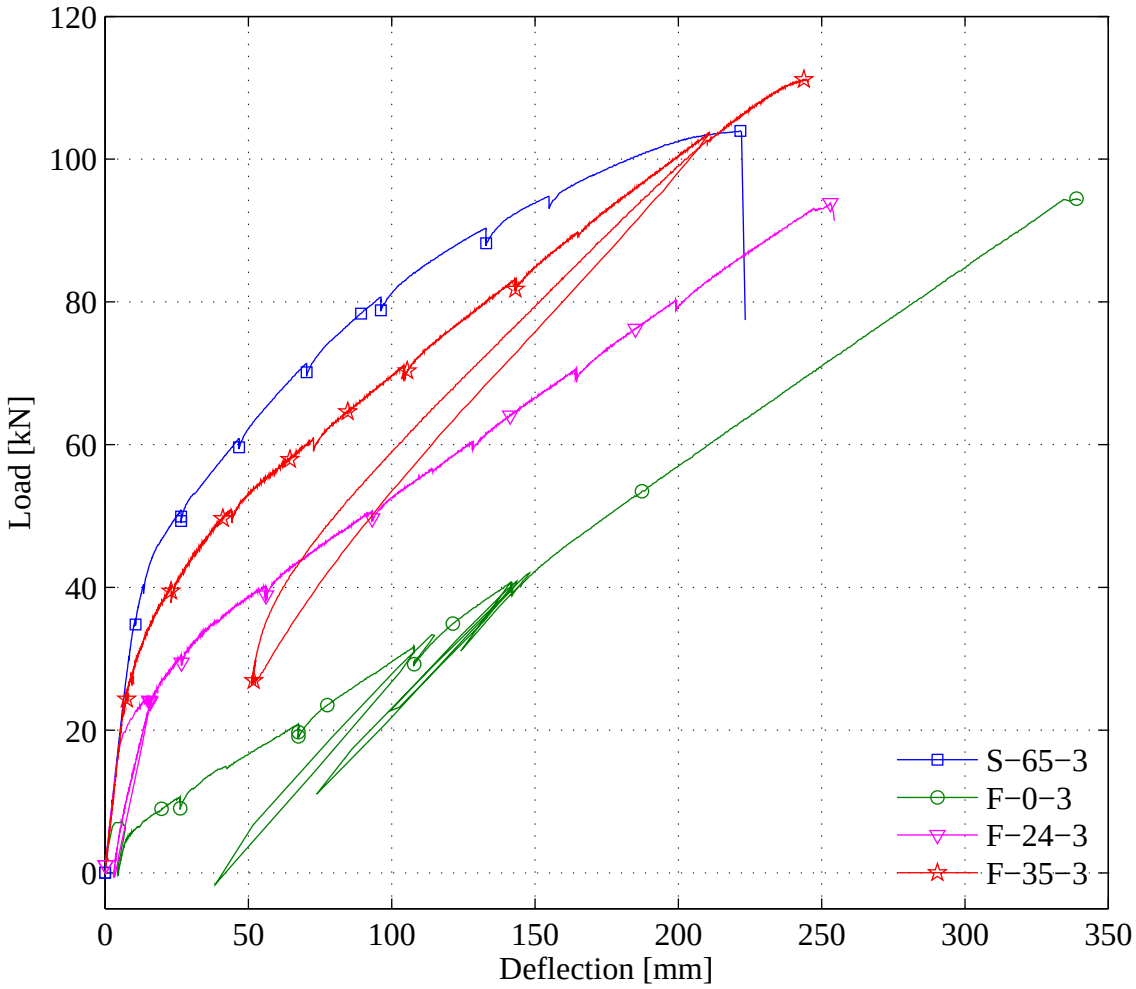

Figure 4-1 Load-Deflection Response from Short Term Tests

The results shown in Figure 4-1 do not include the deflections due to self-weight of the slab. In the theoretical analysis for deflections, the effect of self-weight has been included and the analytical results are adjusted for comparing them with experimental values.

For slabs F-0-3, F-24-3 and F-35-3 a loop can be seen in the load deflection response as shown in Figure 4-1. This is due to the resetting of MTS machine in between the test because of a faulty cable.

As the GFRP prestress increases, the load-deflection behaviour of the slab approaches that of steel prestressed slab reflecting the influence of prestressing force on flexural behaviour of the slabs after cracking. However the modulus of elasticity of low relaxation steel strands declines with the increase in strain due to which the later part of the load-deflection curve of slab F-35-3 becomes stiffer than slab S-65-3.

The methods adopted for the determination of load-deflection response were discussed in section 2.3. The theoretical immediate deflection and change in strain are compared with the observed values in Table 4-3. For slabs F-24-2 and F-35-2 the immediate deflection results are not consistent in their category due to the reduced self weight of slab.

It should be noted that the initial deflection readings can have a variation of $\pm$ 1 mm due to the error in recording initial correction factor. Also, the immediate deflection error for slabs F-0-1, F-0-2 and F-0-3 may reach up to 1.5mm due to the combined effect of initial correction error and use of water level in the first few readings of these slabs. Considering these limitations, the above theoretical values are in good comparison with the experimental results.

Table 4-3 Immediate Deflection and Corresponding Strain due to Self-Weight

Slab ID	Immediate Deflection [mm]		Strain in rebar [10^{-6}]	
	Experimental	Sectional Analysis	Experimental	Sectional Analysis
F-0-1	-	4.10	33	43
F-0-2	3.3	4.33	61	56
F-0-3	1.5	3.58	35	46.8
F-24-1	-0.4	-0.40	-80	-63
F-24-2	-1.6	-0.90	-115	-92
F-24-3	-1.6	-0.30	-83	-63
F-35-1	-2.3	-2.92	-130	-127
F-35-2	-5.0	-4.45	-208	-185
F-35-3	-3.8	-3.07	-145	-134
S-65-1	-	-4.19	-167	-161
S-65-2	-	-4.20	-217	-175
S-65-3	-	-3.10	-185	-132.5

In the following section, the load-deflection results obtained from CSA S806-12 (2012), ISIS Design Manual No. 3 (2007), ACI 440.1R-06 (2006), ACI 440.4R-04 (2004) and modified Bischoff method (Bischoff et al., 2011) are discussed. It should be noted that for short term load-deflection analysis, the cracking moment is obtained by using the modulus of rupture as suggested in CSA S806-12 (2012).

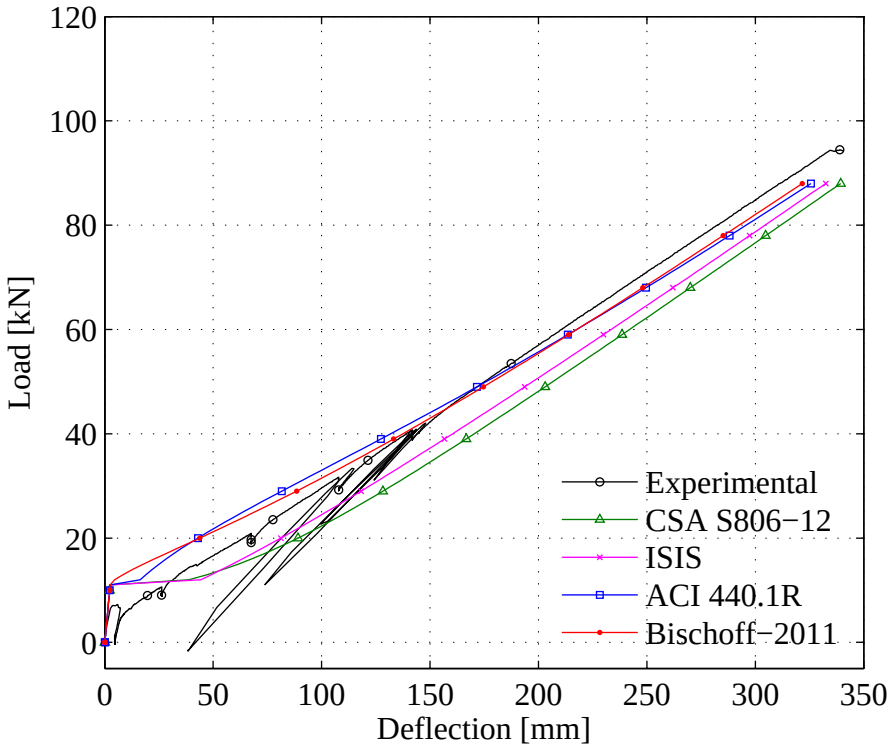

Figure 4-2 F-0-3 Load-Deflection

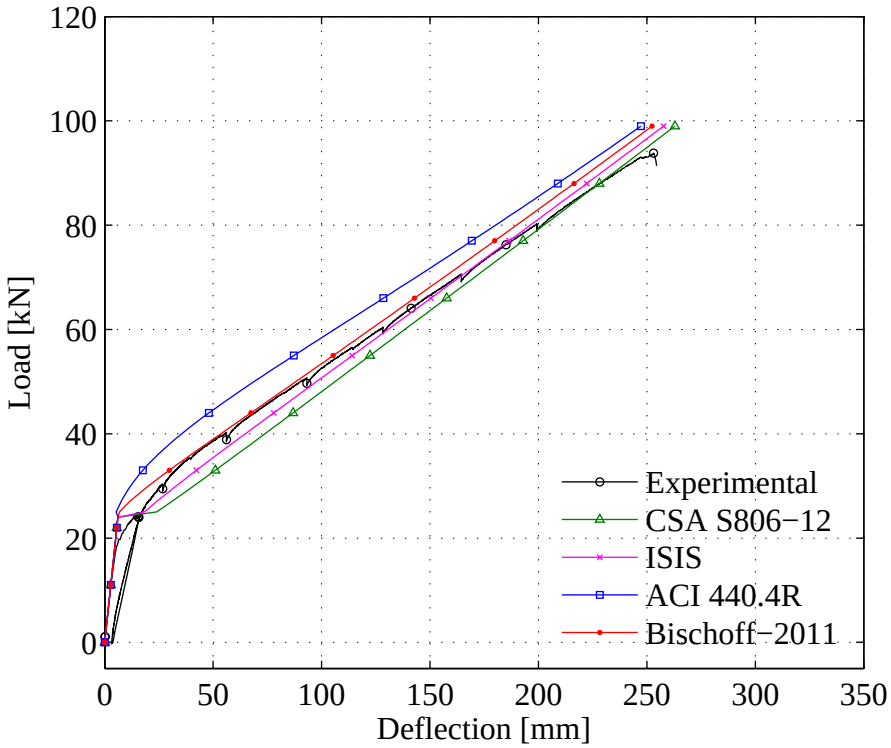

Figure 4-3 F-24-3 Load-Deflection

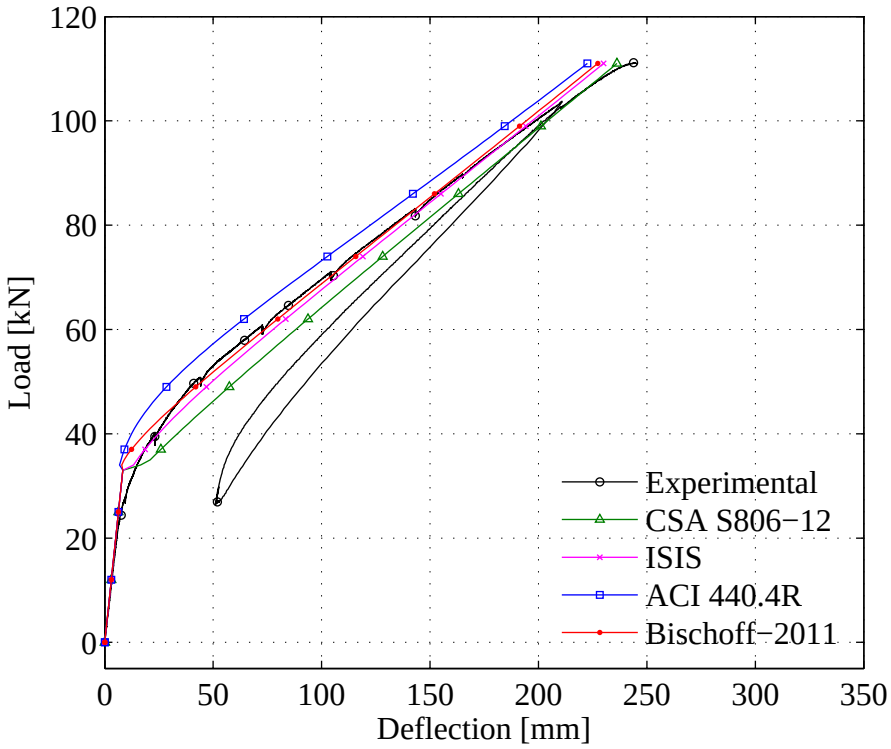

Figure 4-4 F-35-3 Load-Deflection

It is also noted that the influence of shrinkage resistant stresses has greatly influenced the deflection near cracking load and has followed the same pattern as discussed by Gilbert (1999) and Scanlon and Bischoff (2008).

4.1.1. Modes of Failure

The presented failure loads were obtained from the examination of recorded videos and from the observation of post failure condition of the slabs. The pictures presented from Figure 4-5 to Figure 4-8 show the condition of slabs just after the initiation of failure, and were extracted from recorded videos.

The failure criteria for the determination of type of failure was based on the maximum concrete strain of 3500×10^{-6} as per CSA S806-12 (2012), CSA A23.3-04 (2004) and the

absolute GFRP strain (obtained experimentally) of 15900 $\times 10^{-6}$. The failure load and type of failure are presented in Table 4-4.

Table 4-4 Failure Load from Short Term Destructive Testing

Slab ID		F-0-3	F-24-3	F-35-3	S-65-3
Failure Load [kN]	Experimental	94.5	93.8	111.2	104
	Cross-sectional Analysis	88	99	111	93.4 †
	Error [%]	7.35	-5.2	0.15	11.3
Type of Failure	Observed	Compression	Shear	Tension	Compression
	Cross-sectional Analysis	Compression	Compression	Compression	Compression†
Strain at Failure Load (Theoretical) [10^{-6}]	Concrete	3500	3488	3483	-
	Reinforcement	12267	10134+3040 = 13174	9619+4626 =14245	8924+4955 =13879 †
Reinforcement Strain at Failure Load (Experimental) [10^{-6}]		13084	9383+3040 =12423	9279+4626 =13905	8396+5268 =13664

†Results from Response-2000

Table 4-4 illustrates that the percentage error in the failure load is within 10% of the experimental values and also compares the analysis and experimental strains in the reinforcement.

Figure 4-5 Slab F-0-3 (Compression Failure)

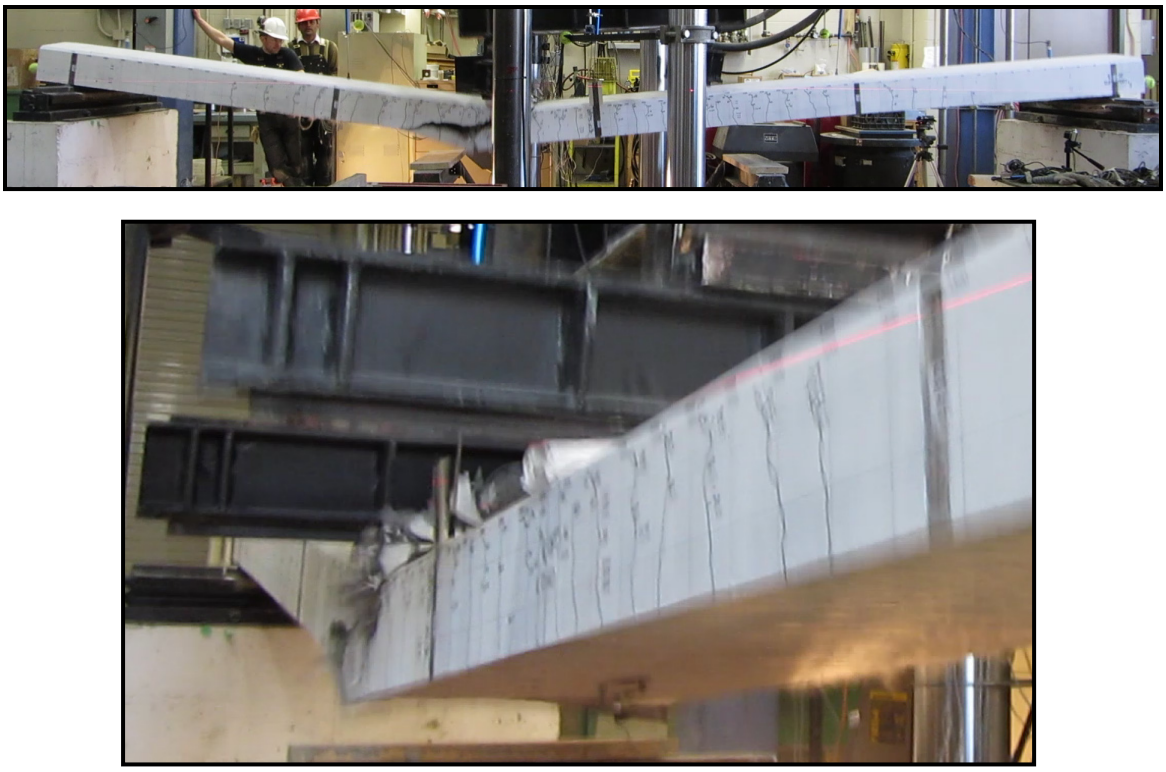

Figure 4-6 Slab F-24-3 (Shear Failure)

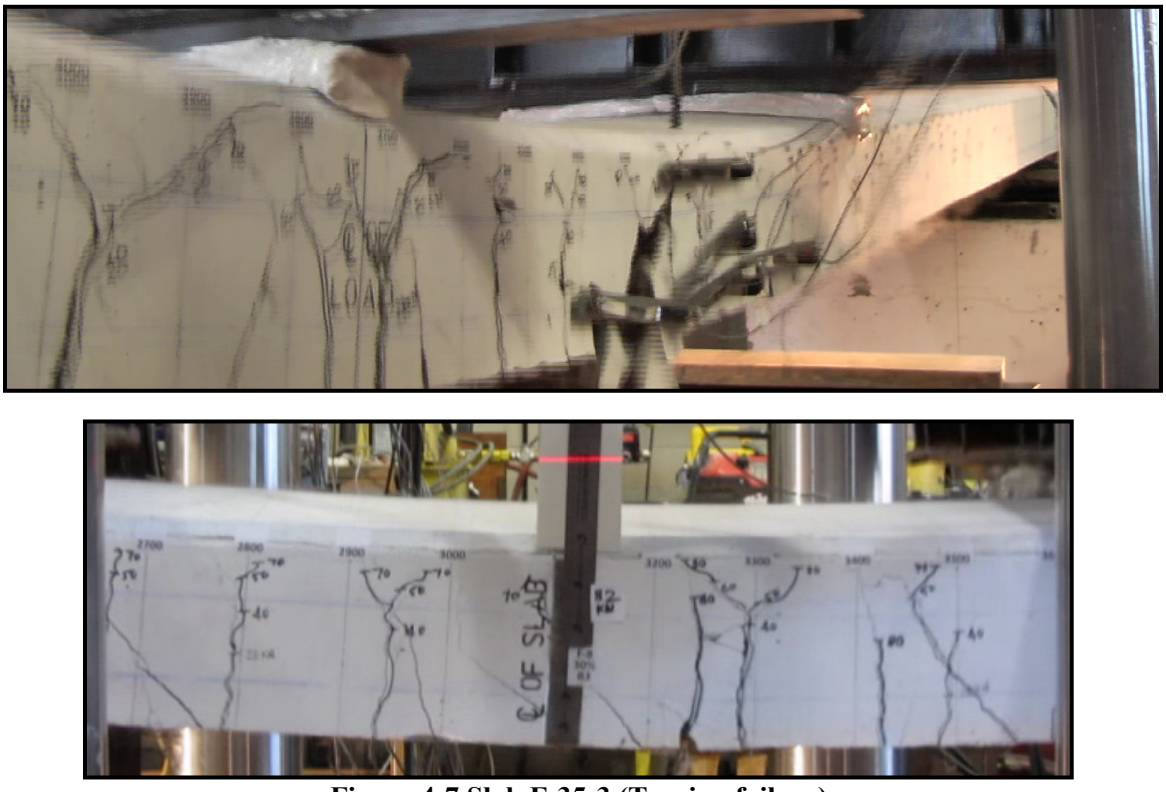

Figure 4-7 Slab F-35-3 (Tension failure)

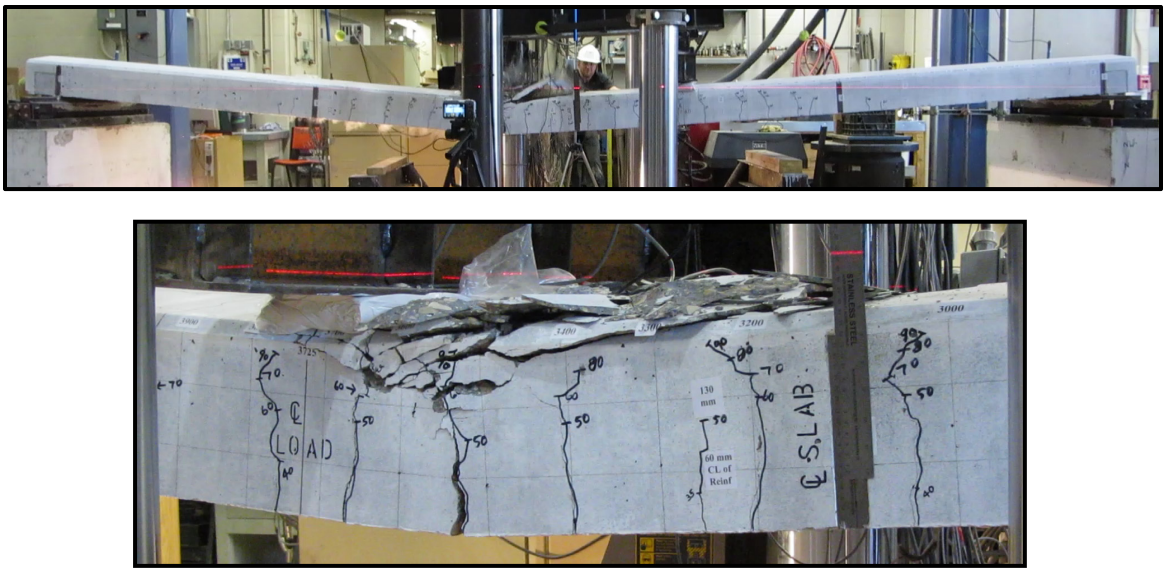

Figure 4-8 Slab S-65-3 (Compression Failure)

4.2. Cross-Sectional Analysis

Due to large variation of the properties of concrete, in terms of compressive strength, air content (from 5% to 15%) etc., the analysis has been performed on the basis of actual properties of concrete and reinforcement. The strain compatibility approach has been employed in the cross-sectional analysis of all the slabs. The procedure of analysis can be referred to in Appendix-C.

It shall be noted that the effect of shrinkage on the reduction of cracking moment is not considered in the short term analysis. The loss in prestressing force due to creep, shrinkage and relaxation for the pretensioned slabs is obtained from the experimental strain data and presented in Table 4-8.

4.2.1. Moment-Curvature (MC) Relation

The moment curvature diagram was obtained at mid span with the help of Pi gauges and ESG installed on concrete surface. The location of each of them is indicated in Figure 4-9.

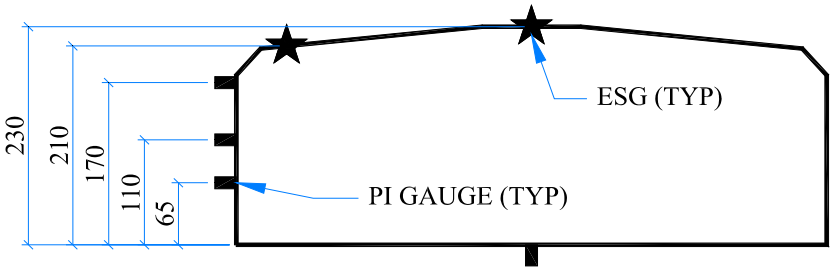

Figure 4-9(a) Slab F-0-3

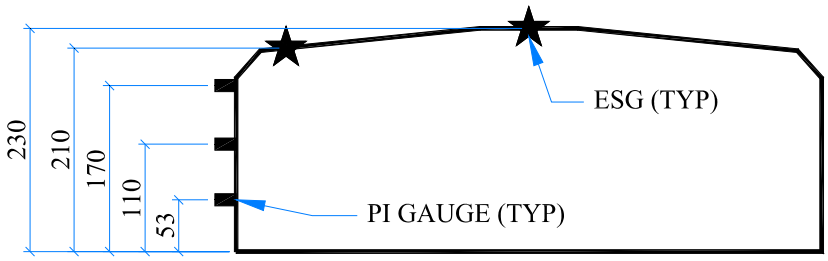

Figure 4-9(b) Slab F-24-3

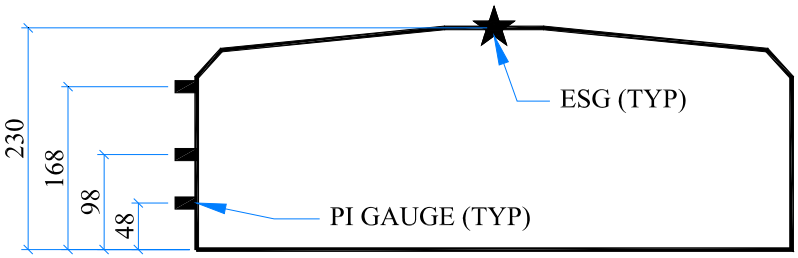

Figure 4-9(c) Slab F-35-3

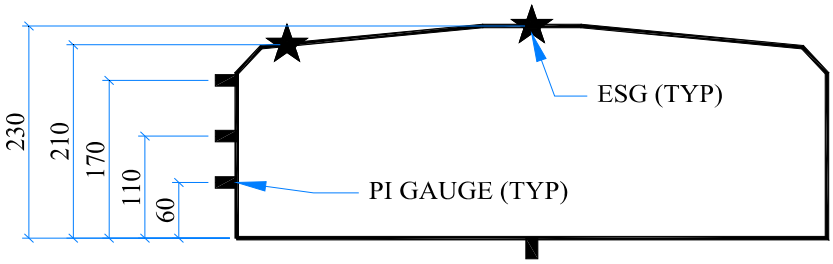

Figure 4-9 (d) Slab S-65-3

Figure 4-9 Instrumentation for Destructive Testing at Mid Span

The curvature at midspan was determined through linear regression using method of least squares from the recorded readings. Figure 4-10 shows the moment curvature relation of the slabs tested till failure.

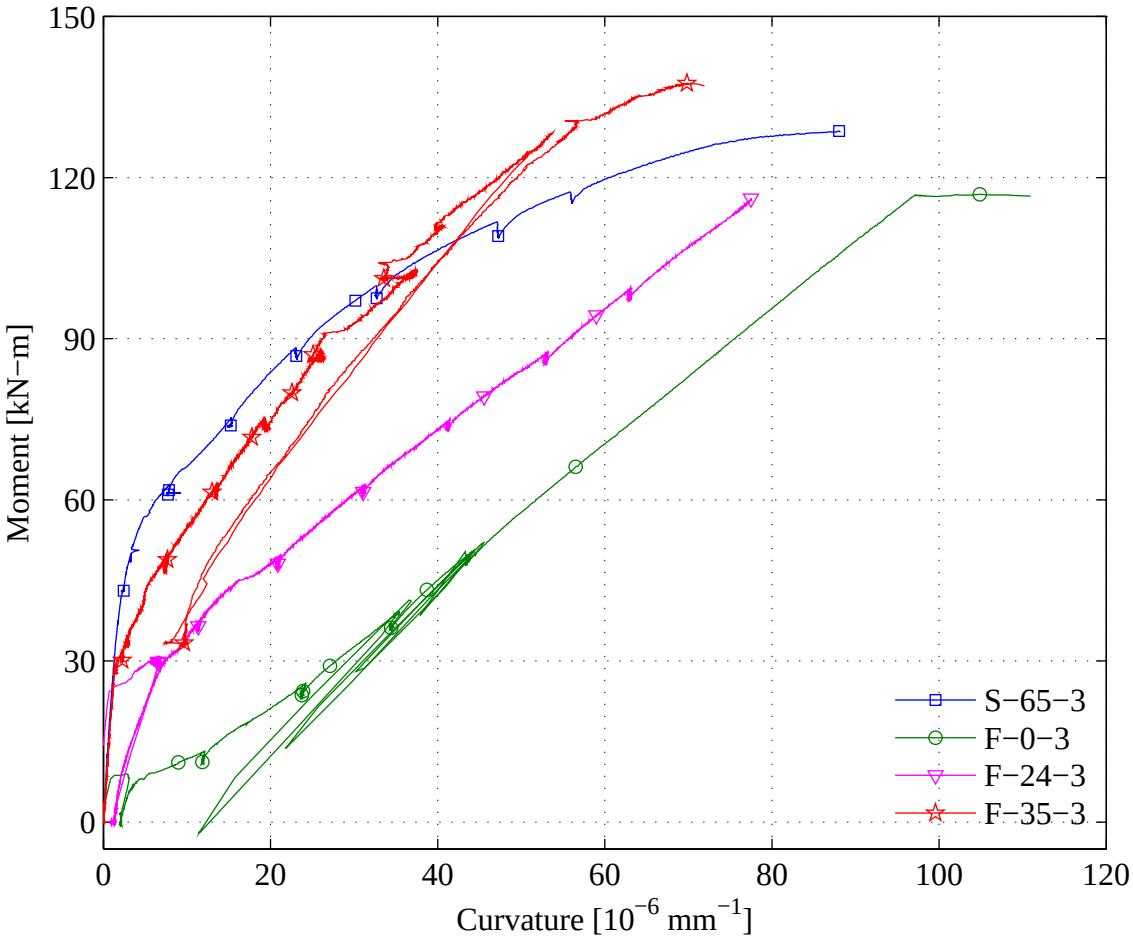

Figure 4-10 Moment Curvature at Mid Span from Short Term Tests

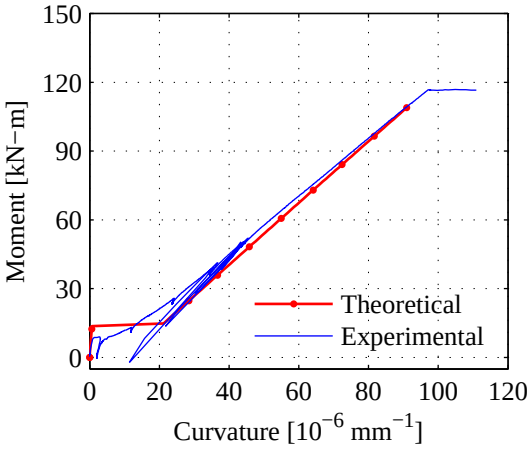

Figure 4-11 MC of Slab F-0-3

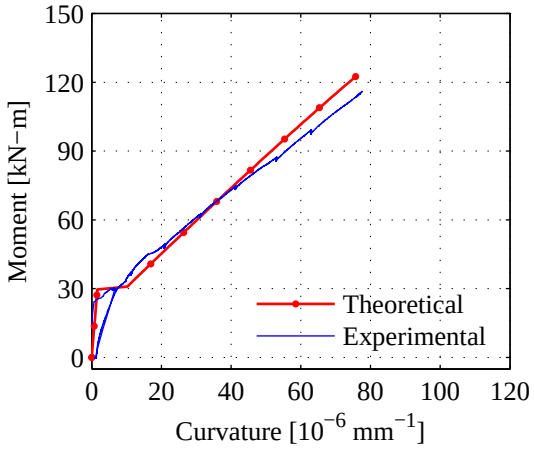

Figure 4-12 MC of Slab F-24-3

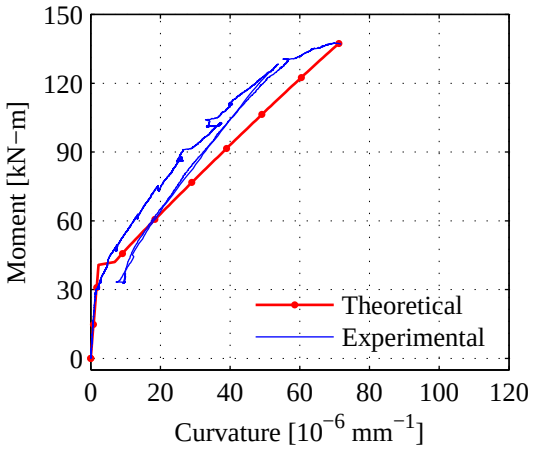

Figure 4-13 MC of Slab F-35-3

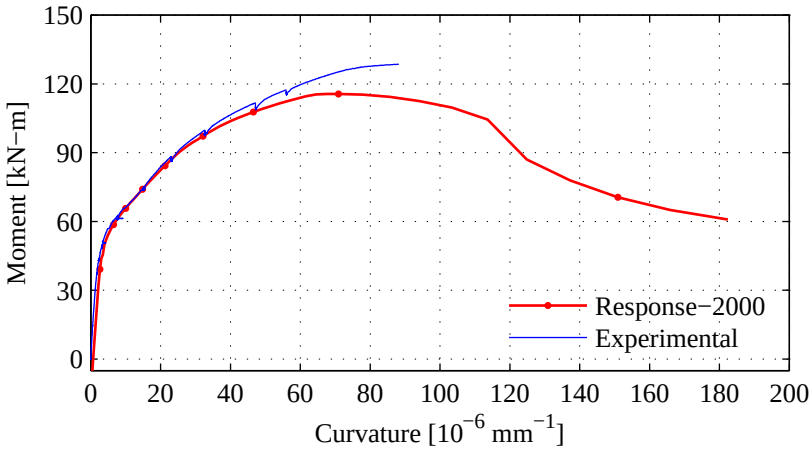

Figure 4-14 MC of Slab S-65-3

For GFRP reinforced/prestressed slabs, the theoretical calculation of moment curvature is performed from the cross-sectional analysis by strain compatibility approach. A mathematical computation software Maple was used to develop the code and the results were obtained with an increment of moment of 1.00 kN-M. However, the steel prestressed section was analyzed with the help of computer program Response-2000. The comparison is shown from Figure 4-11 to Figure 4-14. It can be seen that the analysis is able to predict the curvature very well. The mean relative error at ultimate load for slab F-0-3, F-24-3, and F-35-3 is -0.4%, 7.4% and -2.9%, respectively. Whereas, the average

mean post cracking relative error of moment curvature for slab F-0-3, F-24-3, and F-35-3 is -7.5%, -2.5% and -24.8%, respectively.

4.2.2. Mid-Span Strain in Reinforcement

All the longitudinal rebars/strands were instrumented with a strain gauge at mid-span. The theoretical and observed strains are compared from Figure 4-15 to Figure 4-18. The mean relative error at ultimate load for slab F-0-3, F-24-3, and F-35-3 is -6.3%, -2.1% and -3.7%, respectively. Whereas, the average mean post cracking relative error of strain in reinforcement for slab F-0-3, F-24-3, and F-35-3 is -10.1%, -1.1% and -5.9%, respectively.

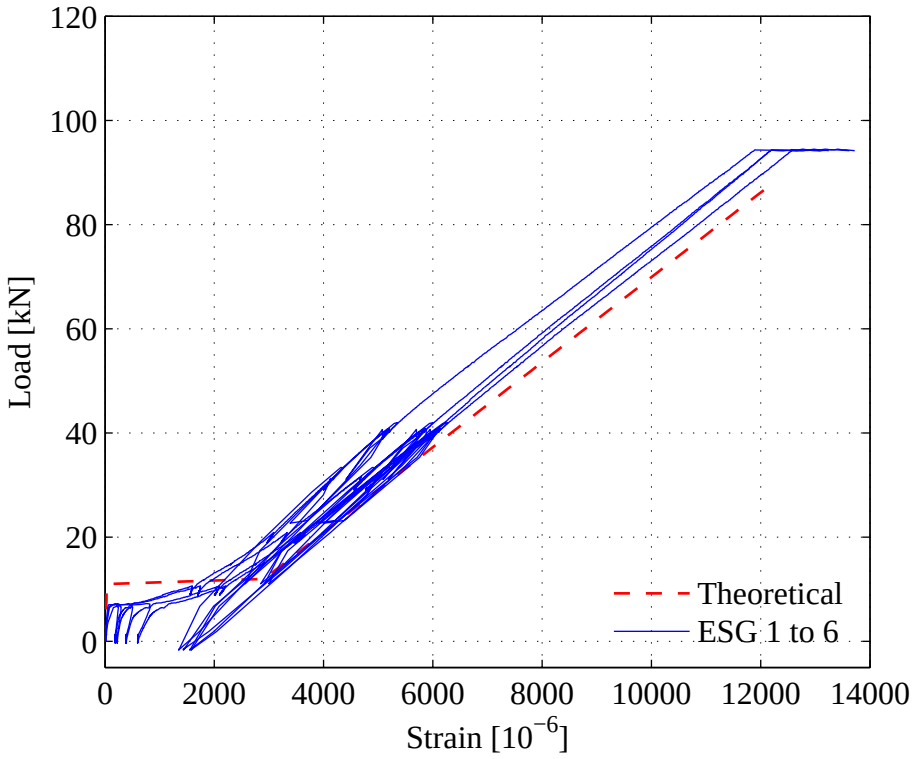

Figure 4-15 Rebar Strain-Load F-0-3

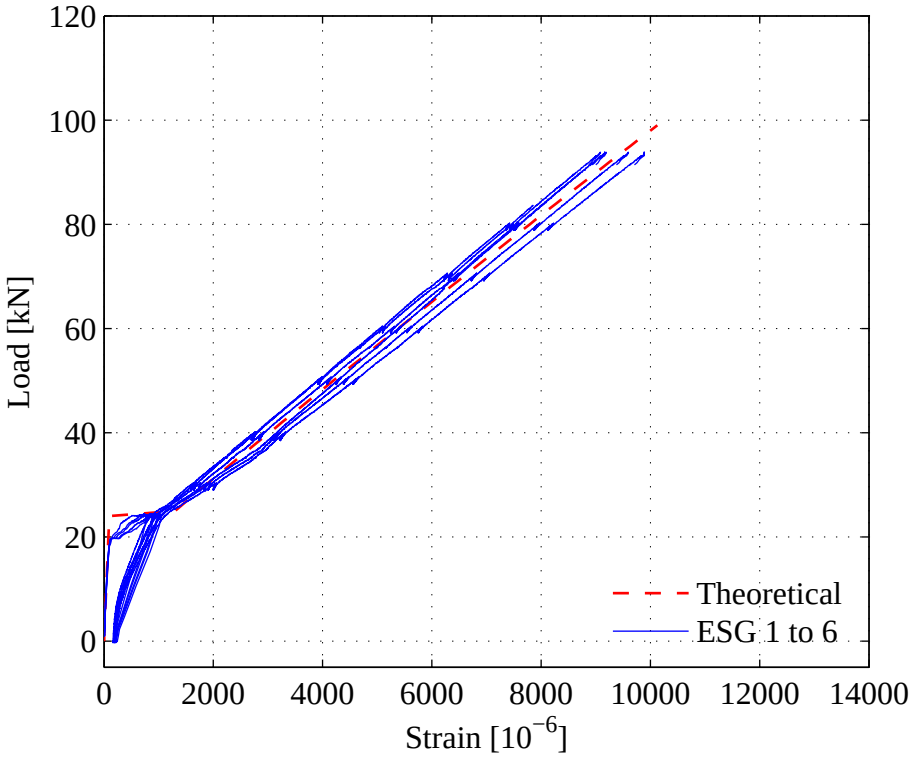

Figure 4-16 Rebar Strain-Load F-24-3

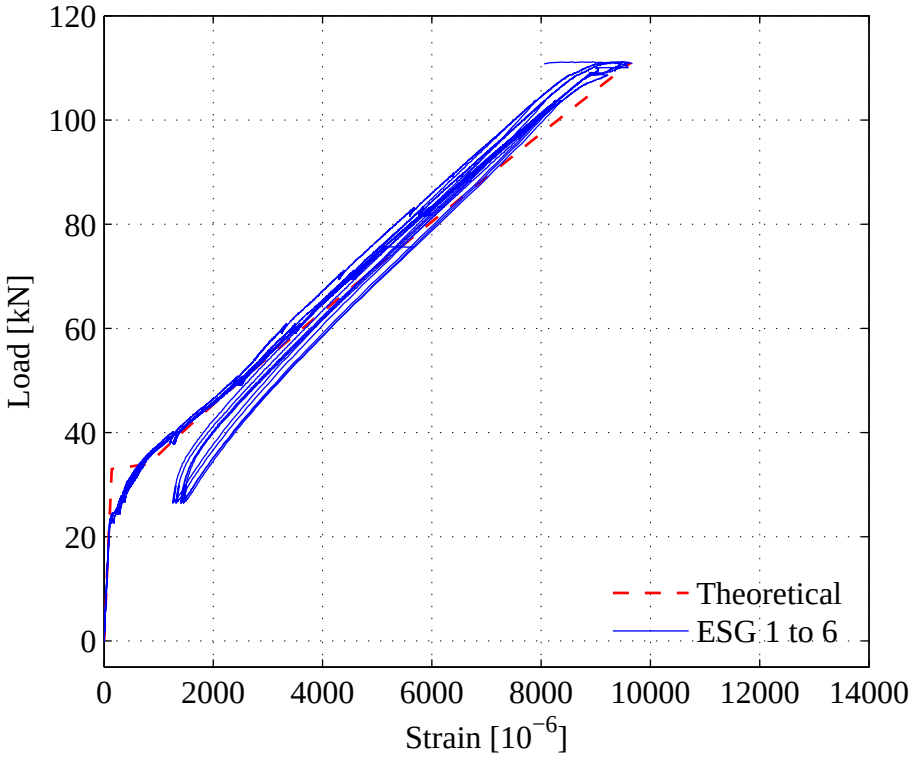

Figure 4-17 Rebar Strain-Load F-35-3

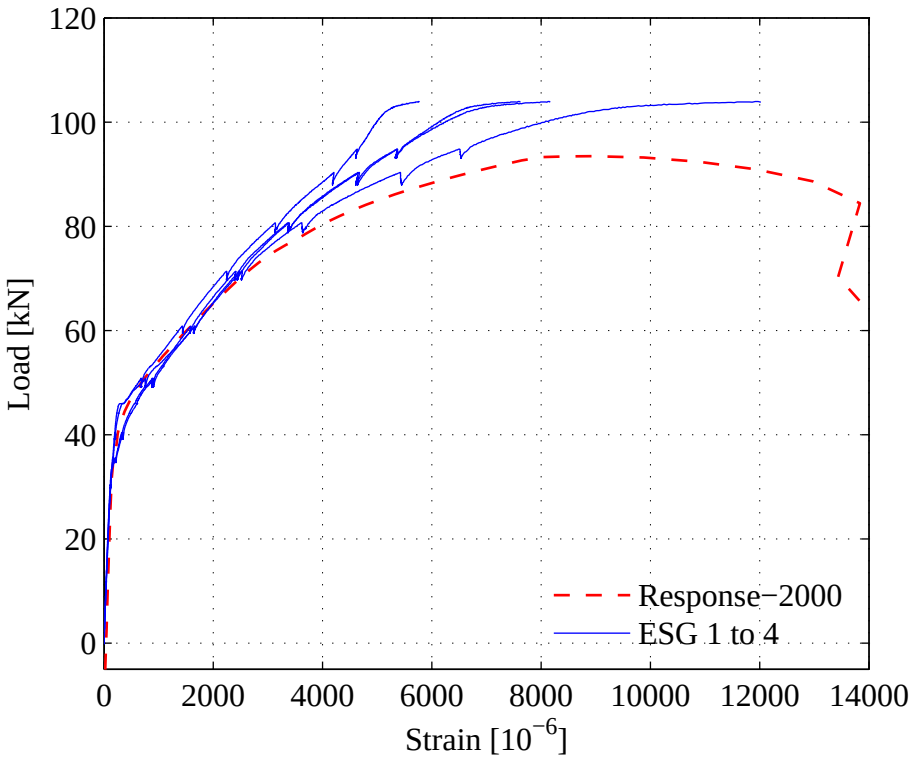

Figure 4-18 Rebar Strain-Load S-65-3

4.2.3. Mid-Span Compressive Strain in Concrete

The compressive strain in concrete from the ESG at the top face of slab is compared below with the analysis results obtained by cross-sectional analysis and Response-2000.

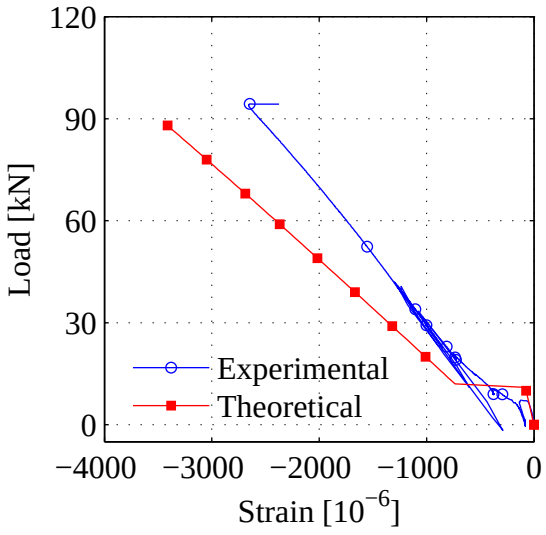

Figure 4-19 Concrete Strain Slab F-0-3 (Compression Failure)

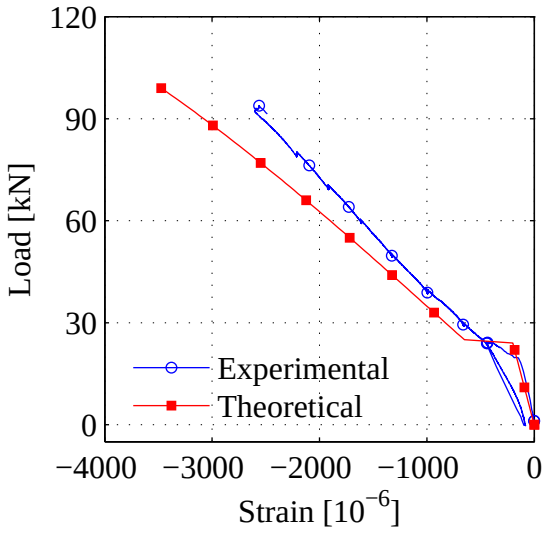

Figure 4-20 Concrete Strain Slab F-24-3 (Shear Failure)

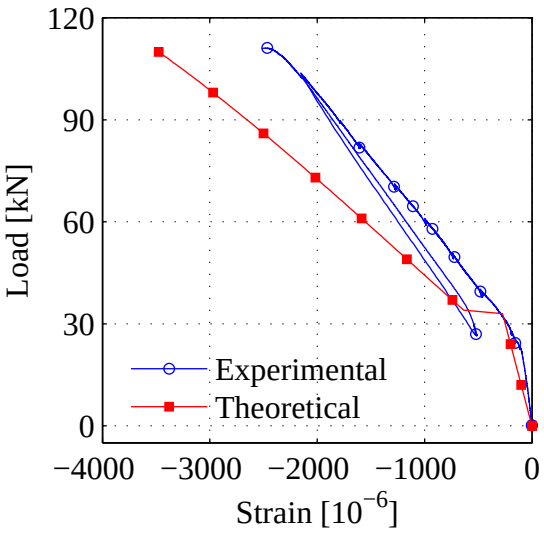

Figure 4-21 Concrete Strain Slab F-35-3 (Tension Failure)

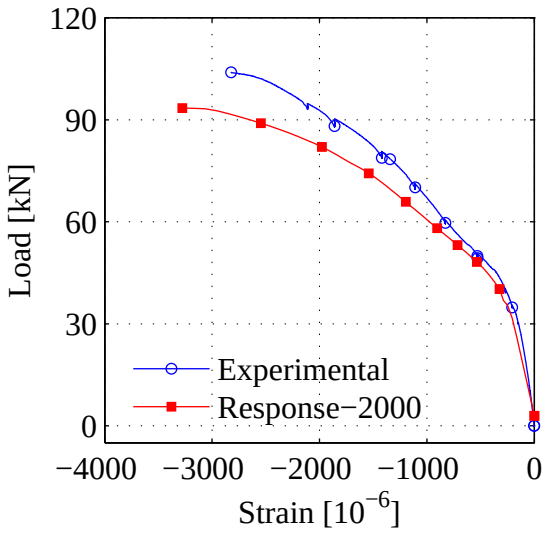

Figure 4-22 Concrete Strain Slab S-65-3 (Compression Failure)

The mean relative error at ultimate load for slab F-0-3, F-24-3, and F-35-3 is -26.8%, -22.2% and -30.5%, respectively. Whereas, the average mean post cracking relative error of strain at top face of concrete for slab F-0-3, F-24-3, and F-35-3 is -27.7%, -17.6% and -35.6%, respectively.

It is interesting to see the increase in the deviation of concrete strains with increase in corresponding loads. For all the four slabs, the theoretical results has showed higher strain in compressive zone of concrete. It may be difficult to determine the exact cause of this deviation. However it should be noted that the presented experimental strains in concrete were recorded with the help of ESG of 50.8 mm gauge length. One of the possible reason for this deviation may be due to the localized strain measurement on the slab and strains would be different along the width of sample (in constant moment region of slab).

4.3. Depth of Neutral Axis

The variation of depth of neutral axis with load is shown from Figure 4-23 to Figure 4-26. As expected, with the increase in the prestressing force the post cracking variation of neutral axis has shown more and more nonlinearity. The vertical shift between the theoretical and experimental values is due to the lowering of cracking moment because of shrinkage restraint stresses. For slabs F-24-3, and F-35-3 the reduction of 18.9% and 32.9%, respectively was measured.

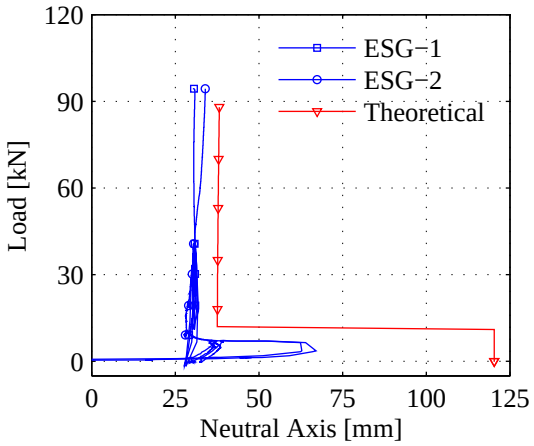

Figure 4-23 NA Slab F-0-3

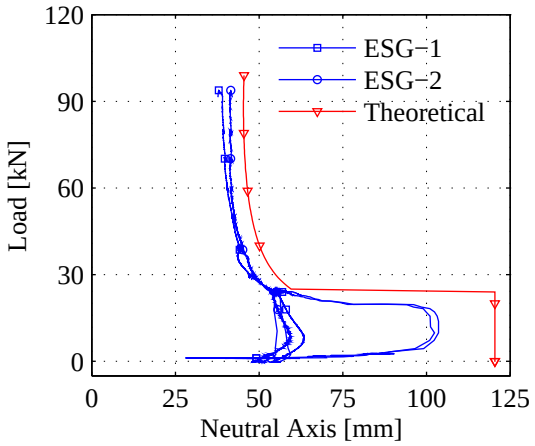

Figure 4-24 NA Slab F-24-3

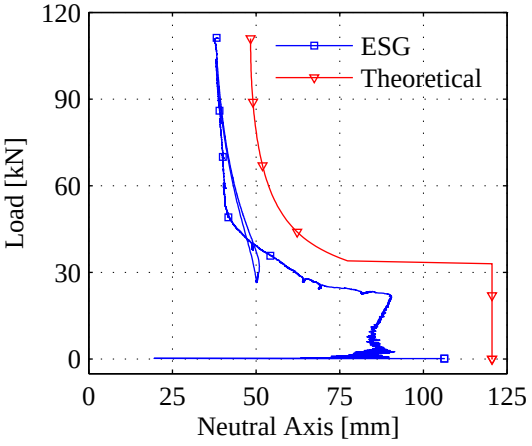

Figure 4-25 NA Slab F-35-3

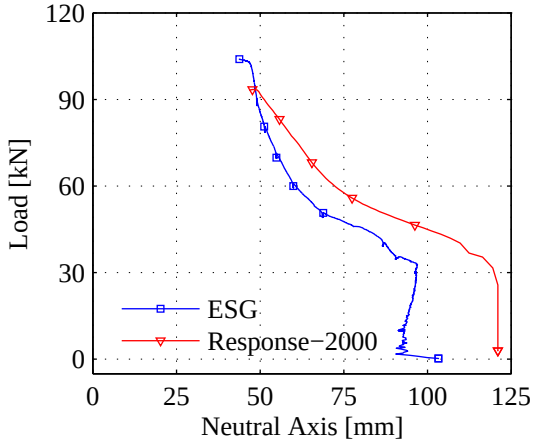

Figure 4-26 NA Slab S-65-3

4.4. Material Properties for Analysis of Short Term and Long Term Deformations

The experimental properties of concrete and reinforcement used in the analysis are described below.

4.4.1. Concrete

The concrete stress strain relation for analysis is derived in cubic form from the experimental data obtained through the ESG installed on concrete cylinder and tested as per ASTM Code C39/C39M (2012).

Slabs F-0-3 and S-65-3 were manufactured from the same batch of concrete. A cubic equation Eq 4-1has been derived empirically using Excel from the experimental data and has been plotted in Figure 4-27. Similarly, for Slab F-24-3 and F-35-3 Eq 4-2 is derived and plotted in Figure 4-28along with the experimental stress-strain curve.

$$\sigma_c = -3 \times 10^8 \varepsilon_c^3 - 23 \times 10^4 \varepsilon_c^2 + 36300 \times \varepsilon_c \qquad \text{Eq 4-1}$$

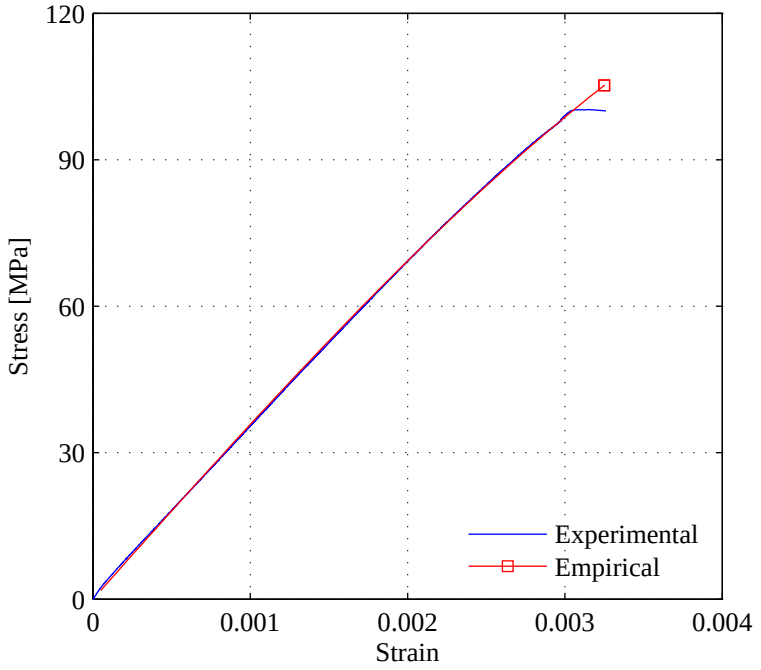

Figure 4-27 Concrete Stress-Strain for Slabs F-0-3 and S-65-3 (Eq 4-1)

$$\sigma_c = -7 \times 10^8 \varepsilon_c^3 - 2 \times 10^6 \varepsilon_c^2 + 36100 \times \varepsilon_c \qquad \text{Eq 4-2}$$

Where, σ_c is the concrete stress in MPa.

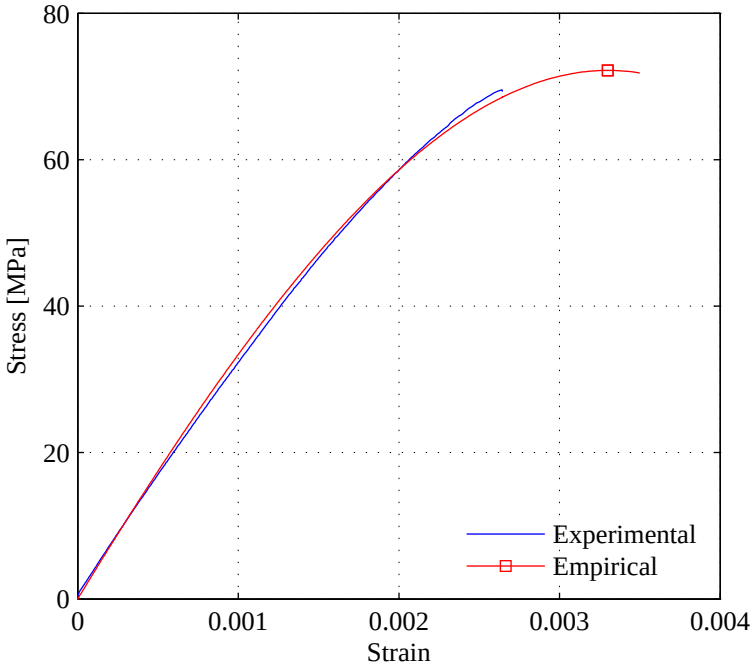

Figure 4-28 Concrete Stress-Strain for Slab F-24-3 and S-35-3 (Eq 4-2)

Concrete used to construct the 12 slabs was obtained from 9 concrete batches, it was found that the properties of concrete had very large variability as listed in Appendix-A. The concrete strength varied between 46 MPa to 75 MPa, the air content was from 5% to 15% and the unit weight had a range of 20.64 to 23.50 kN/m^3. One of the influencing parameters was the unit weight of concrete, which was experimentally determined from the concrete cylinders. Specifically, concrete from Batch-8 had an air content of 15%, which has resulted in much lower unit weight of concrete (20.64 kN/m^3) in comparison with the other batches. This had not only effected the short term analysis but also largely effected the long term behaviour of the slabs. Slabs F-24-2 and F-35-2 used concrete from Batch-8. As shown in Figure 4-41 and Figure 4-42, the cracking load and the

stiffness of the slabs decreased. In long term the higher air content has resulted in the higher compliance as shown in Figure B-10 (e), which resulted in large long term deformations.

One important factor which influences the prediction of deflection is the correct prediction of cracking moment which in turn depends on the modulus of rupture of concrete. Work done by Scanlon and Murray (1982), Gilbert (1999), Scanlon and Bischoff (2008) indicate the reduction of cracking moment due to shrinkage restraint stress. The reduction in cracking moment with time can further significantly increase the long term deflection due to the occurrence of cracks with time.

The modulus of rupture obtained from code equation, split cylinder test and from the cracking of test slabs (Eq 4-3 and Eq 4-4) are presented in Table 4-6. The values from split cylinder test and CSA S806-12 (2012) had an average increase of 30% and 36% respectively from the results obtained by cracking the slabs. In the analysis of the slabs, modulus of rupture obtained from CSA S806-12 (2012) approach has been used.

The modulus of rupture from the non-prestressed test slabs is obtained through back calculation from Eq 4-3. For prestressed concrete slabs the stresses generated through the prestressing force are added as shown in Eq 4-4

$$f_r = \frac{(M_{sw} + M_{Pcr})y_{bt}}{I_t} \qquad \text{Eq 4-3}$$

$$f_r = \frac{(M_{sw}+M_{Pcr})\, y_{bg}}{I_g} - \frac{P_c\, e\, y_{bg}}{I_g} - \frac{P_c}{A_g} \qquad \text{Eq 4-4}$$

Where, f_r is modulus of rupture of concrete, M_{sw} is the maximum bending moment due to self weight of member, M_{Pcr} is the bending moment at which the tensile stresses in concrete exceeds the modulus of rupture due to applied load, y_{bt} is the distance between bottom concrete face and centroid of transformed section, I_t is the transformed moment of inertia of uncracked section, y_{bg} is the distance between bottom concrete face and centroid of gross section, I_g is gross moment of inertia of the cross-section, P_c is the total prestressing force after time dependent losses in rebar/tendons, e is eccentricity of reinforcement of uncracked section, A_g is gross cross-sectional area of member.

To determine the modulus of rupture from Eq 4-3 and Eq 4-4, the cracking moment has been obtained from the test data by graphical method of linear regression from load deflection curve. In case of steel prestressed slabs the transition was not abrupt, thus the cracking moment is not included in the table. Also, non-prestressed GFRP slabs were cracked under their own weight due to shrinkage, thus it is as well not included.

Table 4-5 Cracking Moment - from Test Slabs

Slab ID	Concrete Batch	Age at Loading [Days]	Age at testing [Days]	Concrete strength [MPa]	Unit Weight [kN/m^3]	M_{sw} [kN-m]	P_{cr} [kN]	$M_{cr} = M_{sw} + M_{Pcr}$ [kN-m]
F-24-1	7	3	46	70.7	23.00	14.73	17.5	36.4
F-24-2	8	3	90	41.5	20.64	13.22	14.2	30.8
F-24-3	9	3	59	69.5	23.00	14.73	18.4	37.5
F-35-1	7	3	46	70.7	23.00	14.73	26.2	47.2
F-35-2	8	3	90	41.5	20.64	13.22	22.0	40.4
F-35-3	9	3	43	68.0	23.00	14.73	27.2	48.4

Table 4-6 Modulus of Rupture

Slab ID	Precracking Exp. value [MPa] ($f_{r,s}$)	Split cylinder [MPa] ($f_{r,c}$)	$f_{r,s}$ $f_{r,c}$ [MPa]	$\frac{f_{r,s} - f_{r,c}}{f_{r,c}} \times 100$ [%]	CSA approach [MPa] ($f_{r,CSA}$)	$f_{r,s}$- $f_{r,CSA}$ [MPa]	$\frac{f_{r,c} - f_{r,CSA}}{f_{r,c}} \times 100$ [%]
F-24-1	3.14	4.84	-1.70	**-35**	5.04	-1.90	**-38**
F-24-2	2.40	3.05	-0.65	**-21**	3.90	-1.50	**-38**
F-24-3	3.54	5.09	-1.55	**-30**	4.95	-1.41	**-28**
F-35-1	3.28	4.84	-1.56	**-32**	5.04	-1.76	**-35**
F-35-2	2.13	3.05	-0.92	**-30**	3.90	-1.77	**-45**
F-35-3	3.31	5.09	-1.78	**-35**	4.95	-1.64	**-33**

Table 4-6 shows that there is a reduction in the modulus of rupture of about 30% from the results obtained from split cylinder test. Similar estimate has been suggested by Scanlon and Bischoff (2008). They suggested a reduction of cracking moment by 2/3 of M_{cr} as specified in the ACI 318-05 for flexural members with reinforcement ratio less than approximately 0.8%.

Another important parameter in the analysis is the modulus of elasticity of concrete. Compressometer with dial gauge was employed to determine the same. The procedure adopted is discussed in more detail in Chapter 3. The data obtained is compared with the CSA A23.3-04 approach through Eq 4-5.

$$E_c = \left(3300\sqrt{f_c'} + 6900\right)\left(\frac{\gamma_c}{2300}\right)^{1.5} \qquad \text{Eq 4-5}$$

The percentage error with reference to the CSA A23.3 is within 10% of the experimental values, thus the prediction of modulus of elasticity is fairly accurate by the CSA A23.3 code. In general the prediction is on the higher side of the experimental values.

Table 4-7 Modulus of Elasticity of Concrete at Precracking/Testing

Concrete Batch	Slab ID	Compressometer Readings [MPa]	CSA A23.3	$\frac{\text{Compressometer} - \text{CSA}}{CSA} \times 100$ [%]
1	S-65-1	39609	39717	-0.3
2	F-0-1	40293	40850	-1.4
3	S-65-2	35976	37069	-2.9
4	F-0-2	36262	38396	-5.6
5	S-65-3	39165	41145	-4.8
6	F-0-3	37283	40726	-8.5
7	F-24-3, F-35-3	33003	34123	-3.3
8	F-24-2, F-35-2	25316	23942	5.7
9	F-24-1, F-35-1	34957	34645	0.9

4.4.2. Reinforcement

The slabs are reinforced with GFRP and low relaxation steel, the properties of reinforcement can be found in Table 3-5 and Table 3-6 respectively. The tension tests performed on GFRP show its expected linear behaviour up to failure. The modulus of elasticity of GFRP rebars is calculated as per CAN/CSA S806-12 from Eq A-1.

4.4.3. Loss in Prestress

The loss in prestress of the rebar/strand is the cumulative effect of creep, shrinkage and relaxation. Its prediction requires considerable computational effort; moreover the results change based on the prediction models used. Due to this variability the loss in strain over the desired period of time has been obtained from the ESG readings and this difference is used to estimate the loss of prestress for the short term analysis as listed in Table 4-8.

Table 4-8 Loss in Prestressing – Before Cracking

Slab ID	Age at Pre-cracking [Days]	Initial Strain [10^{-6}]	Change in Strain [10^{-6}]	Initial Prestressing Load [kN]	Prestress load after Losses	
					[kN]	[%]
F-24-1	46	3498	-296	244	223	8.5
F-24-2	90	3436	-531	239	202	15.5
F-24-3	59	3377	-337	238	214	10.0
F-35-1	46	3156	-363	354.5	329	7.1
F-35-2	90	5024	-732	355	303	14.6
F-35-3	43	5077	-451	357	325	8.9
S-65-1	261	-	-	481†	422†	12.0
S-65-2	246	6274	-775	492	431	12.4
S-65-3	219	5993	-725	470	413	12.1

† Average of S-65-2 and S-65-3

4.5. Long Term Behaviour

In this section an investigation of the time dependent behaviour of GFRP rebar prestressed/non-prestressed slabs and low relaxation steel strands prestressed slabs with age-adjusted effective modulus method has been compared. Three creep and shrinkage models namely ACI 209R-92 (1992), CEB MC90-99 (1999) and Bažant-Baweja B3 (1995) (ACI 209.2R-08) are used in the age adjusted effective modulus method.

Figure 4-30 depicts the deflection of some of the samples from the time prestress was released. In Figure 4-30, x-axis represents the time in days starting from September 25, 2012 which was the first day of casting and samples F-0-1, S-65-1 were cast. The positive deflection axis represents hogging and the negative deflection represents the sagging deflection profile of the slabs due to stressing and self weight.

Table 4-9 Residual Deflection due to Pre-cracking

Slab Name	Total Effective Prestressing Force at Transfer[kN]	Prestress Levels at Transfer[% of Ultimate]	Pre-cracking Load [kN]	Residual deflection [mm]
S-65-1	481	65.3	47.8	1.75
S-65-2	492	66.8	45.3	1.63
F-0-1	0	0	7.7	6.75
F-0-2	0	0	7.7	7.5
F-24-1	244	23.92	20.5	1.7
F-24-2	239	23.43	20.2	2
F-35-1	354.5	34.75	32.9	1.6
F-35-2	355	34.8	27.6	1.13

For slabs F-0-1, F-0-2 and S-65-2, the prestress was transferred at the age of one day and for the remaining slabs the age at transfer was three days due to insufficient strength after one day. Immediately after the transfer of prestress, the slabs were subjected to self-weight with a span of 6200 mm. The same support conditions were maintained during the entire period of observation and also during precracking the slabs, to avoid any creep reversal phenomenon. Since theoretically the precracking does not influence the long term behaviour for these slabs, thus the age of precracking was not required to be kept the same. The precracking began on day 257 as presented in Figure 4-30. A permanent residual deflection was recorded due to precracking of slabs on that day. The residual deflection was found to be dependent on the level of prestress and the amount of pre-cracking load as listed in Table 4-9. The highest residual deflection was 7.5 mm in GFRP reinforced slab (F-0-2). After precracking, on day 275 all the slabs were loaded with five

concrete blocks with weight of approximately 75.5 kg. This superimposed dead weight can be seen in Figure 4-30 as a second drop in deflection.

The slabs F-24-2 and F-35-2 had air content of 15%, due to which lower unit weight of concrete was recorded in the measurements. The lower unit weight has resulted in the reduction in the self weight of slab and consequently higher camber and creep-shrinkage deformation. The analysis results shows that the camber for F-35-2 was 4.45 mm against 2.92 mm and 3.07 mm for F-35-1 and F-35-3 respectively, slab F-24-2 resulted in a camber of 0.9 mm against 0.4 mm and 0.3 mm for slabs F-24-1 and F-24-3 respectively. Slabs with 24% of prestressing had shown most favourable deflection history by almost compensating the deflection due to dead weight by the upward moment generated from the prestressing force. The steel pre-tensioned slab S-65 had the highest total design prestressing force of 480 kN, due to which the highest camber and upward time dependent deflection is recorded. Slabs S-65-2, F-0-1 and F-0-2 were exposed to the winter of 2012-2013. During this period, the time dependent deformation of these slabs was almost restricted. In the first week of May 2013, these three slabs were brought inside the structural lab for precracking. As a result, the temperature of slabs was suddenly elevated from -0.5°C to +23°C. This sudden increase in temperature has increased the creep in concrete and consequently the rate of deflection of the slabs. The experimental study on increase in creep of concrete with the increase in temperature was performed by Fahmi et al. 1972 and Ohnuma et al. 1998 as shown in Figure 2-1 and Figure 4-29 respectively.The results presented in earlier research had close proximity with the deflection behaviour of the test slabs in this experimental program.

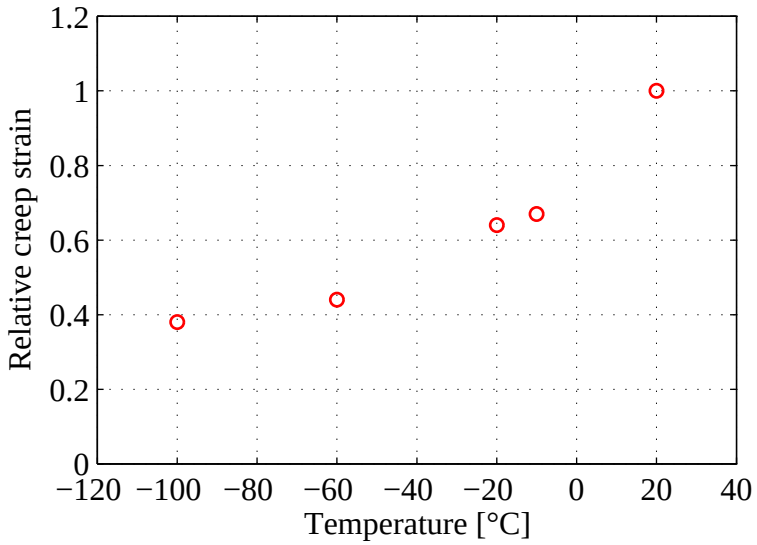

Figure 4-29 Relation between Relative Creep Strain and Temperature; Ohnuma et al. 1998

Out of all the slabs, only non-prestressed GFRP slabs did not satisfy the maximum permissible deflection from CSA S806-12 (2012). The code requires that deflection be limited to L/240 which is 25.84 mm. After an age of 401 days slab F-0-1 had undergone 30.9 mm of deflection and slab F-0-2 had shown 34.4 mm of deflection at the age of 387 days. Both of these exceeded the 25.8 mm deflection permitted by the code. The steel prestressed slab had an upward movement of 14 mm on 387th day. The GFRP prestressed slabs F-24-2, F-35-1 and F-35-2 had upward deflection of 0.03 mm, 2.4 mm and 7.7 mm at the age of 232nd, 187th and 232nd day respectively , slab F-24-1 had a downward deflection of 1.8 mm on 187th day after casting.

Figure 4-32 to Figure 4-39 compares the analysis results with the observed values. For the better comparison of long term deformation of all the slabs the immediate deflection is kept the same as theoretical in Figure 4-32 to Figure 4-39. It can be seen that the Bažant-Baweja B3 creep and shrinkage model has closely estimated the time dependent deformation of slabs except for slab F-35-2. The inaccuracy incorporated is due to the

high air content in concrete (15%). Unlike ACI 209R-92 (1992) model, the CEB MC90-99 (1999) and Bažant-Baweja B3 (1995) models do not include air content as a variable in their creep and shrinkage predictions. Also Bažant-Baweja B3 model provides compliance (Eq 2-24) as a parameter for creep deformation however in this analysis the creep coefficient is derived through compliance which can be another source of error as explained by Bažant (1995).

The test slabs were subjected to high variation in temperature. CEB MC90-99 model accounts for temperature by changing the age of concrete and had estimated good predictions for slabs F-0-3 and S-65-3. However in all other slabs it had under predicted the deformation.

The ACI 209R-92 model requires least computational effort, but considers the air content in concrete as a variable in the determination of creep coefficient, which in the present study is important due to the variation of air content between samples. The creep coefficient increases with the increase in air content. The method had closely predicted the deformation of slab F-35-2 having concrete air content of 15%.

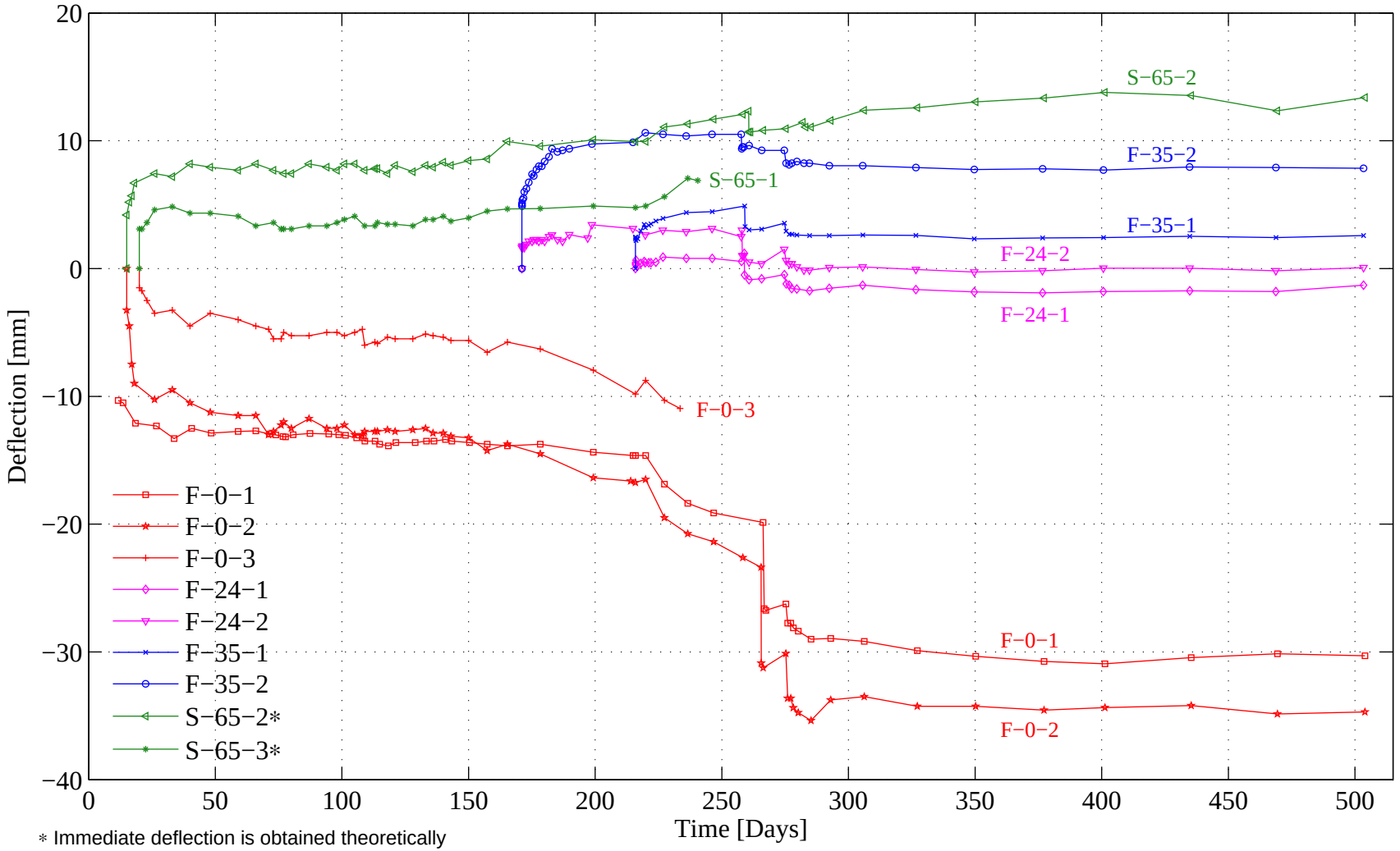

* Immediate deflection is obtained theoretically

Figure 4-30 Long Term Deflection

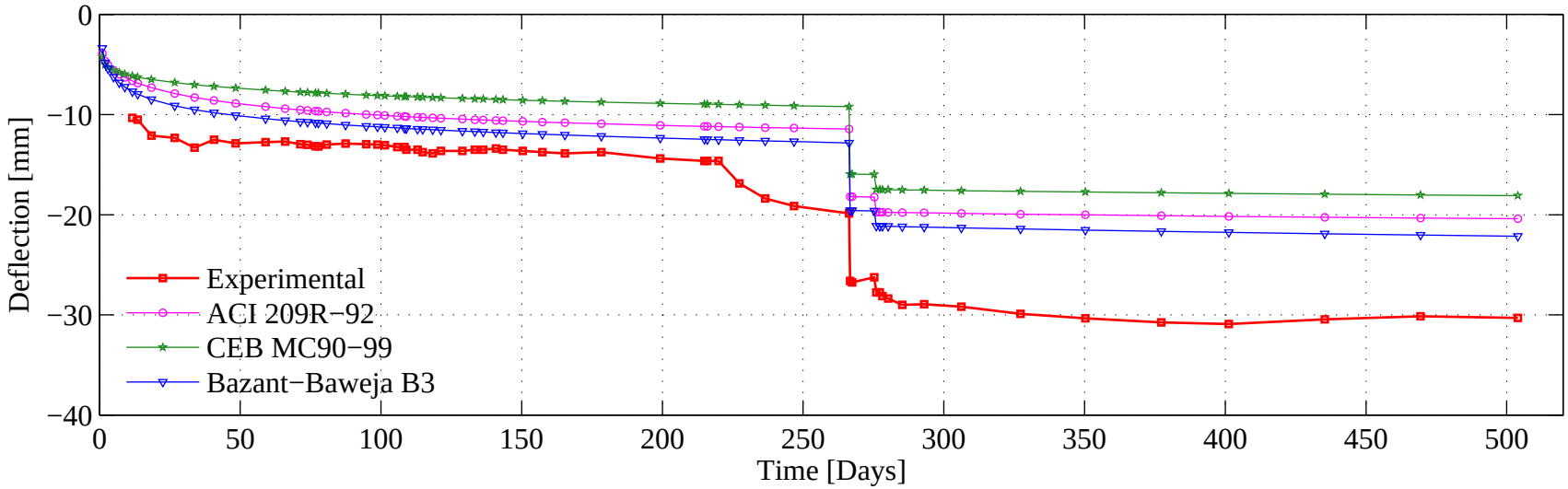

Figure 4-31 F-0-1 Long Term Deflection

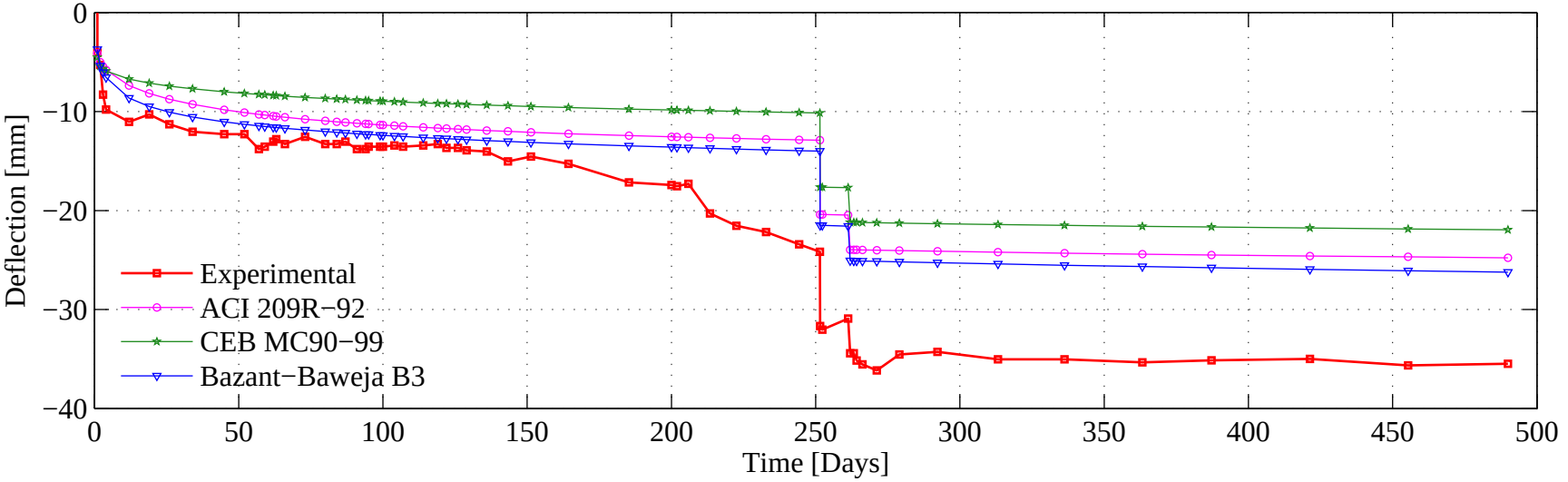

Figure 4-32 F-0-2 Long Term Deflection

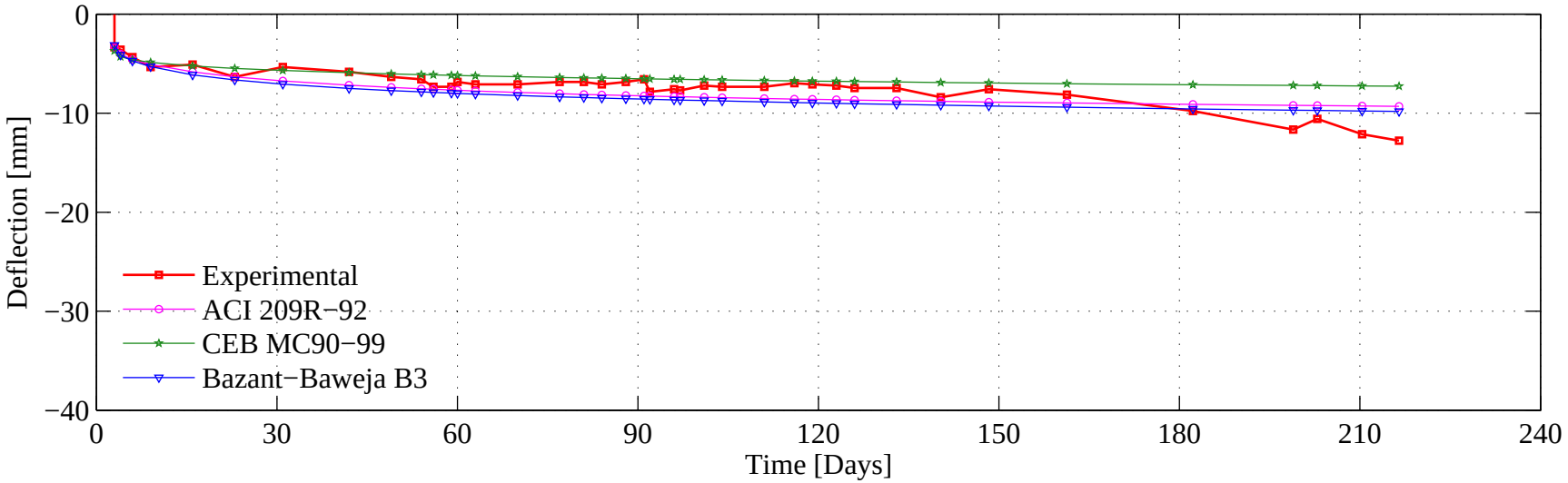

Figure 4-33 F-0-3 Long Term Deflection

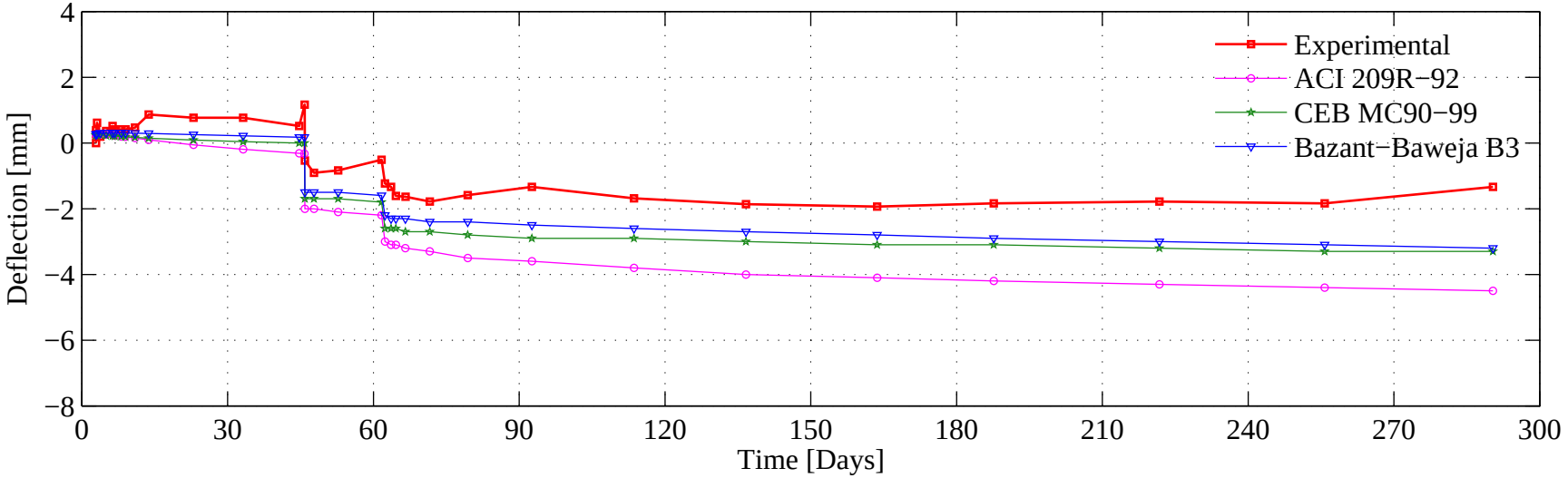

Figure 4-34 F-24-1 Long Term Deflection

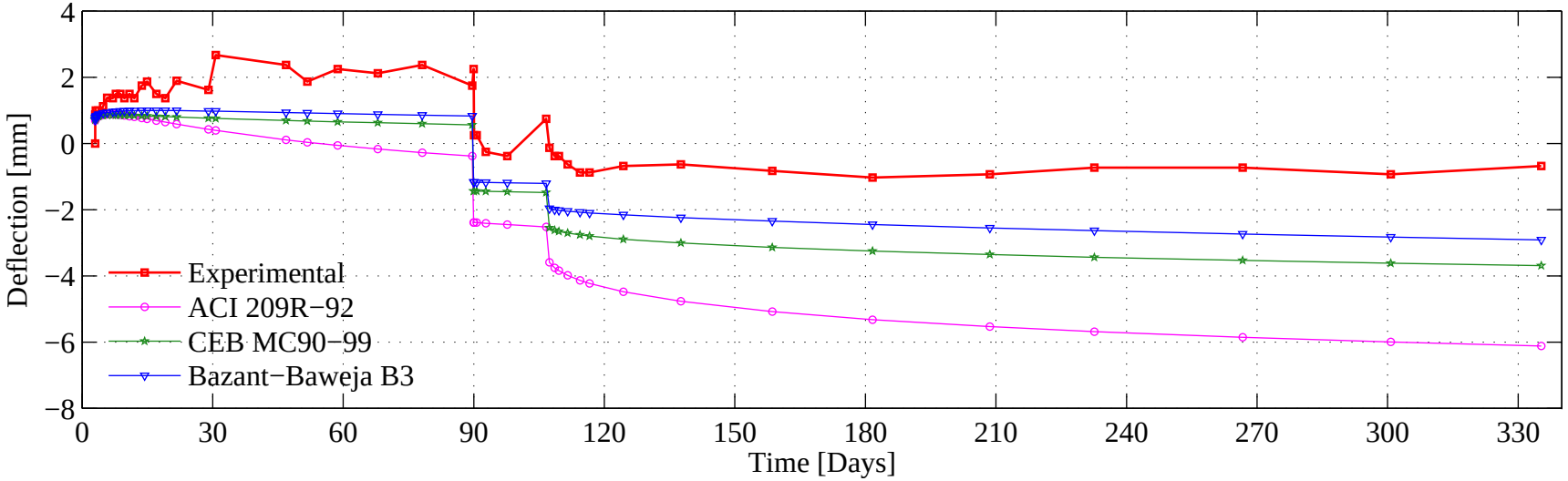

Figure 4-35 F-24-2 Long Term Deflection

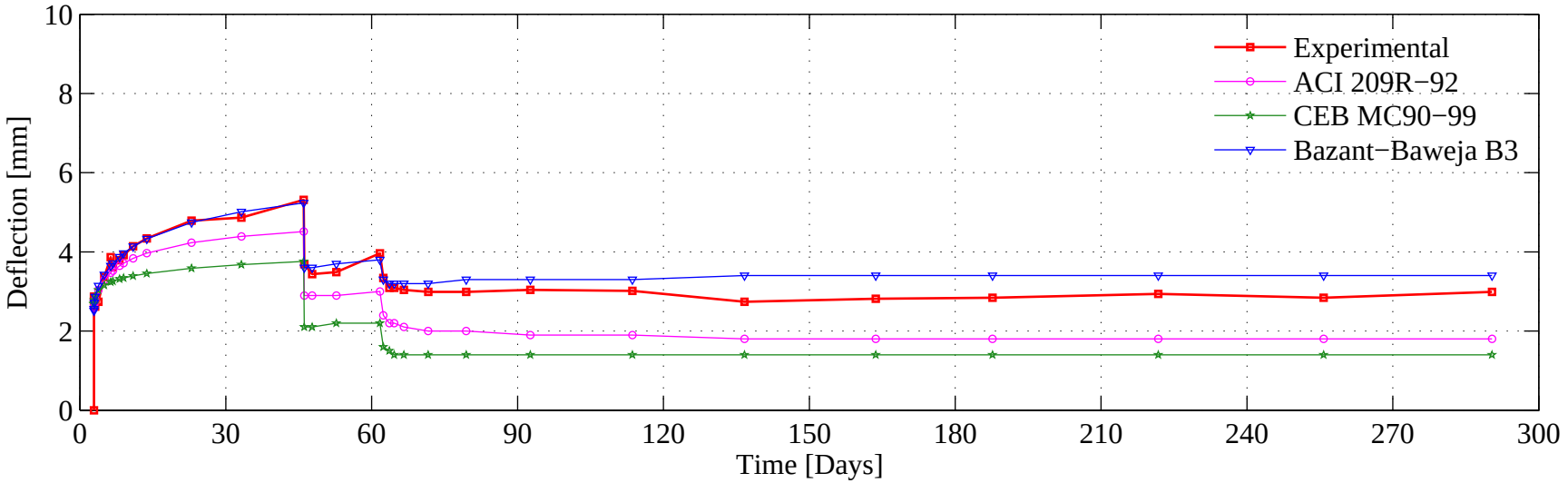

Figure 4-36 F-35-1 Long Term Deflection

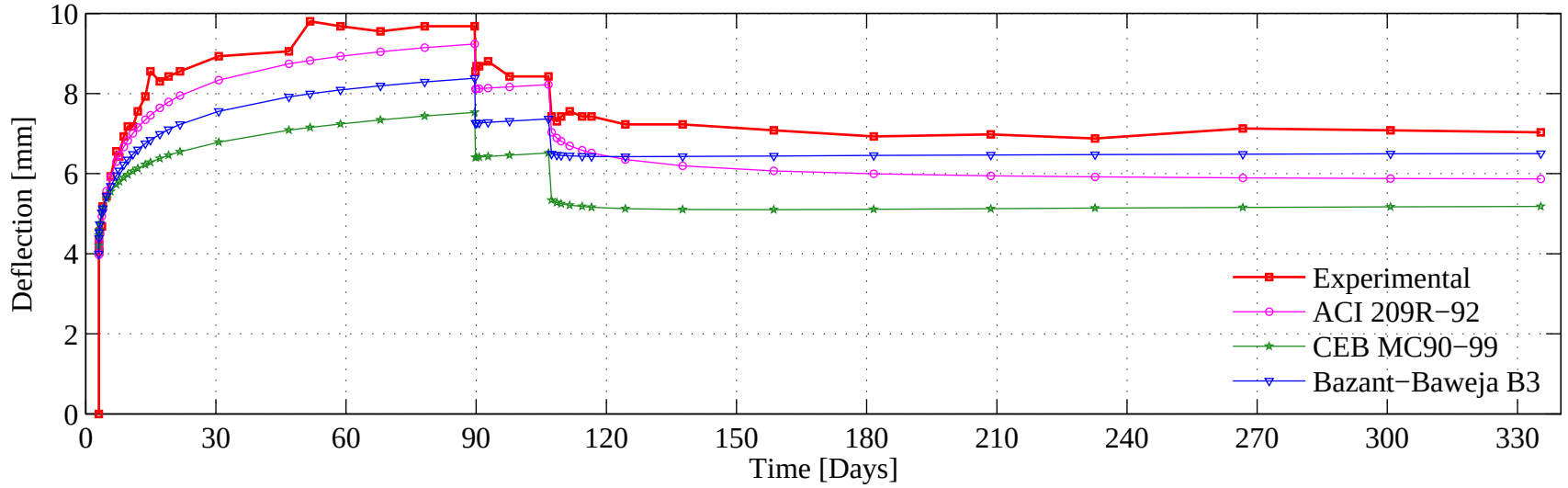

Figure 4-37 F-35-2 Long Term Deflection

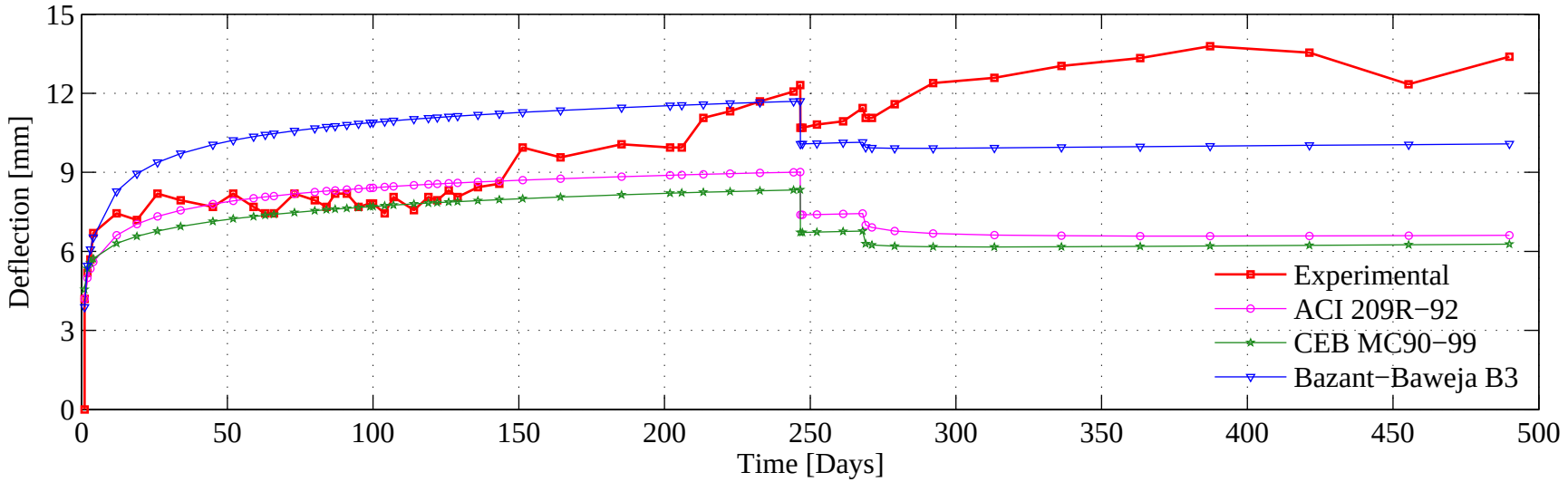

Figure 4-38 S-65-2 Long Term Deflection

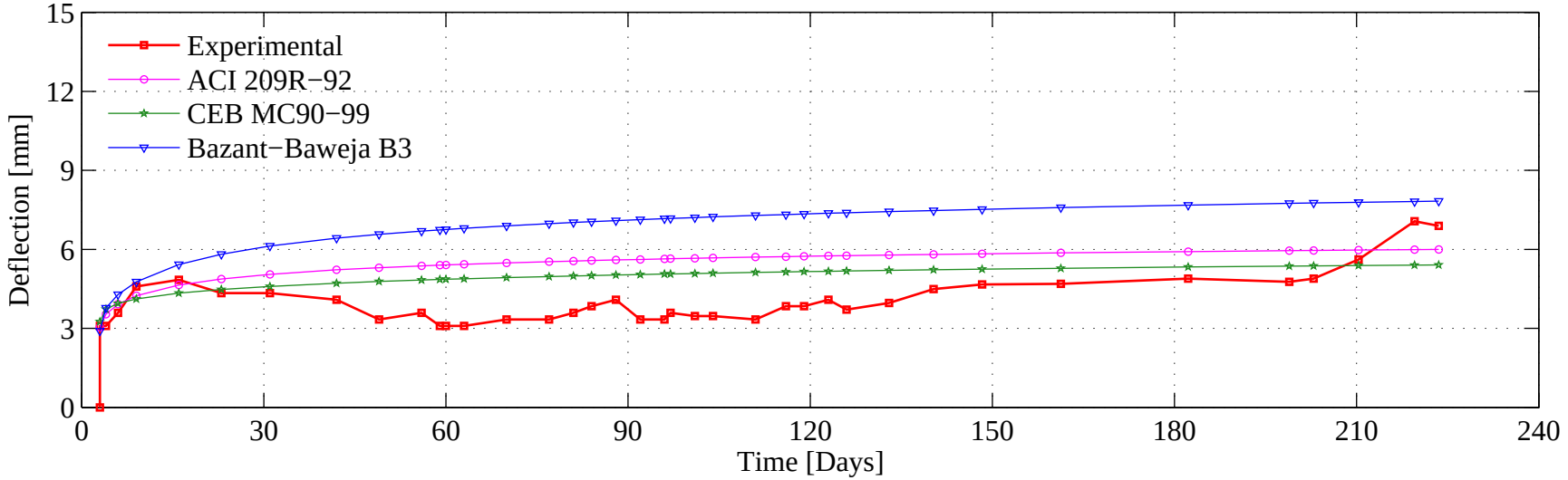

Figure 4-39 S-65-3 Long Term Deflection

The shrinkage and compliance for all the concrete batches are presented in Appendix-B. In this analysis only three models are compared however recently a new Model B4 (Wendner et al., 2013) has been developed, which is an recalibrated update of the previous Model B3. This model extends the scope to the concrete with admixtures and high strength and has been validated on bridge and laboratory data for multi-decade durations. For future work, such new prediction models and procedures can be tested on this existing data for their suitability for GFRP reinforced/prestressed members.

4.5.1. Precracking and Loading

Before applying the superimposed dead load mentioned in Table 3-4 the slabs were precracked. The precracking was done to examine the long term behaviour of cracked prestressed GFRP slabs and to bring the uncracked slabs to the similar conditions of cracked non-prestressed slabs. The details of loading is shown in Figure 4-40 to Figure 4-43. The difference in load deflection behaviour of F-24-1 and F-24-2 in Figure 4-41 and for F-35-1 and F-35-2 in Figure 4-43 is due to the difference in concrete strength.

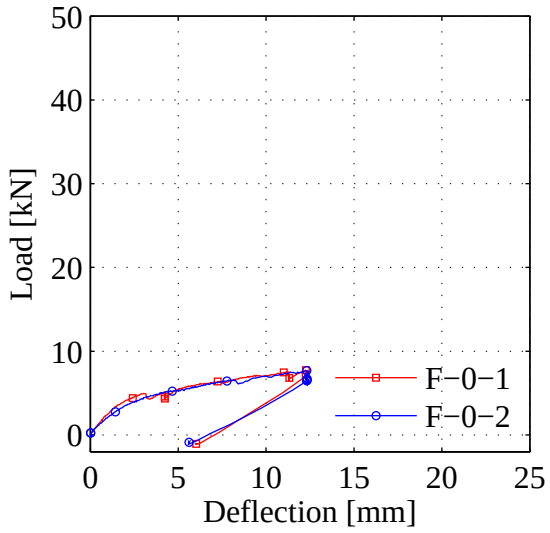

Figure 4-40 Cracking Slab F-0

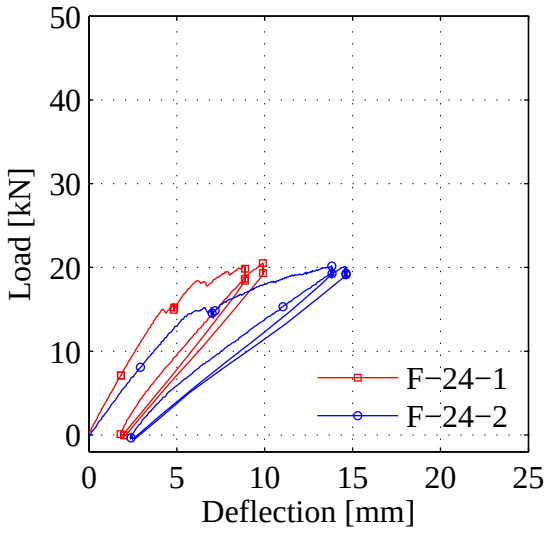

Figure 4-41 Cracking Slab F-24

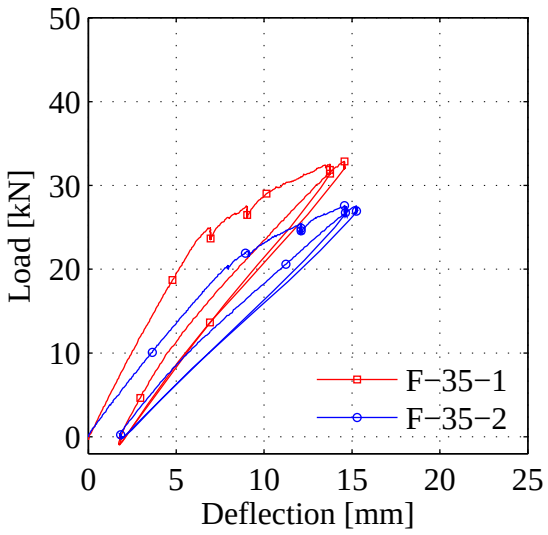

Figure 4-42 Cracking Slab F-35

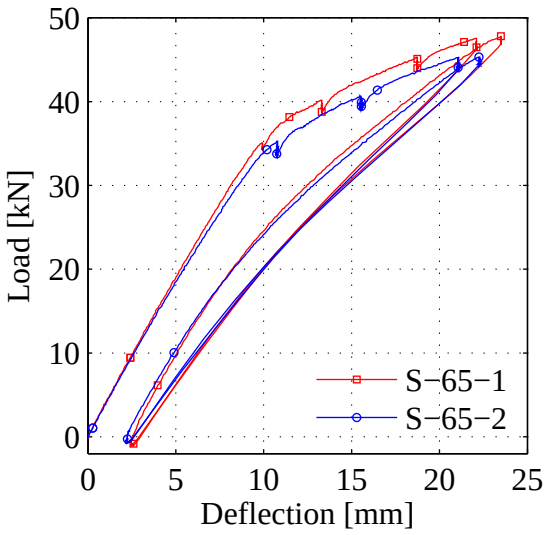

Figure 4-43 Cracking Slab S-65

4.5.2. Strain Observation

One of the aims of this project is to study the long term suitability of ESG in the structures exposed to environment. The following section shows the procedure adopted for the correcting error in strains due to thermal output of the gauges.

4.5.2.1. Dummy ESG

The strains were recorded for a temperature variation of -30°C to +50°C. To capture the strains in this temperature domain, the error due to thermal output of ESG becomes significant in comparison with the strains due to creep and relaxation. Thus the dummy gauges were installed in each slabs close to the supports and since the ESGs were installed at the mid-span of slab so to avoid the error due to differential temperature in the slab, the strain readings were captured in early morning hours when the temperature remains uniform in the entire slab. The theoretical estimation of thermal output from Eq 3-1 is validated through the strains obtained from dummy ESG installed in each slab and the results are presented from Figure 4-44 to Figure 4-46. It can be seen from the figures, that the estimation of thermal output is in good agreement with the dummy ESGs. The

modified manufacturers recommended thermal output is used to avoid the transfer of error in the dummy ESGs to all the strain readings.

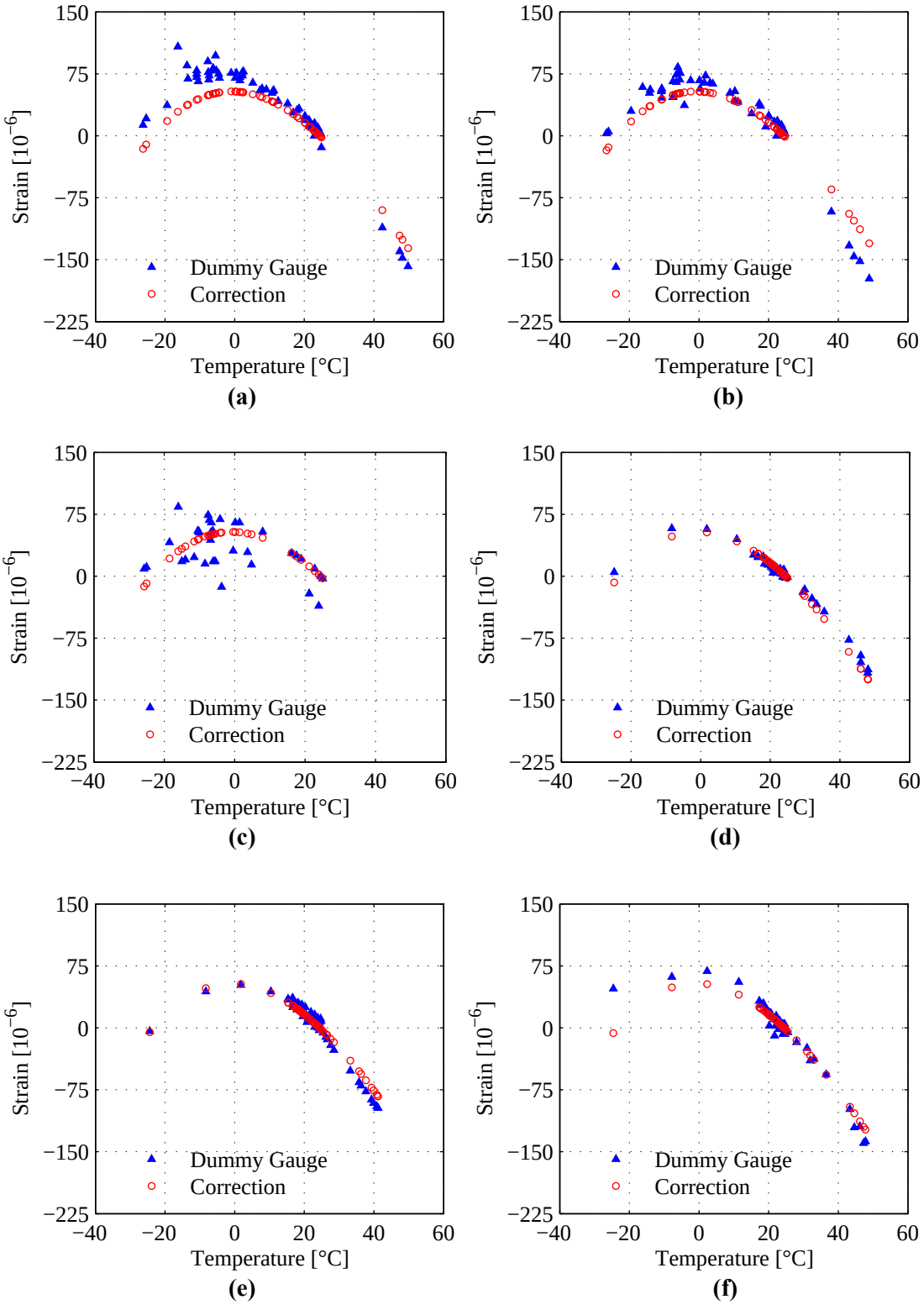

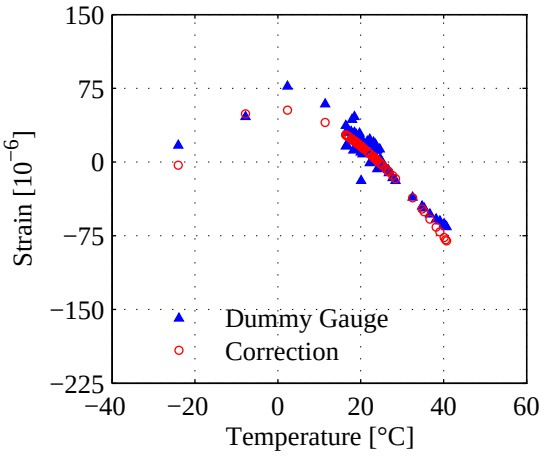

(g)

Figure 4-44 Dummy Gauge Strain 350 Ω (Micro-Measurements STC06) for (a) F-0-1, (b) F-0-2, (c) F-0-3, (d) F-24-1, (e) F-24-2, (f) F-35-1, (g) F-35-2

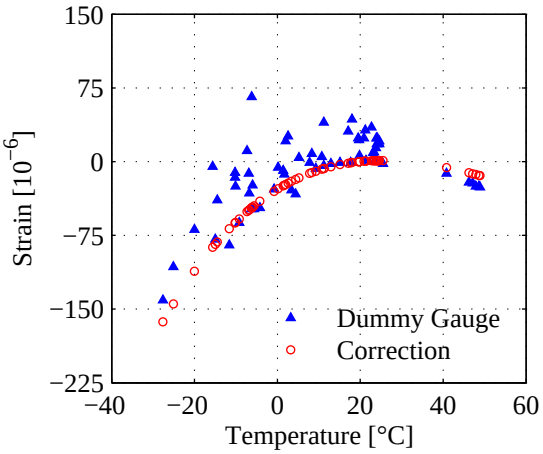

(a)

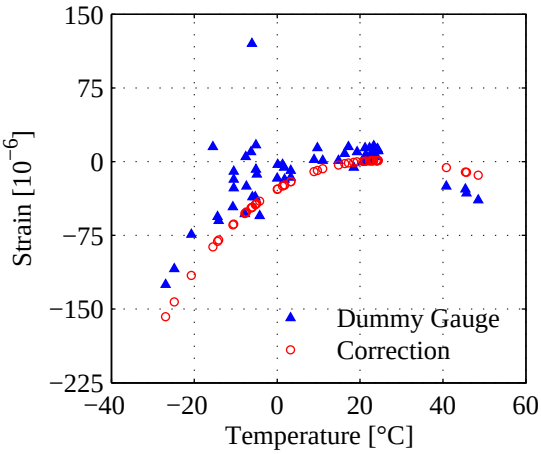

(b)

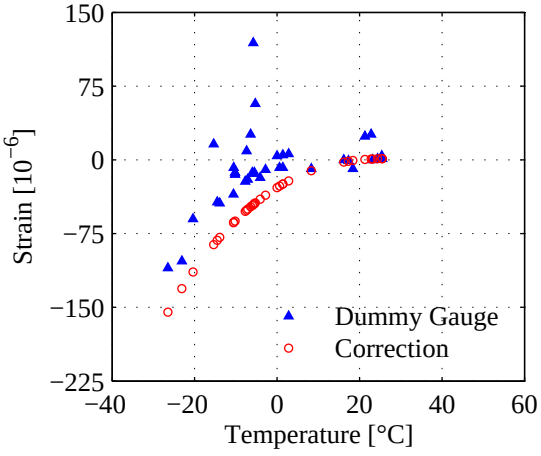

(c)

Figure 4-45 Dummy Gauge Strain 120 Ω for (a) S-65-1, (b) S-65-2, (c) S-65-3

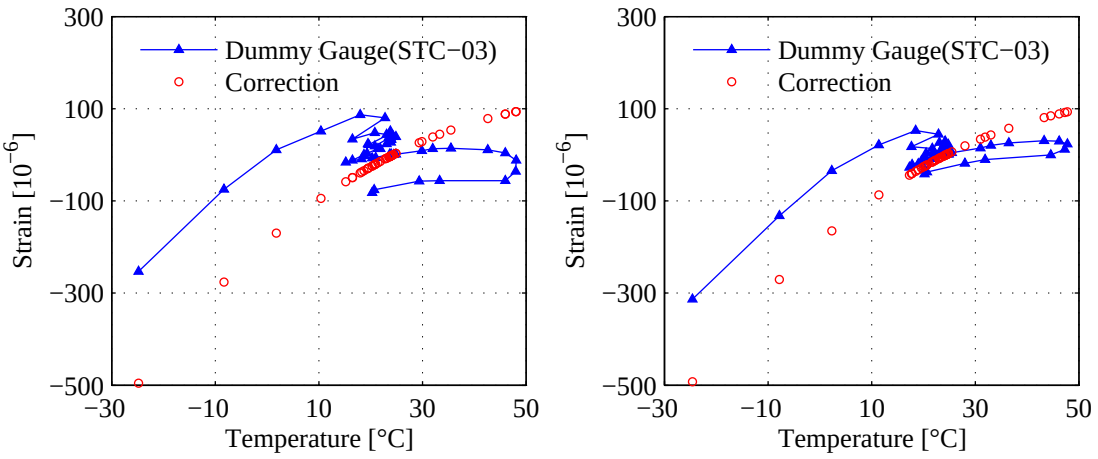

Figure 4-46 Dummy Gauge Strain 350 Ω (Micro-Measurements STC03) for (a) F-24-1, (b) F-24-2

The deviation of some of the data points in Figure 4-45 was due to the depletion of the battery of P-3500 strain indicator. Also, the dummy gauge readings in Figure 4-45 was for 120 Ω gauges which are less stable than the 350 Ω gauges. The initial readings of the dummy ESG's shown in Figure 4-46 does not match with the estimated thermal output due to the undergoing curing of bonding agent AE-10, however the later part on the left side of graph is showing similar slope as obtained from Eq 3-1. The dummy ESGs in Figure 4-44 and Figure 4-45 were installed nearly 6 months before the casting of slabs and were unaffected by the curing of bonding glue.

From the above figures it can be concluded that the modification made in the manufacturers recommended thermal output can be used to correct the error in strains due to thermal output with a reasonable degree of accuracy.

4.5.2.2. ESG on Longitudinal Reinforcement

Accurate knowledge of strains in rebar/tendons is essential to validate the theoretical analysis as well as it can accurately provide the loss in prestress. The observed strains corrected for thermal output from Eq 3-1 are presented from Figure 4-47 to Figure 4-55.

The comparison between FOS and ESGs for slab F-24-2 in Figure 4-48 shows a good match with an variation of 4.4%. However, for slabs F-0-1 and F-0-2 the difference at the time of last recorded reading was 30.9% and 17.8% respectively with respect to FOS strain reading. Considering the issues in the installation of FOS as discussed in section 3.7.2, the readings obtained from FOS cannot be claimed as true values. But, both ESG and FOS readings had shown similar pattern of change in strain.

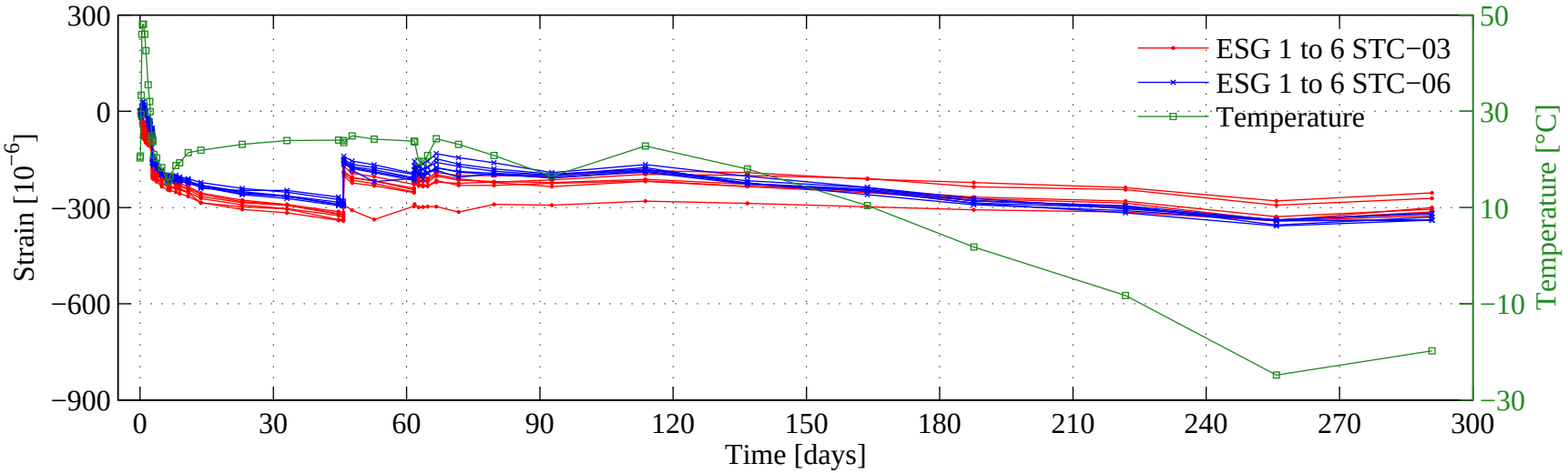

Figure 4-47 ESG Slab F-24-1

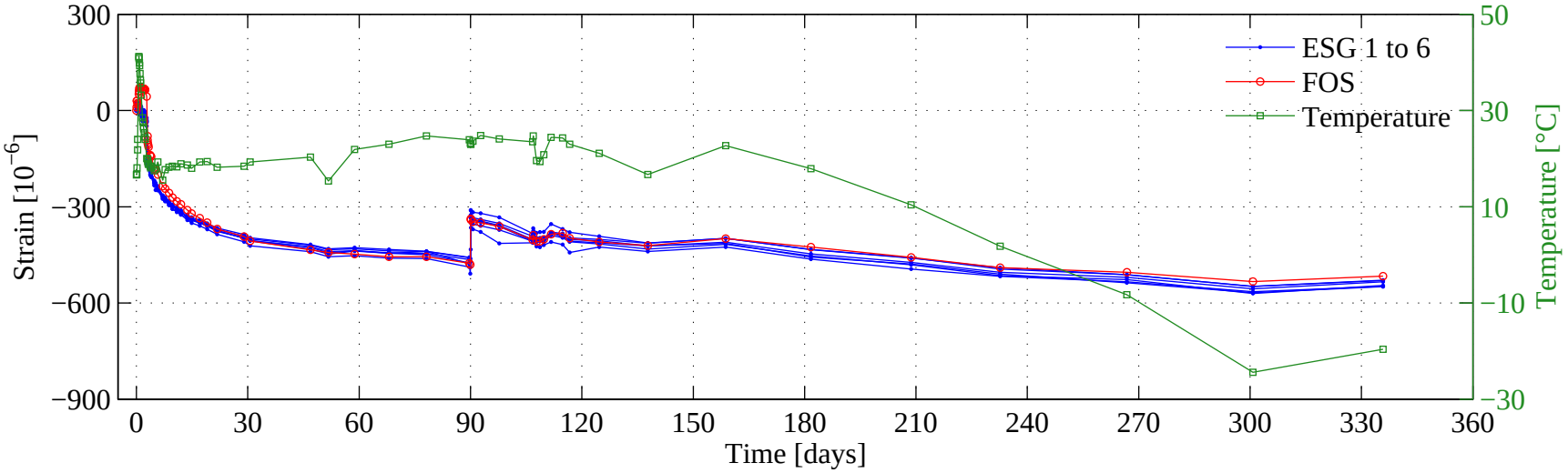

Figure 4-48 ESG Slab F-24-2

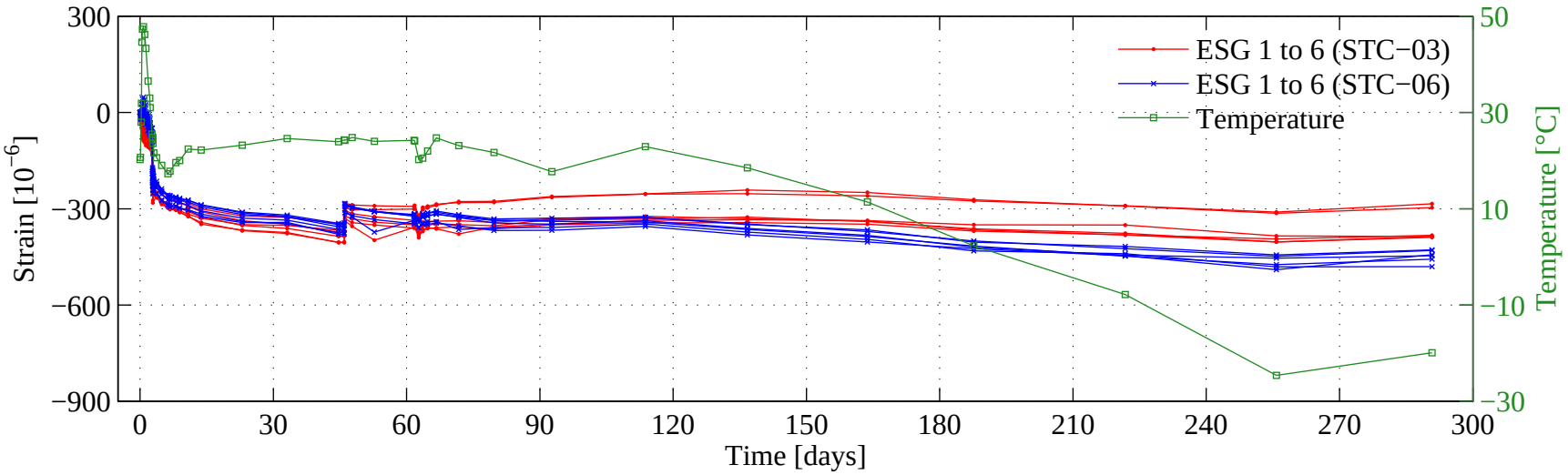

Figure 4-49 ESG Slab F-35-1

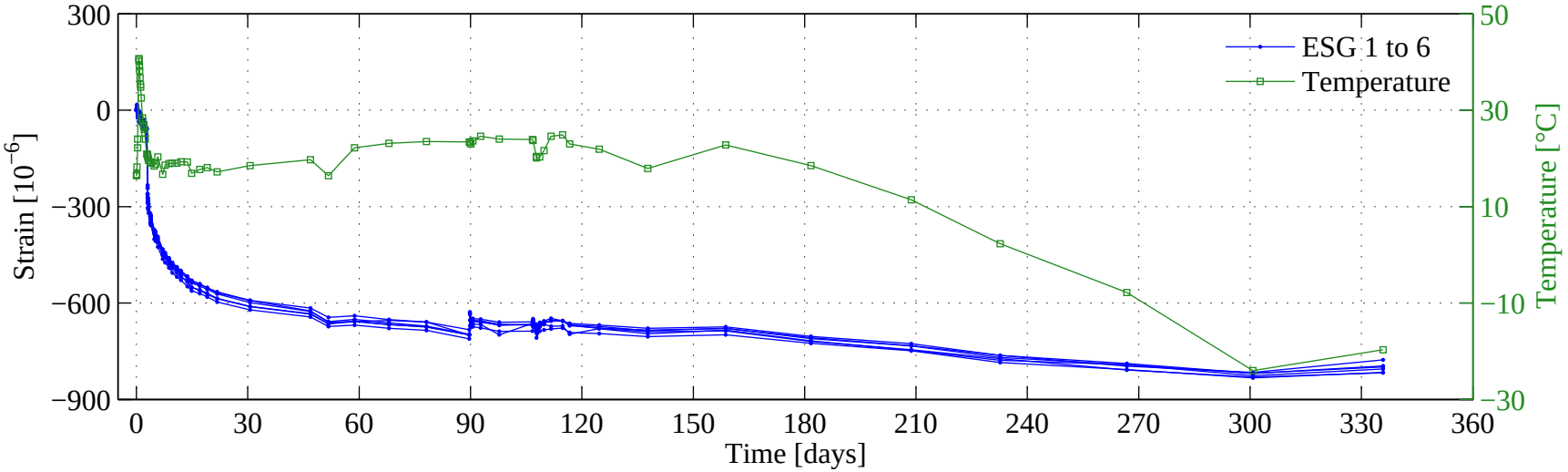

Figure 4-50 ESG Slab F-35-2

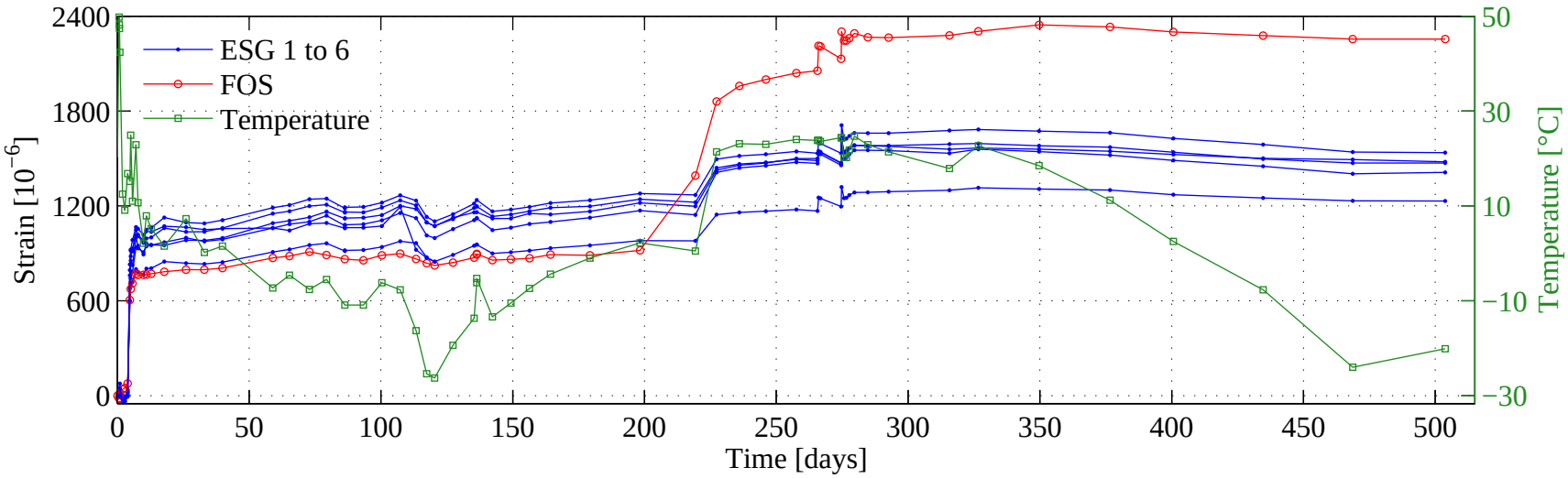

Figure 4-51 ESG Slab F-0-1

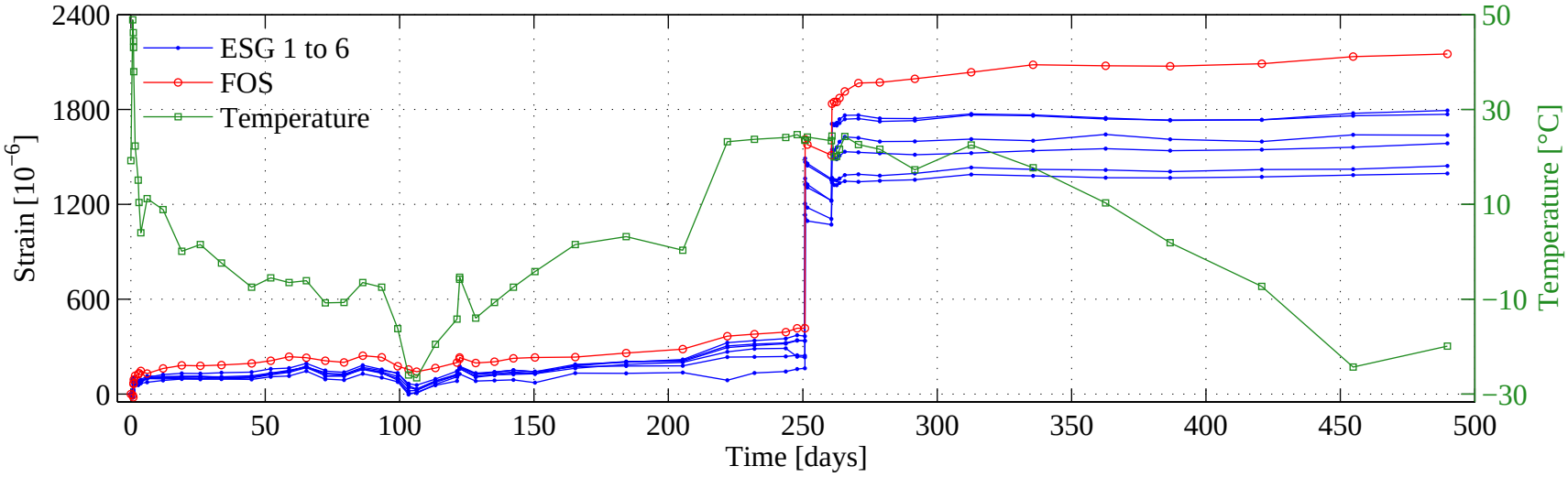

Figure 4-52 ESG Slab F-0-2

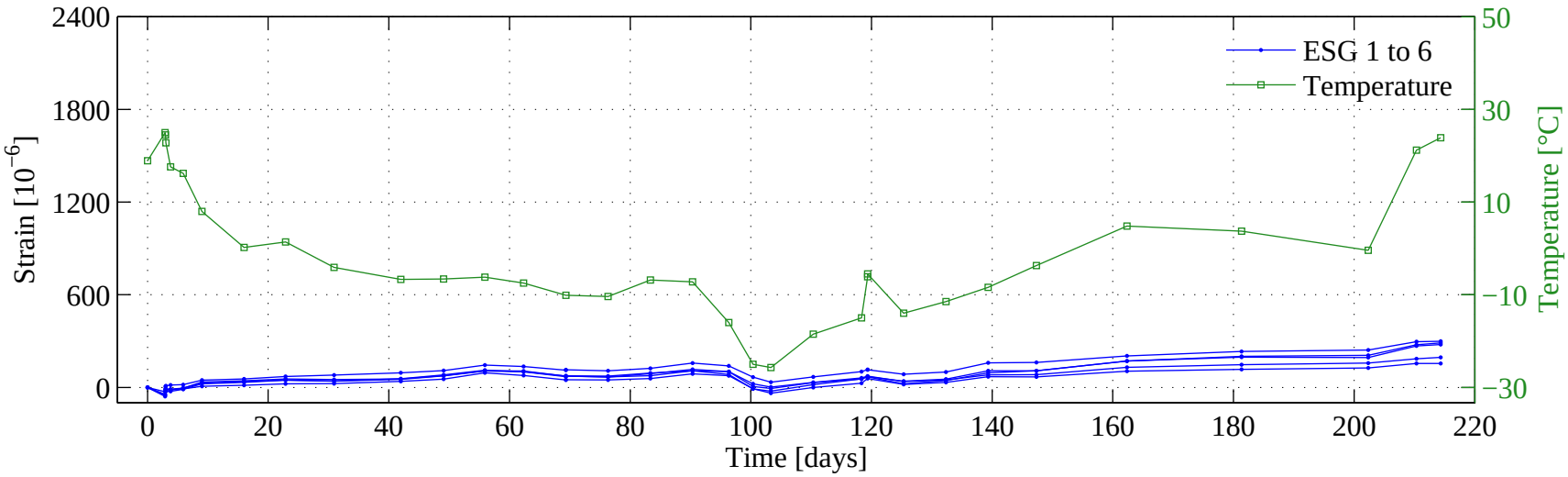

Figure 4-53 ESG Slab F-0-3

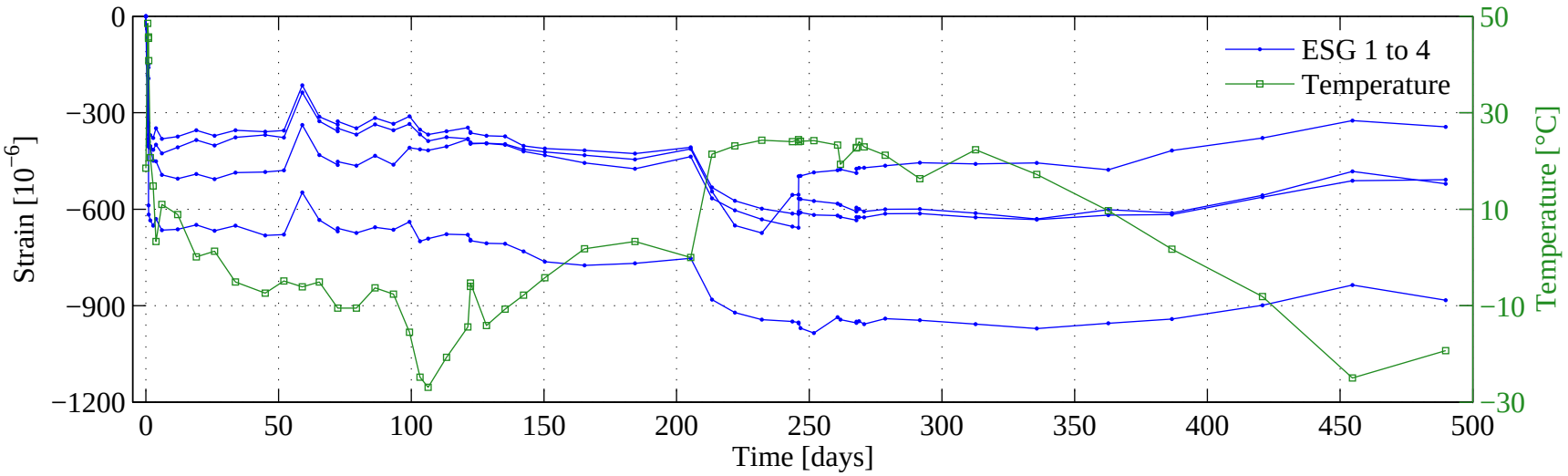

Figure 4-54 ESG Slab S-65-2

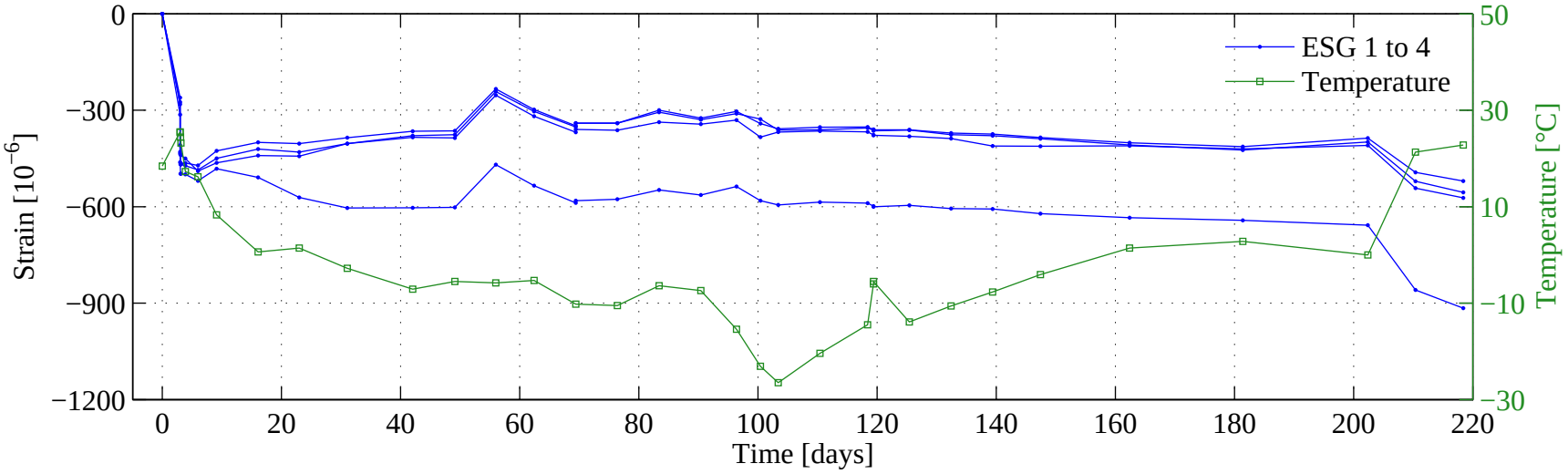

Figure 4-55 ESG Slab S-65-3

4.5.3. Cracking Behaviour

The pre-cracking load was targeted to get equal number of cracks in all prestressed slabs over the constant moment region under 4 point bending mechanism as shown in Figure 3-8, thus the load is different in all the prestressed slabs as listed in Table 4-5. On average 10 cracks were achieved by precracking in each prestressed slab. The cracking phenomenon is highly unpredictable and occurs at the weak sections due to the tensile forces on the tension face of member exceeding the tensile strength capacity of concrete. The cracks developed in the pre-cracking stage are presented in Table 4-10.

Table 4-10 Crack Development in Pre-Cracking Stage

Slab ID	Pre-cracking Load [kN]	Number of cracks	Average crack spacing [mm]
F-24-1	20.5	8	225
F-24-2	20.2	12	183
F-35-1	32.9	10	180
F-35-2	27.6	9	177
S-65-1	47.8	9	211
S-65-2	45.3	11	172

The slabs with non-prestressed GFRP slabs were cracked under their own weight and the cracks are listed in Table 4-11. A clear influence of early age loading is observed in non-prestressed slabs in terms of average crack spacing and number of cracks.

Table 4-11 Crack Development Under Self Weight for Slabs F-0

Slab ID	Age of Slabs [Days]	Age at Loading [Days]	Number of cracks	Average crack spacing [mm]
F-0-1	266	1	25	200
F-0-2	251	1	28	200
F-0-3	215	3	19	263

The crack details of the four slabs used in destructive testing are presented in Table 4-12 below.

Table 4-12 Crack Pattern Near Ultimate Capacity

Slab ID	Failure Load [kN]	Number of cracks	Average crack spacing [mm]
F-0-3	94.5	40	117
F-24-3	93.8	39	115
F-35-3	111.2	34	130
S-65-3	104	24	154

The graphical representation of crack pattern can be found in Appendix-B.

5. Conclusions

5.1. General

This study was conducted to investigate the long term and short term behaviour of GFRP prestressed concrete slabs. CAN/CSA S6 permits the use of GFRP as an internal prestressing element, thus it becomes necessary to investigate the long term behaviour of structural elements prestressed with GFRP rebars/tendons under natural environmental conditions. The time dependent observation included deflection of slabs, loss in prestress and strain history in the reinforcement. The second objective was to determine the suitability of ESGs for long term monitoring of strains in the reinforcement under outdoor environment.

Total of 12 slabs were constructed and 8 are being monitored for a period of 10 years. The time dependent deflection obtained from the experiments was compared with theoretical deflections using Age-Adjusted Effective Modulus Method (Bazant 1972). In AAEMM three different creep and shrinkage models were used namely ACI 209R-92 (1992), CEB MC90-99 (1999) and Bažant-Baweja B3 (1995). The short term behaviour was obtained by conducting destructive testing on four slabs (one each from 4 types). The short term tests included the estimation of load-deflection by CSA S806-12 (2012), ISIS Design Manual No. 3 (2007), ACI 440.1R-06 (2006), ACI 440.4R-04 (2004) and modified Bischoff method (Bischoff et al., 2011).

5.2. Short Term Load Deflection Response

[1] The effect of shrinkage restraint stresses and early age loading is observed in reducing the cracking moment of the slabs. The modulus of rupture obtained from split

cylinder test and CSA S806-12 (2012) are 30% and 36% respectively higher than from the results obtained by cracking the slabs prestressed with GFRP rebars with 0.88% reinforcement ratio.

[2] All four methods predicted the load-deflection response of GFRP reinforced slabs fairly well especially at higher load levels. However at lower loads differences were found between each of them. The ISIS Canada and CSA S806-12 (2012) has shown sudden loss in post-cracking stiffness compared to the other two methods. The error in the deflection at failure for CSA S806-12 (2012), ISIS Design Manual No. 3 (2007), ACI 440, and modified Bischoff method for slab F-0-3 is -8.2%, -6.3%, -4.3% and -3.2% respectively. For slab F-24-3 the error is 2.3%, 4.6%, 9.9% and 7.1% respectively. For slab F-35-3 the error is 2.5%, 5.3%, 8.9% and 6.6% respectively.

[3] Historically the load deflection response of prestressed members has been predicted by introducing the decompression moment in the effective moment of inertia approach. Adopting the same approach, the prediction of failure load and deflection at failure for GFRP prestressed members can be estimated within 10% of the experimental results.

[4] The strain compatibility approach has produced satisfactory results in predicting moment-curvature and strain in reinforcement for the cross-sectional analysis of non-uniformly shaped of concrete. For both prestressed and non-prestressed slabs, the results are well within 10% of the experimental results.

5.3. Time Dependent Behaviour

[1] During the period of approximately 10 months of observation on slabs with similar properties of concrete, the loss in GFRP prestress strain is less than the loss observed in steel strands. On the basis of strain gauge readings, slabs F-24-1, F-24-2, F-24-3, F-35-1, F-35-2, F-35-3, S-65-2, S-65-2 and S-65-3 had lost 8.3%, 15.5%, 10.0%, 7.1%, 14.6%, 8.9%, 12.4% and 12.1% of prestressing strain respectively.

[2] It was found that the calculated deflections were largely dependent on the creep and shrinkage models. Considering the limitations of the creep and shrinkage models, the deflections were predicted with sufficient degree of accuracy and have shown the same pattern as experimentally observed deflections over a period of 10 months of observation.

[3] The GFRP pre-tensioned and steel prestressed concrete slabs have satisfied the CSA S806-12 (2012) and CSA A23.3-04 (2004) maximum permissible deflection limit of 25.8 mm. However, GFRP reinforced slabs F-0-1 and F-0-2 had undergone 30.9 mm and 34.4 mm mid-span deflection respectively and hence exceeded the permissible deflection by 19.8% and 33.3%, respectively. The steel prestressed slab had an upward movement of 14 mm. The GFRP prestressed slabs F-24-2, F-35-1 and F-35-2 had upward deflection of 0.03 mm, 2.4 mm and 7.7 mm respectively, and slab F-24-1 had a downward deflection of 1.8 mm.

[4] The creep and shrinkage strains predicted by ACI 209R-92 (1992), CEB MC90-99 (1999) and Bažant-Baweja B3 (1995) had shown large variability in their results and had become the major influencing factor in the accuracy of predicting the long term deformation. This variation signifies the importance of experimental determination of creep and shrinkage for each batch of concrete.

[5] The influence of early age loading was observed in terms of higher immediate and time dependent deflections. In addition, smaller average crack spacing and increased number of cracks was also observed in the slabs loaded on day one versus the slabs loaded on day three.

[6] Slabs with higher strength concrete had smaller time dependent deflections.

[7] Using multipliers for the prediction of long term deflection is not suitable for GFRP prestressed members.

[8] The higher air content in concrete had resulted in higher time dependent deflection. The air content had not only influenced creep and shrinkage but also reduced the unit weight of concrete.

[9] In general Bažant-Baweja B3 model in combination with AAEMM has estimated the long term deflections closest to the experimental results. However with the increase in the air content of concrete it under predicts the deformation.

[10] The deformation due to creep was mostly restricted in sub-zero temperatures. As soon as the test slabs were brought to room temperature, the deformation of slabs increased due to the increase in creep.

[11] ESGs were able to capture the time dependent strains in the rebars/strands. The strains obtained from the ESG are in line with the deflection observation and had shown similar strain pattern as recorded by FOS after applying correction for thermal output of strain gauge with STC mismatch. It was found that the installation of ESG was less susceptible to damage than the installation of FOS. However, depending on the DAQ

used, the readings with ESGs get prone to sensitivity due to temperature, magnetic interference, humidity levels making them vulnerable to use in outside environment.

[12] In general, 350 Ω gauges had produced more stable strains than 120 Ω gauges.

5.4. Recommendations for Future Work

[1] At the end of long-term monitoring of slabs, a material degradation study for GFRP shall be performed on prestressed/non-prestressed slabs to check their suitability under natural environmental conditions.

[2] CAN/CSA S6 allows GFRP to be used as a prestressing material; however the relaxation data for the same is not provided by the code. Thus research shall be conducted for the accurate prediction of relaxation of GFRP rebars at the stress of 25% of ultimate strength

[3] In the implementation of age adjusted effective modulus method, a constant value of aging coefficient is considered. The increase in accuracy by considering a variable aging coefficient shall be checked.

[4] There are new developments made in the existing creep and shrinkage models which can be analysed for their suitability for these slabs.

[5] GFRP anchorage system adopted in this experiment was expensive and time consuming. This requires a new less expensive method to be developed with equal reliability.

[6] For greater accuracy, humidity meters for measuring the humidity shall be installed in the future tests which involve the creep and shrinkage behaviour of concrete.

References

ASTM C39/C39M − 12a. (2012), "Standard Test Method for Compressive Strength of Cylindrical Concrete Specimens" ASTM International, 100 Barr Harbor Drive, PO Box C700, West Conshohocken, PA 19428-2959. United States

ASTM C143/C143M − 12. (2012), "Standard Test Method for Slump of Hydraulic-Cement Concrete" ASTM International, 100 Barr Harbor Drive, PO Box C700, West Conshohocken, PA 19428-2959. United States

ASTM C231/C231M − 10. (2010), "Standard Test Method for Air Content of Freshly Mixed Concrete by the Pressure Method" ASTM International, 100 Barr Harbor Drive, PO Box C700, West Conshohocken, PA 19428-2959. United States

ASTM C469/C469M − 10. (2010), "Standard Test Method for Static Modulus of Elasticity and Poisson's Ratio of Concrete in Compression" ASTM International, 100 Barr Harbor Drive, PO Box C700, West Conshohocken, PA 19428-2959. United States

ASTM C496/C496M-11. (2011), "Standard Test Method for Splitting Tensile Strength of Cylindrical Concrete Specimens" ASTM International, 100 Barr Harbor Drive, PO Box C700, West Conshohocken, PA 19428-2959. United States

ASTM C617/C617M − 12. (2012), "Standard Practice for Capping Cylindrical Concrete Specimens" ASTM International, 100 Barr Harbor Drive, PO Box C700, West Conshohocken, PA 19428-2959. United States

ASTM C1064/C1064M − 12. (2012), "Standard Test Method for Temperature of Freshly Mixed Hydraulic-Cement Concrete" ASTM International, 100 Barr Harbor Drive, PO Box C700, West Conshohocken, PA 19428-2959. United States

American Concrete Institute (ACI). (1996). "ACI Committee 440 report: State-of-the-Art Report on Fiber Reinforced Plastic (FRP) Reinforcement for Concrete Structures" ACI 440R-96, American Concrete Institute, Farmington Hills, Michigan, USA.

American Concrete Institute (ACI). (2004). "ACI Committee 440 report: Prestressing Concrete Structures with FRP Tendons" ACI 440.4R-04, American Concrete Institute, Farmington Hills, Michigan, USA.

American Concrete Institute (ACI). (2006). "ACI Committee 440 report: Guide for the Design and Construction of Structural Concrete Reinforced with FRP Bars" ACI 440.1R-06, American Concrete Institute, Farmington Hills, Michigan, USA.

American Concrete Institute (ACI). (2008). "ACI Committee 209: Guide for Modeling and Calculating Shrinkage and Creep in Hardened Concrete" ACI 209.2R-08, American Concrete Institute, Farmington Hills, Michigan, USA.

American Concrete Institute (ACI). (2011). "ACI Committee 318: Building Code Requirements for Structural Concrete" ACI 318M-11, American Concrete Institute, Farmington Hills, Michigan, USA.

Al-Omaishi, N., Tadros, M.K., Seguirant, S.J., "Estimating prestress loss in pretensioned, high-strength concrete members", PCI Journal, Vol. 54, No. 04, Fall 2009, pp. 132-159.

Bazant, Z.P., "Prediction of Concrete Creep Effects Using Age-Adjusted Effective Modulus Method", Journal of the American Concrete Institute, Vol. 69, No. 04, April 1972, pp. 212-219.

Bazant, Z.P., "Creep and shrinkage prediction model for analysis and design of concrete structures - model B3*", Materials and Structures, Vol. 28, 1995, pp. 357-365.

Bischoff, P.H., Gross, S.P., "Equivalent Moment of Inertia Based on Integration of Curvature", Journal of Composites for Construction, Vol. 15, No. 03, June 2011, pp. 263-273.

Branson, D. E., "Instantaneous and time-dependent deflections of simple and continuous reinforced concrete beams." HPR Report No. 7, Part 1, Alabama Highway Department, Bureau of Public Roads, Montgomery, AL, 1965, pp 78.

Brown, V.L., 1997, "Sustained Load Deflections in GFRP Reinforced Concrete Beams" Proceedings of the Third International Symposium on Non-Metallic (FRP) Reinforcement for Concrete Structures (FRPRCS-3), Vol. 2, Japan Concrete Institute, Tokyo, Japan, pp. 495-502.

Canadian Standards Association (CSA). (2004). "Design of concrete structures" A23.3-04, Canadian Standards Association, Toronto, Ontario, Canada.

Canadian Standards Association (CSA). (2010). "Canadian Highway Bridge Design Code" S6-10, Canadian Standards Association, Mississauga, Ontario, Canada.

Canadian Standards Association (CSA). (2012). "Design and Construction of Building Components with Fiber-Reinforced Polymers" S806-12, Canadian Standards Association, Mississauga, Ontario, Canada.

CEB-FIP. (1990). "Model code for concrete structures". Comité Euro-International du Béton - Fédération International de la Précontrainte, Thomas Telford House, London, England.

Collins, M.P. and Mitchell, D. (1997) *Prestressed Concrete Structures*, Response Publications, ON, Canada, 766 pp.

Fahmi, H., Polivka, M., Bresler, B. "Effect of Sustained and Cyclic Elevated Temperature on Creep of Concrete", Cement and Concrete Research, Vol. 2, No. 5, 1972, pp. 591-606.

Gilbert, R. I., "Deflection Calculation for Reinforced Concrete Structures - Why We Sometimes Get It Wrong", ACI Structural Journal, Vol. 96, No. 06, November-December 1999, pp. 1027-1032.

Gross, S.P., Yost, J.R., Kevgas, G.J., "Time-Dependent Behavior of Normal and High Strength Concrete Beams Reinforced with GFRP Bars under Sustained Loads", ASCE Proceedings: High Performance Materials in Bridges, September 2003, pp. 451-462.

ISIS Canada (2007). *Reinforcing concrete structures with Fibre-Reinforced Polymers*, Design Manual No. 3, University of Manitoba, Winnipeg, Manitoba, Canada.

Issa, M.A., Amer, A. "Prestress losses in fibreglass pretensioned concrete compression members", Materials and Structures, Vol. 28, No. 06, July 1995, pp. 330-339.

MacGregor, J.G., Bartlett, F.M. (2000) Reinforced Concrete Mechanics and Design, First Canadian Edition, Prentice Hall, Scarborough, ON, Canada, 1042 pp.

Maple 17, *A mathematical analysis software*, Maplesoft™

Micro-Measurements (2012). *Strain Gage Thermal Output and Gage Factor Variation with Temperature*, Tech Note TN-504-1, Document No: 11054, North Carolina, USA.

Mota, C., Alminar,S., Svecova, D., "Critical Review of Deflection Formulas for FRP-RC Members", Journal of Composites for Construction, Vol. 10, No. 03, May/June 2006, pp. 183-194.

Mufti, A., Onofrrei, M., Rivera, E., Klowak, C., Bindiganavile, V., "Structural Health Monitoring of Field Trial Beam at Veteran Affairs Brookside Cemetery", Technical Report – ISIS Canada Research Network, November 2004.

Mufti, A., Onofrrei, M., Rivera, E., Klowak, C., Bindiganavile, V., "Structural Health Monitoring of Field Trial Beam at Veteran Affairs Brookside Cemetery", Technical Report – ISIS Canada Research Network, March 2005.

Mufti, A., Sidhu, D., Murison, E., Klowak, C., "Structural Health Monitoring of Field Trial Beam at Veteran Affairs Brookside Cemetery", Technical Report – Structural Health Monitoring Support Centre ISIS Canada, March 2007.

Nawy, E., Huang, P., “Crack and deflection control of pretensioned prestressed beams”, PCI Journal, Vol. 22, No. 03, Month 1977, pp. 30-47.

Naaman, A.E., Siriaksorn, A., "Serviceability Based Design of Partially Prestressed Beams: Part I: Analytical Formulation" Journal of the Prestressed Concrete Institute, Vol. 24, No. 2, March/April 1979, pp. 64-89.

Ohnuma, H., Nawa, T., Hironaga, M., Ozawa, M., “Effect of Low Temperature on the Creep Properties of Concrete”, Cement Science and Concrete Technology, No. 52, 1998, pp. 650-655.

Rao, S.V.K.M., Dilger, W.H., “Evaluation of Short-Term Deflections of Partially Prestressed Concrete Members”, ACI Structural Journal, Vol. 89, No. 01, January-February 1992, pp. 71-78.

Response-2000, *A Sectional Analysis Program*, University of Toronto.

Scanlon, A., Bischoff, P.H., “Shrinkage Restraint and Loading History Effects on Deflections of Flexural Members”, ACI Structural Journal, Vol. 105, No. 04, July-August 2008, pp. 498-506.

Scanlon, A., Murray, D.W., “Practical Calculation of Two-Way Slab Deflections” Concrete International, Vol. 4, No. 11, November 1982, pp. 43-50.

Sen, R., Issa, M., Mariscal, D., “Feasibility of Fiberglass Pretensioned Piles in a Marine Environment”, Report No. CEM/ST/92/1 Department of Civil Engineering and Mechanics, University of South Florida, Tampa, FL, August 1992.

Siriaksorn, A., Naaman, A.E., "Serviceability Based Design of Partially Prestressed Beams: Part II: Computerized Design and Parametric Evaluation" Journal of the Prestressed Concrete Institute, Vol. 24, No. 3, May-June 1979, pp. 40-60.

Somes, N.F., “Resin-bonded glass-fibre tendons for prestressed concrete”, Magazine of Concrete Research, Vol. 15, No. 45, November 1963, pp. 151-158.

Taerwe, L.R., Lambotte, H., Miesseler, H., “Loading Tests on Concrete Beams Prestressed With Glass Fiber Tendons”, PCI Journal, Vol. 37, No. 04, July-August 1992, pp. 84-97.

Tadros, M., Ghali, A., Meyer, A., Prestress loss and deflection of precast concrete members. PCI Journal, Vol. 30, No. 01, 1985, pp.114–141.

Wendner, R., Hubler, M.H., Bažant, Z.P., “The B4 model for multi-decade creep and shrinkage prediction”, Mechanics and Physics of Creep, Shrinkage, and Durability of Concrete, Ninth International Conference on Creep, Shrinkage, and Durability Mechanics, September 22-25, 2013, pp. 429-436.

Appendix A - Material Testing

All required tests on wet and dry concrete were performed in accordance with relevant ASTM standards.

A-1 Tests on Wet Concrete:

The total 12 slabs were completed with 9 different batches of concrete. The test results for all of them are listed in Table A-1.

Table A-1 Tests on Wet Concrete

Batch number	Cast Date	Slab Identification number	Air Content	Slump [mm]	Temperature [°C]
1	Sept 25, 2012	S-65-1	5 %	200	19.2
2	Sept 25, 2012	F-0-1	5 %	190	19.6
3	Oct 09, 2012	S-65-2	6.5 %	200	18.0
4	Oct 09, 2012	F-0-2	6.6 %	210	17.5
5	Oct 12, 2012	S-65-3	5.1 %	190	17.0
6	Oct 12, 2012	F-0-3	5.2 %	200	17.0
7	Feb 19, 2013	F-24-3 F-35-3	7 %	200	4.1
8	March 12, 2013	F-24-2 F-35-2	15 %	210	16.0
9	April 26, 2013	F-24-1 F-35-1	8 %	200	20.0

The following codes were referred for the determination of Slump, Air Content and Temperature:

Table A-2 ASTM Standards for Wet Concrete

Type of test	ASTM Code Designation	Code Title
Slump	C 143/C 143M	Standard Test Method for Slump of Hydraulic-Cement Concrete
Air Content	C 231	Standard Test Method for Air Content of Freshly Mixed Concrete by the Pressure Method
Temperature	C 1064/C 1064M	Standard Test Method for Temperature of Freshly Mixed Hydraulic-Cement Concrete

It should be noted that the concrete for batch 7, 8 and 9 was obtained from Lafarge ready mix plant and additional retarder was added in the mix design. The slabs for batch 1 to 6 were manufactured in the Lafarge precast plant without any retarder.

A-2 Tests on Hardened Concrete:

The tests were performed in accordance with ASTM C 496/C 496M (2011), and the test results are provided from Table A-3 to Table A-11

Table A-3 Concrete Properties Batch - 1 (Slab S-65-1)

Test type	Day 1 (Sept 26, 2012)	Day 7	Day 15	Day 28	Day 268
Split cylinder [MPa]	-	4.5	5.3	5.7	6.1
Compression test [MPa]	37.6	64.7	68.0	70.0	91.5
Modulus of Elasticity [MPa]	-	32 982	33 740	33 512	39 609

Table A-4 Concrete Properties Batch - 2 (Slab F-0-1)

Test type	Day 1 (Sept 26, 2012)	Day 7	Day 15	Day 28	Day 268
Split cylinder [MPa]	-	4.56	5.26	6.30	6.77
Compression test [MPa]	41.70	66.76	68.22	75.20	97.91
Modulus of Elasticity [MPa]	-	33 437	33 469	34 936	40 293

Table A-5 Concrete Properties Batch - 3 (Slab S-65-2)

Test type	Day 1 (Oct 10, 2012)	Day 7	Day 14	Day 29	Day 254
Split cylinder [MPa]	-	4.19	4.47	5.04	6.08
Compression test [MPa]	36.63	58.60	66.41	66.53	83.58
Modulus of Elasticity [MPa]	-	29 574	30 910	32 322	35 975

Table A-6 Concrete Properties Batch - 4 (Slab F-0-2)

Test type	Day 1 (Oct 10, 2012)	Day 8	Day 14	Day 29	Day 254
Split cylinder [MPa]	-	4.64	5.02	5.57	6.47
Compression test [MPa]	36.23	60.99	64.90	69.20	91.10
Modulus of Elasticity [MPa]	-	29 554	29 918	33 105	36 087

Table A-7 Concrete Properties Batch - 5 (Slab S-65-3)

Test type	Day 3 (Oct 15, 2012)	Day 7	Day 14	Day 28	Day 228
Split cylinder [MPa]	-	4.75	4.89	5.51	6.59
Compression test [MPa]	59.10	64.04	70.48	74.27	99.63
Modulus of Elasticity [MPa]	-	32 774	35 076	34 856	39 164

Table A-8 Concrete Properties Batch - 6 (Slab F-0-3)

Test type	Day 3 (Oct 15, 2012)	Day 7	Day 14	Day 28	Day 228
Split cylinder [MPa]	-	4.21	5.03	5.72	5.56
Compression test [MPa]	59.00	63.84	72.34	75.46	97.19
Modulus of Elasticity [MPa]	-	32 541	35 943	35 516	37 282

Table A-9 Concrete Properties Batch - 7 (Slab F-24-3 and F-35-3)

Test type	Day 3 (Feb 22, 2013)	Day 8	Day 16	Day 28	Day 45
Split cylinder [MPa]	3.33	4.54	4.54	4.92	5.09
Compression test [MPa]	40.20	57.01	63.76	67.12	68.05
Modulus of Elasticity [MPa]	25250	31 524	32 664	32 372	33 003

Table A-10 Concrete Properties Batch - 8 (Slab F-24-2 and F-35-2)

Test type	Day 3 (March 15, 2013)	Day 7	Day 15	Day 28	Day 100
Split cylinder [MPa]	2.88	3.35	3.30	3.27	3.05
Compression test [MPa]	28.57	36.58	38.52	45.99	41.52
Modulus of Elasticity [MPa]	20401	24 082	24 716	26 310	25 316

Table A-11 Concrete Properties Batch - 9 (Slab F-24-1 and F-35-1)

Test type	Day 3 (April 29, 2013)	Day 7	Day 14	Day 28	Day 55
Split cylinder [MPa]	4.14	4.09	4.74	5.04	4.84
Compression test [MPa]	46.93	59.10	67.56	72.09	70.69
Modulus of Elasticity [MPa]	29113	32 532	34 487	35 226	34 956

Additional two cylinders from batch 5 and batch 7 were tested with the ESG installed for strain readings. The stress strain curves for both are presented in Figure 4-27 and Figure 4-28.

A-3 Unit Weight of Concrete

Due to the large variability of air content in concrete, the unit weight of concrete is calculated from measuring the weight of five cylinders with the known volume. The obtained unit weight is listed in Table A-12

Table A-12 Unit Weight of Concrete

Concrete batch	Slab ID	Unit Wt [kN/m³]
1	S-65-1	23.50
2	F-0-1	23.50
3	S-65-2	23.00
4	F-0-2	23.00
5	S-65-3	23.50
6	F-0-3	23.50
7	F-24-3 and F-35-3	23.00
8	F-24-2 and F-35-2	20.64
9	F-24-1 and F-35-1	23.00

A-4 GFRP

Tension tests were performed as per CAN/CSA S806-12 (2012) and the modulus of elasticity is calculated from Eq A-1. Total six rebars were tested with the installed strain gauges. The modulus of elasticity and failure load are presented in Table A-13. The load versus strain graphs are shown in Figure A-1.

$$E_{gfrp} = \frac{1000(P_1 - P_2)}{(\varepsilon_1 - \varepsilon_2)A_{gfrp}} \qquad \text{Eq A-1}$$

P_1 & ε_1 = load and corresponding strain, respectively, at about 50% of the ultimate load

P_2 & ε_2 = load and corresponding strain, respectively, at about 25% of the ultimate load

A_{gfrp} = Nominal cross-sectional area of rebar

E_{gfrp} = Modulus of elasticity as per CAN/CSA S806-12 (2012)

Table A-13 GFRP Tension Test

Rebar number	Modulus of Elasticity [MPa]	Failure Stress [MPa]	ε_{max}
G-1	53923.3	829.6	15869.6
G-2	55698.3	869.5	15528.4
G-3	55603.2	865.6	15674.9
G-4	54592.8	888.9	16417.4
Average	**54954.4**	**863.4**	**15872.6**

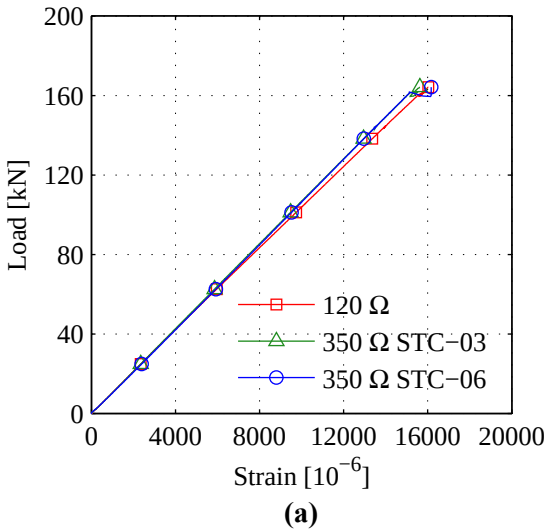

(a)

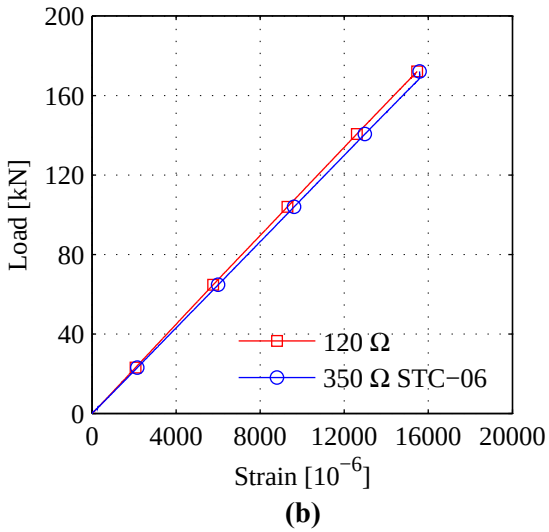

(b)

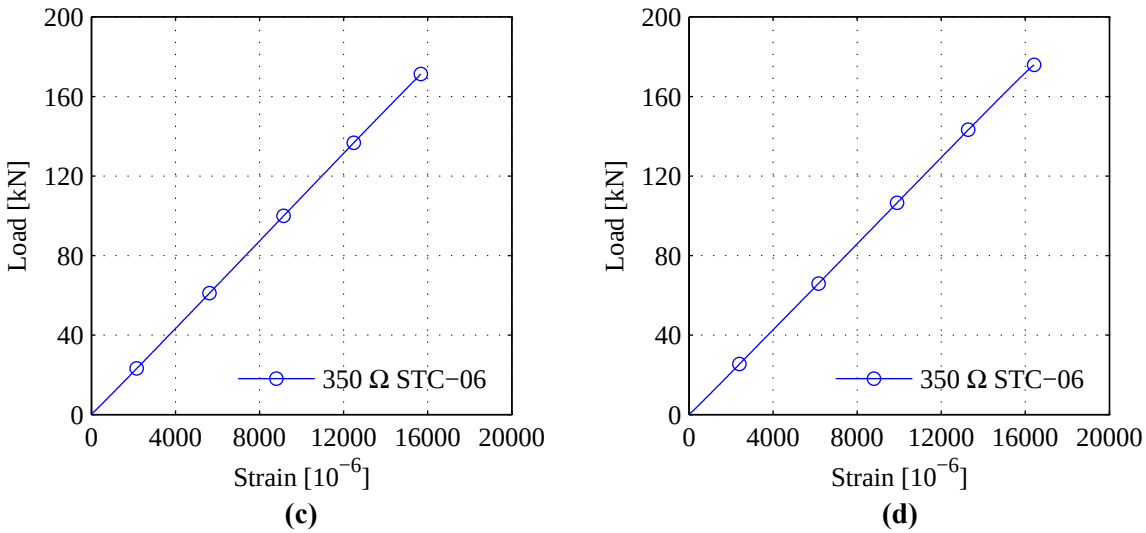

Figure A-1 GFRP Tension Test Results
for (a) G-1, (b) G-1, (c) G-1, (d) G-1

Appendix B – Test Results

B-1 Prestressing of GFRP Slabs

During prestressing the slabs, strains were recorded against time. The prestresssing strains of GFRP in slabs F-24-1 and F-35-1 are shown below.

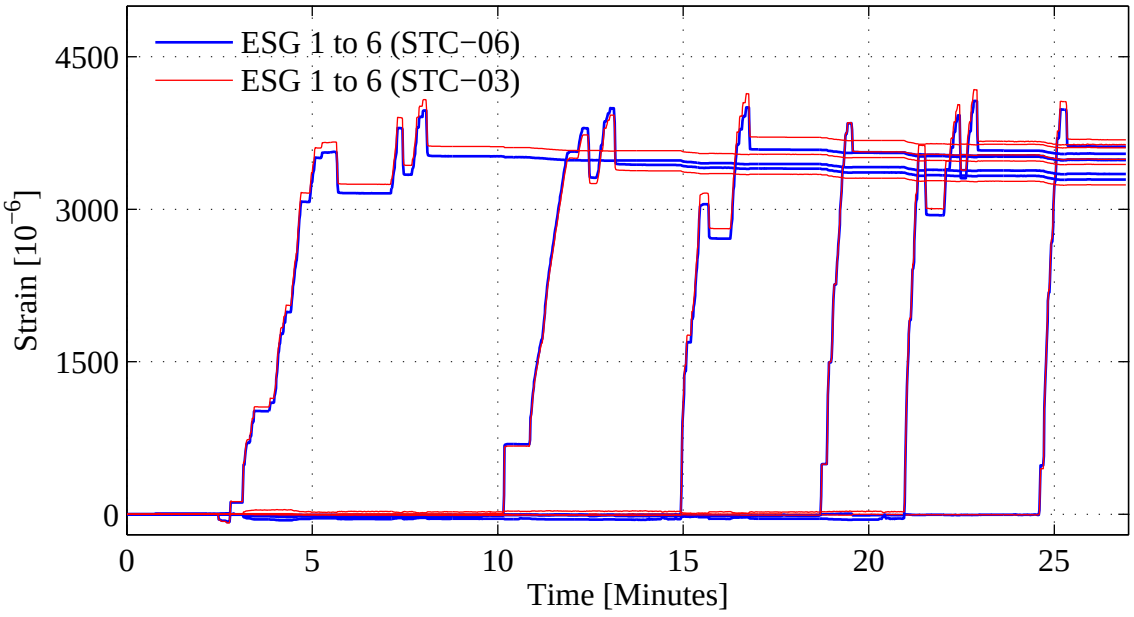

(a)

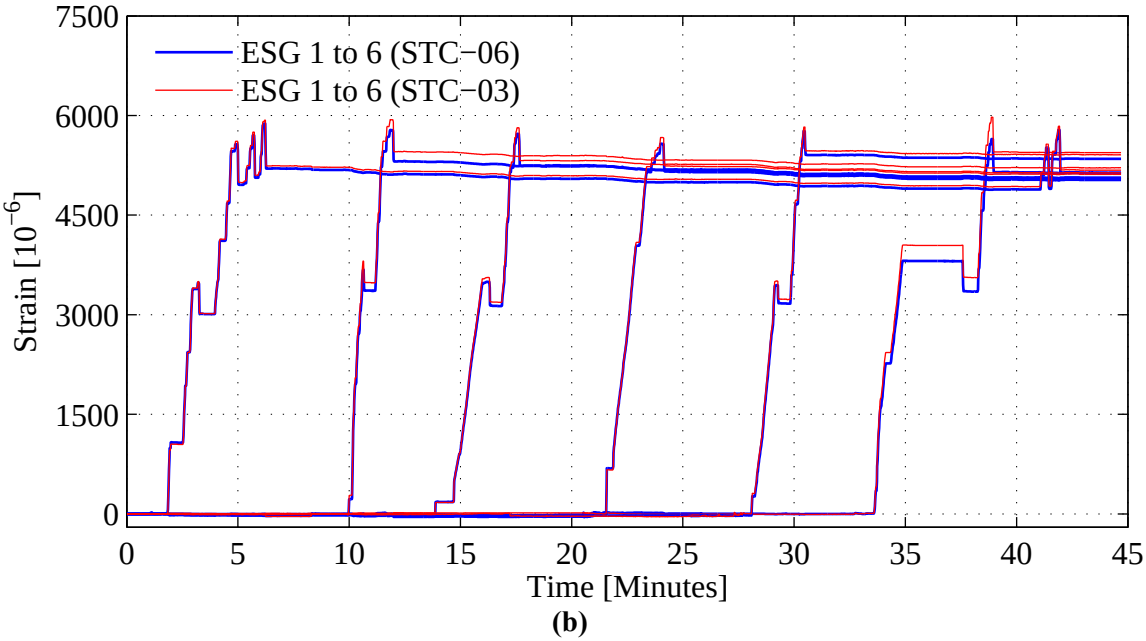

(b)

Figure B-1 Prestressing of GFRP Slabs (a) Slab F-24-1, (b) Slab F-35-1

B-2 Concrete Curing Temperature

The temperature variation during the process of concrete curing is shown in Figure B-2

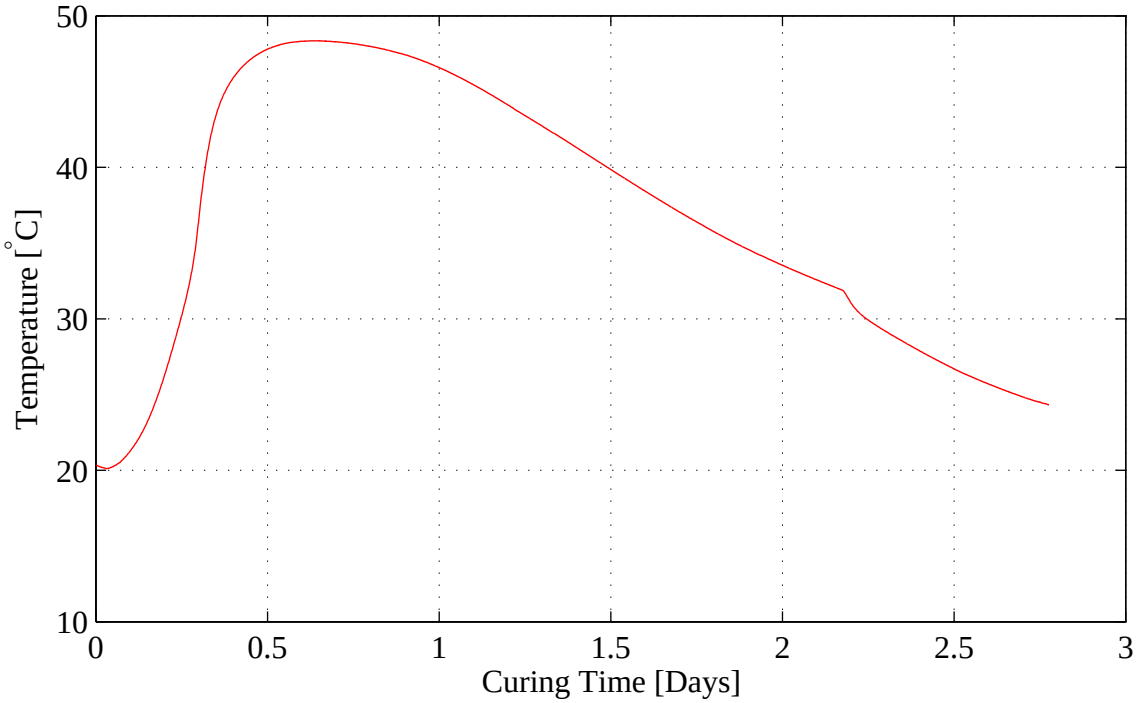

(a)

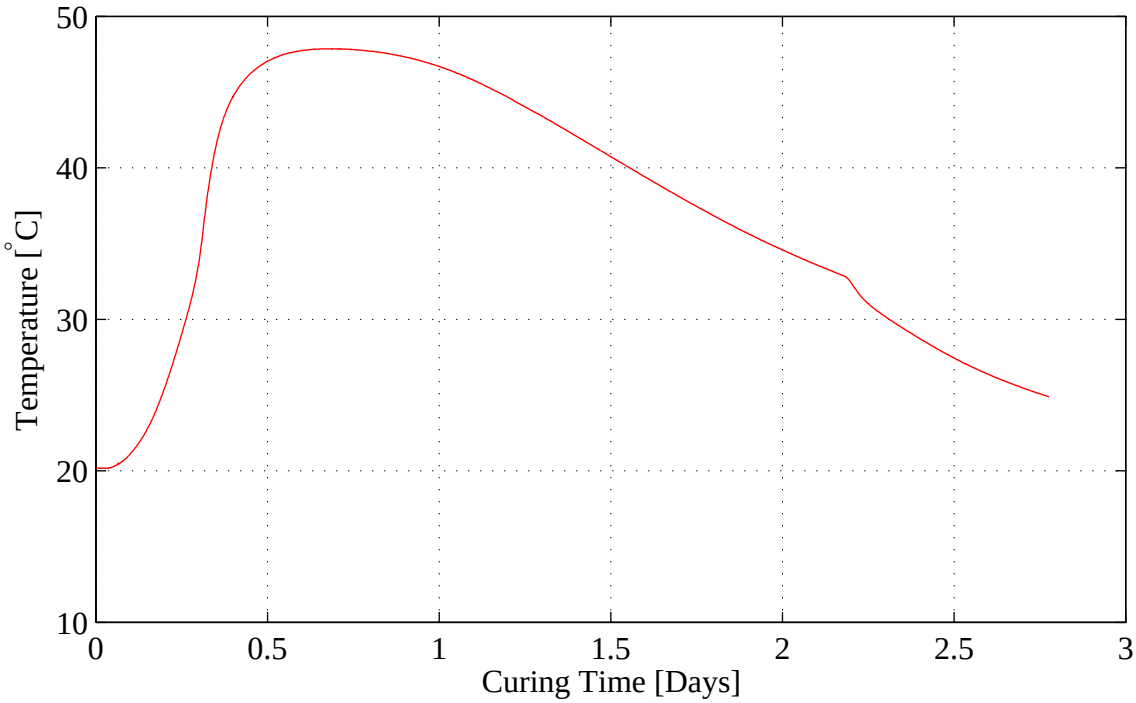

(b)

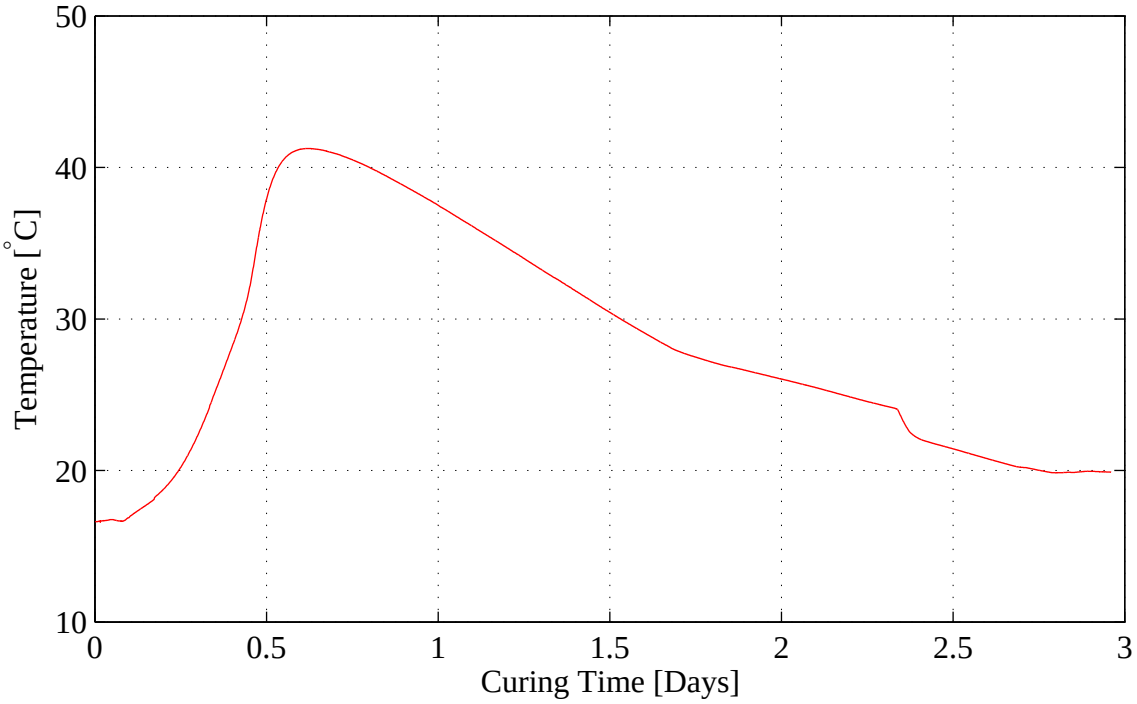

(c)

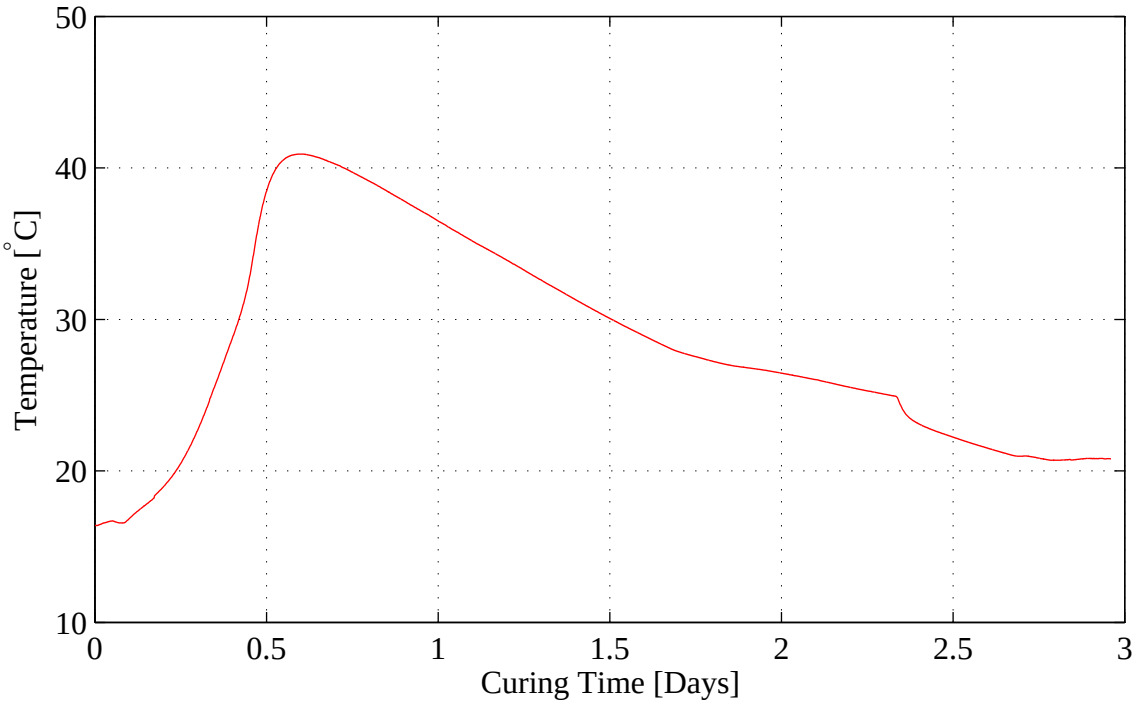

(d)

Figure B-2 Temperature During Curing for Slabs
(a) F-24-1, (b) F-35-1, (c) F-24-2, (d) F-35-2

B-3 Transfer of Prestress

The strains in reinforcement during the transfer of prestress and flipping of slabs to upside up position is shown in Figure B-3.

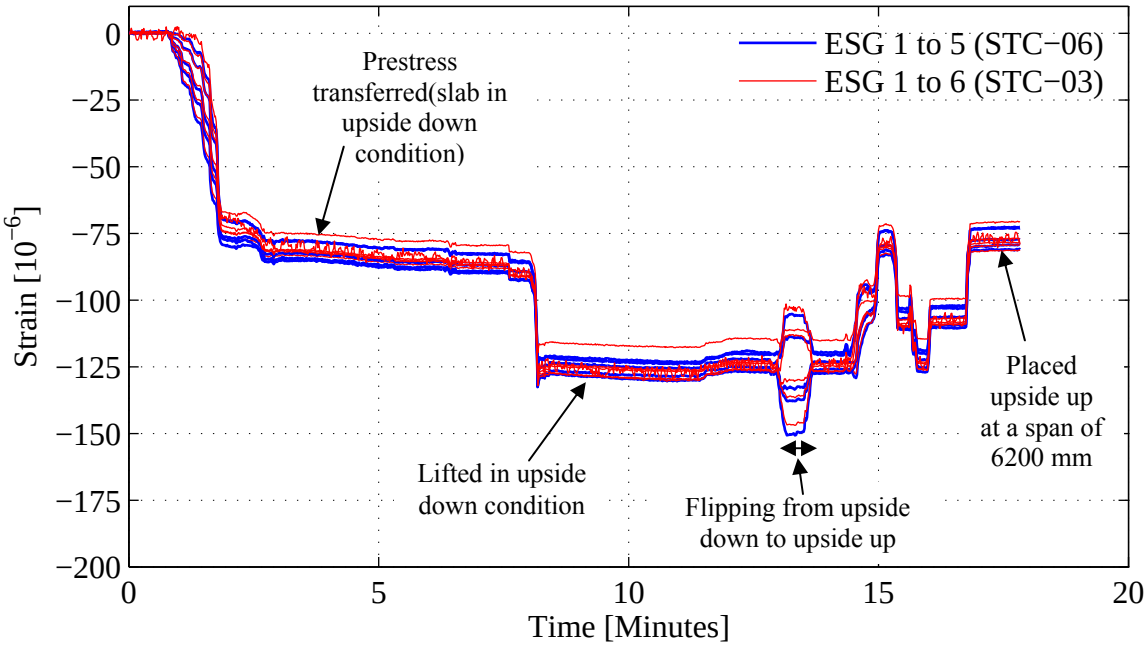

(a)

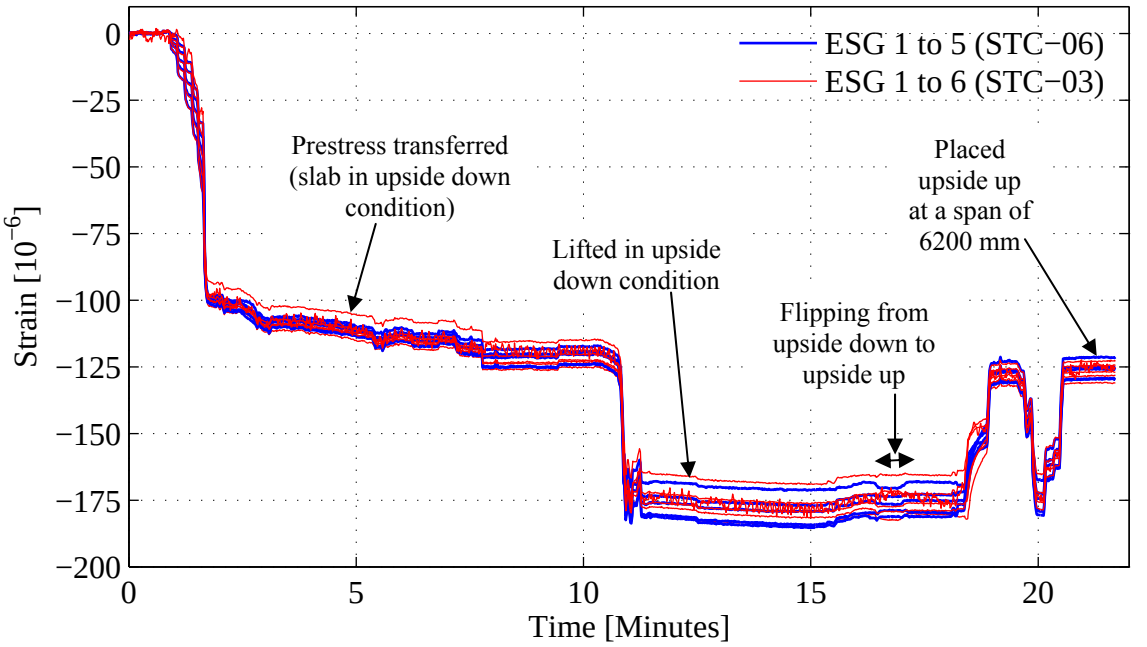

(b)

Figure B-3 Transfer of Prestress and Flipping (a) F-24-1 (b) F-35-1

B-4 Strain Profiles at Mid-Span

The comparison of the strains versus load across the height of the member at mid-span is shown in Figure B-4 (a) to (d).

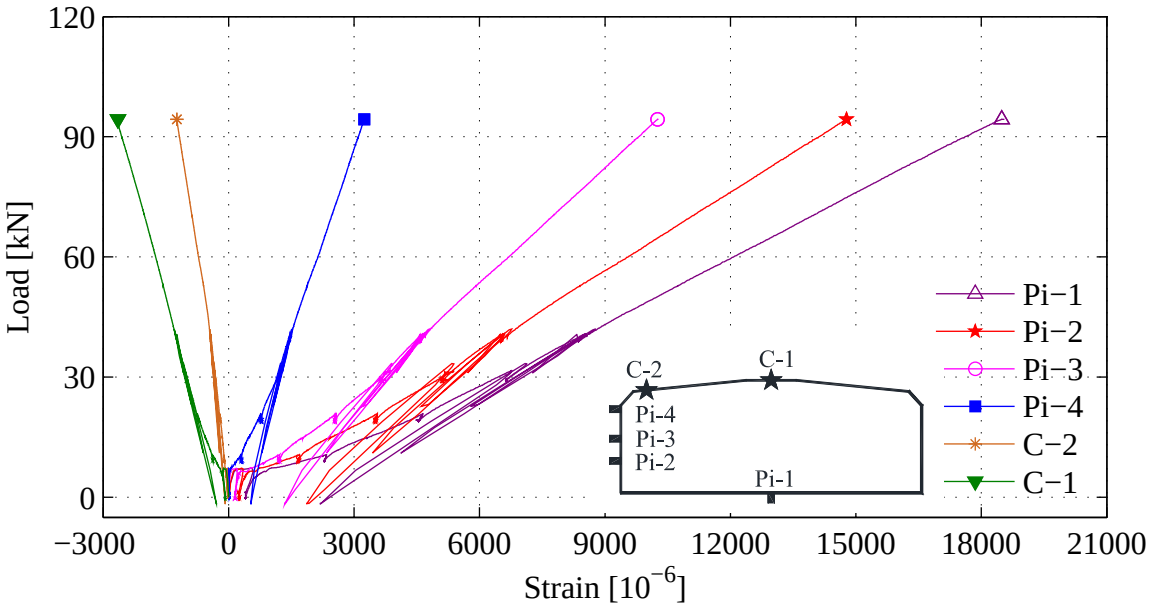

(a)

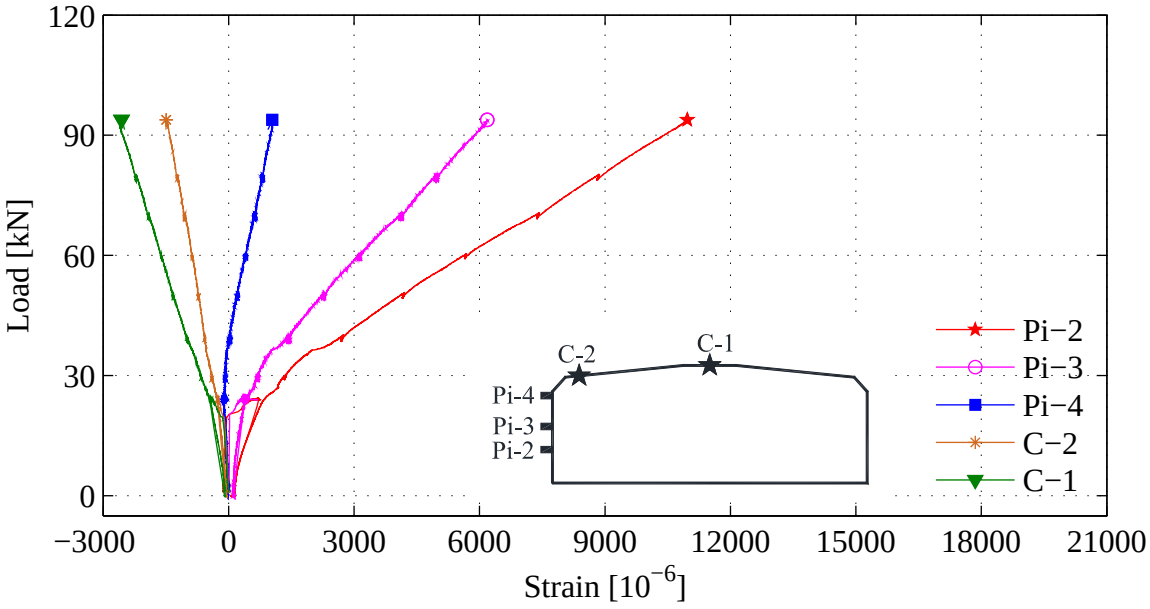

(b)

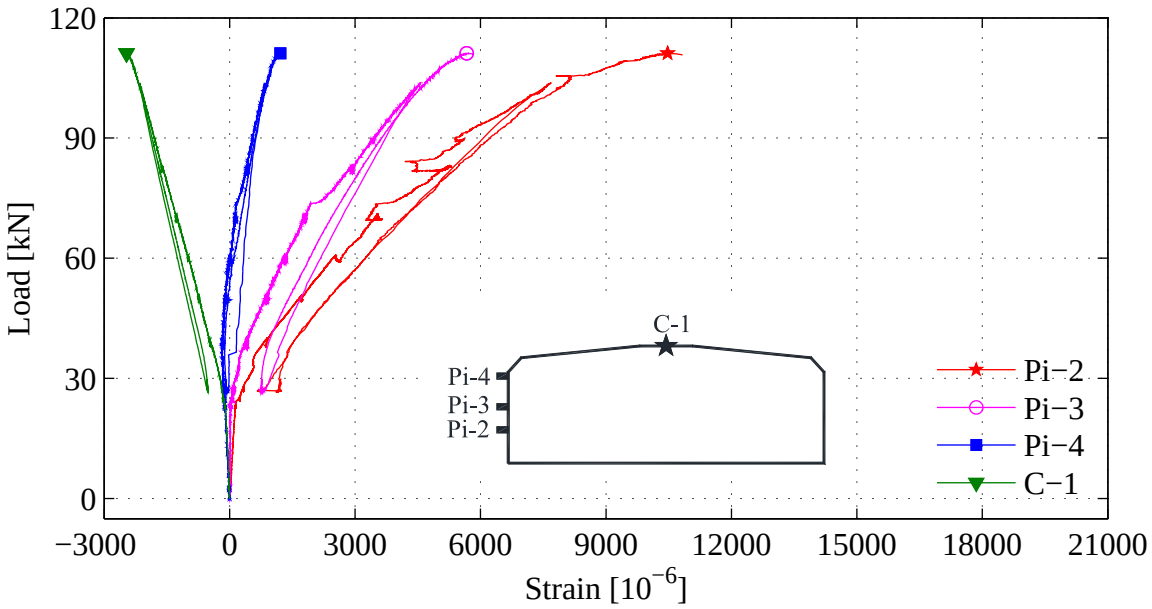

(c)

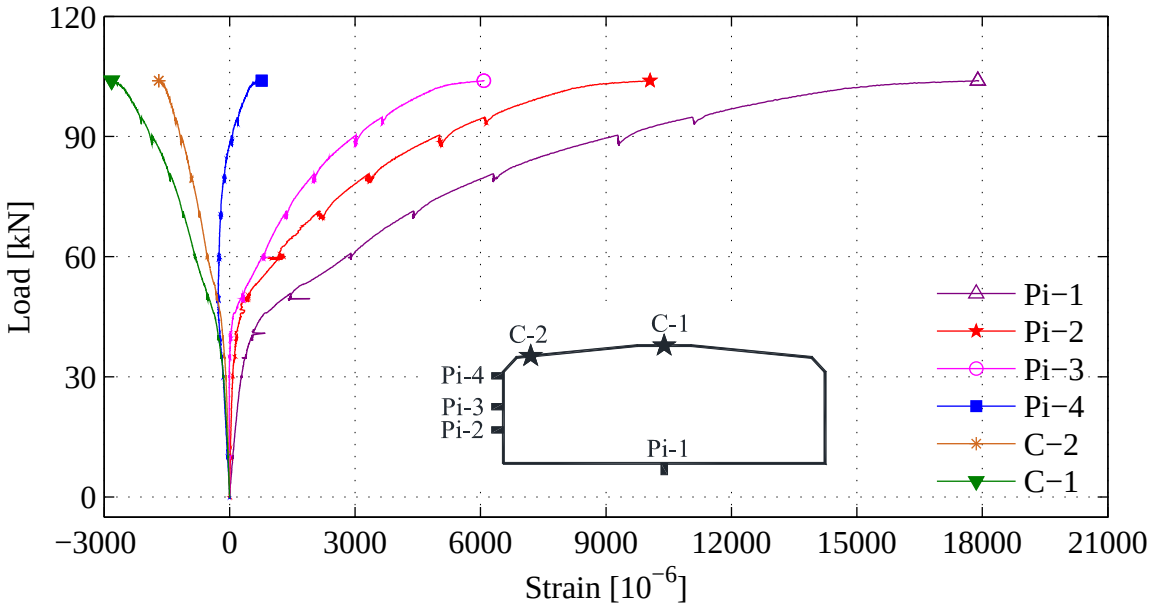

(d)

Figure B-4 Strain-Load Across the Depth at Mid-Span for (a) F-0-3, (b) F-24-3, (c) F-35-3, (d) S-65-3

Figure B-5 expresses the variation of strains across the depth of member with respect to the load at 25%, 50 %, 75% and 100% of the ultimate capacity of the slab. The variation of strains obtained from the experiments is nearly straight line with the increase in load.

Thus the assumption that plain section remains plane before and after bending closely resembles the experimental results.

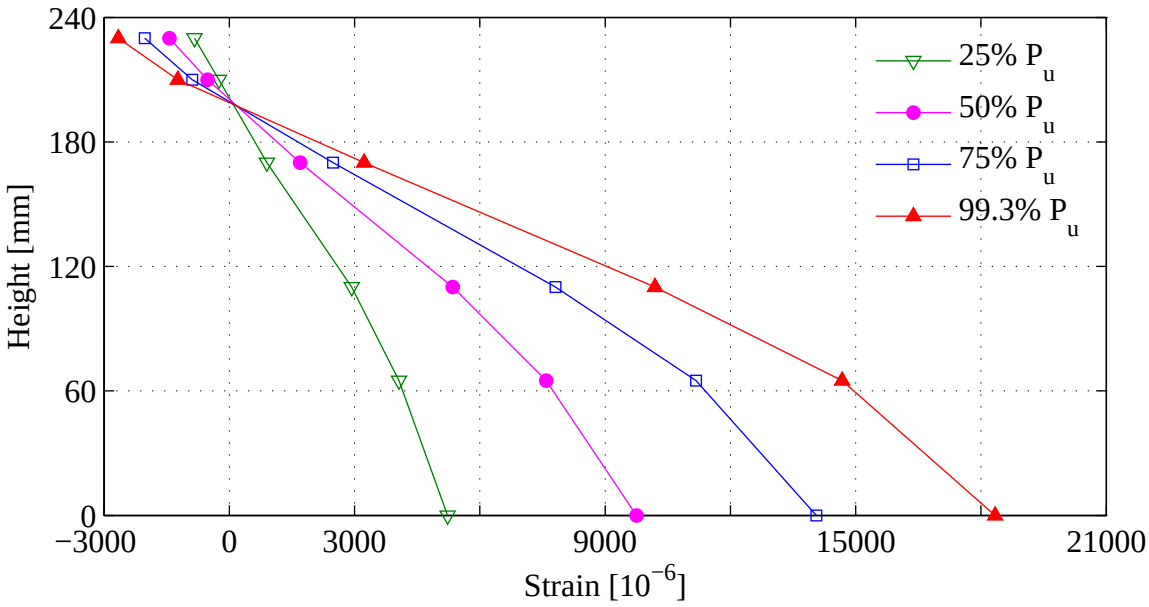

(a)

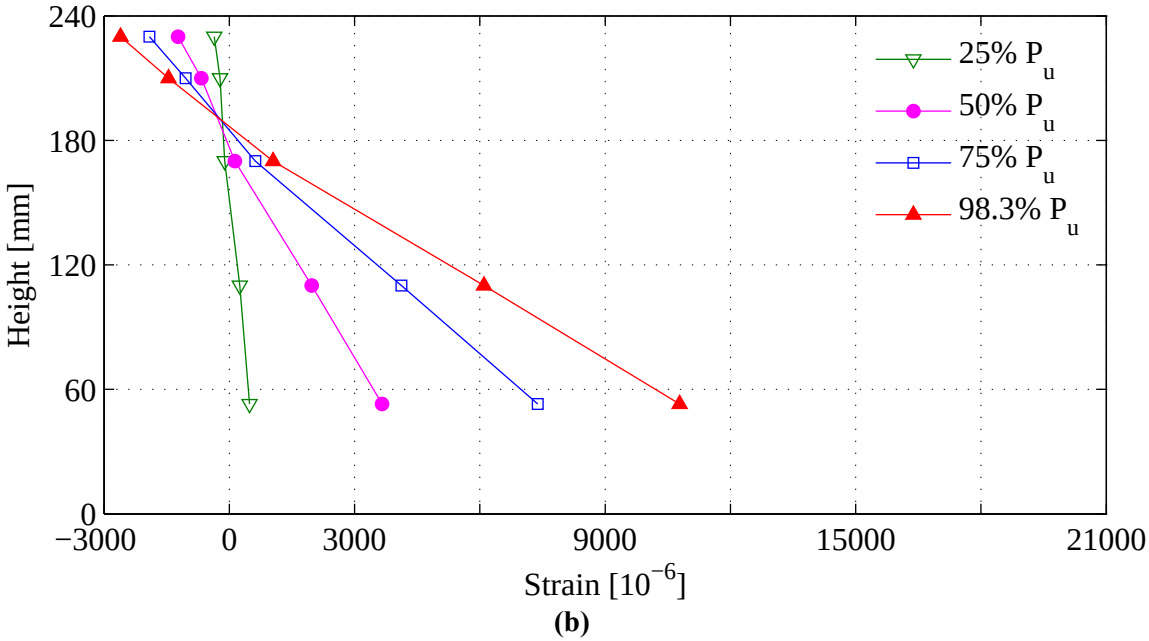

(b)

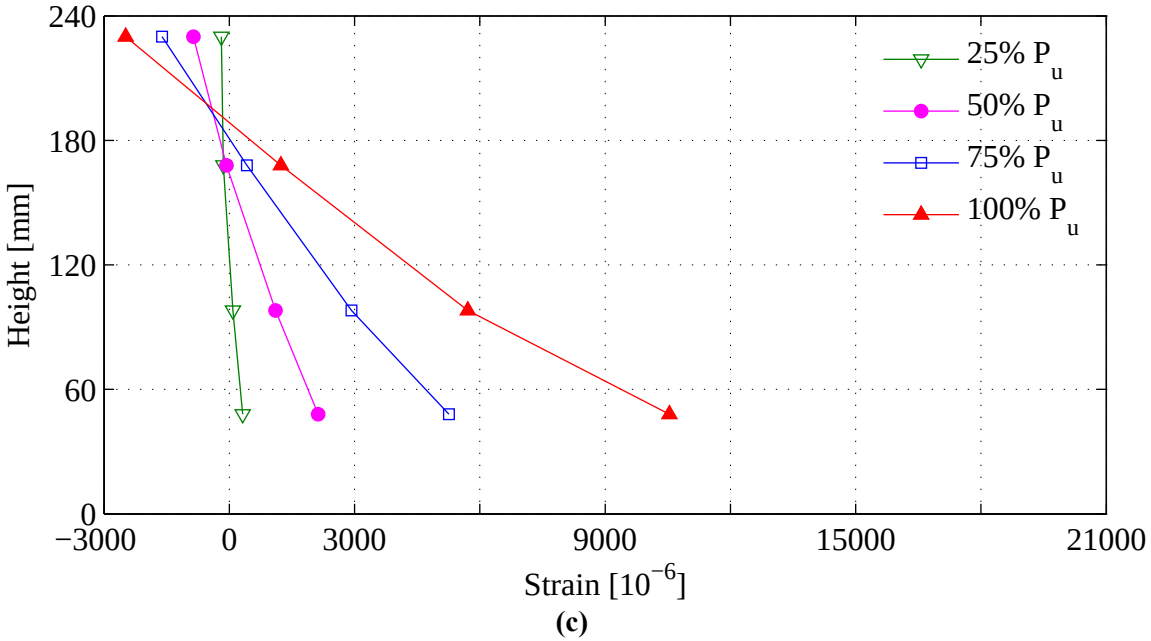

(c)

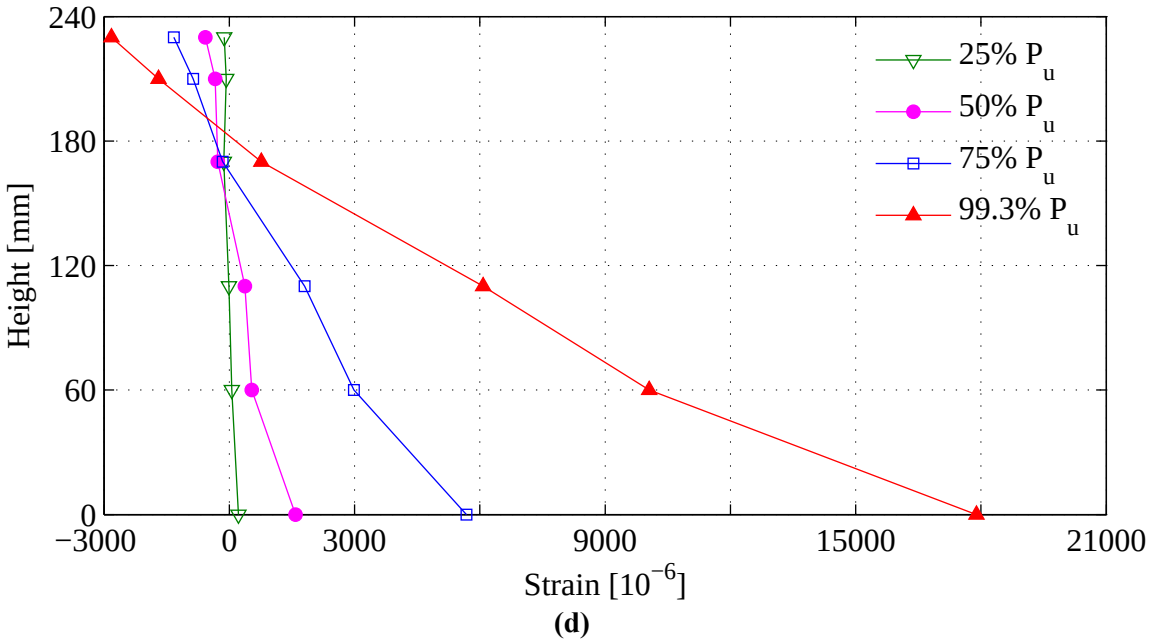

(d)

Figure B-5 Strain Profile at Mid Span
for (a) F-0-3, (b) F-24-3, (c) F-35-3, (d) S-65-3

B-5 Deflection Profile Along the Slab

For short term tests, six LVDTs were used to acquire the deflection response at five points along the span. The deflection at mid span was obtained from two LVDTs attached on top of the slab near both the edges to capture any possible torsional deflection,

however no torsion was observed from the recorded readings. Figure B-6 represents the deflection along the span at 25%, 50%, 75% and 100% of the ultimate capacity of slabs.

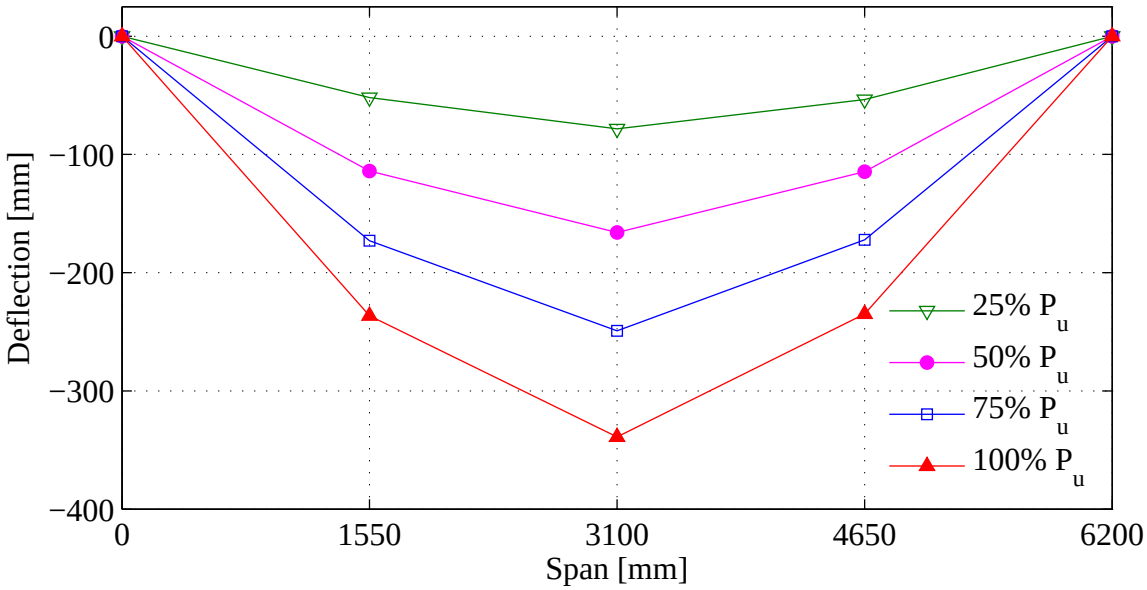

(a)

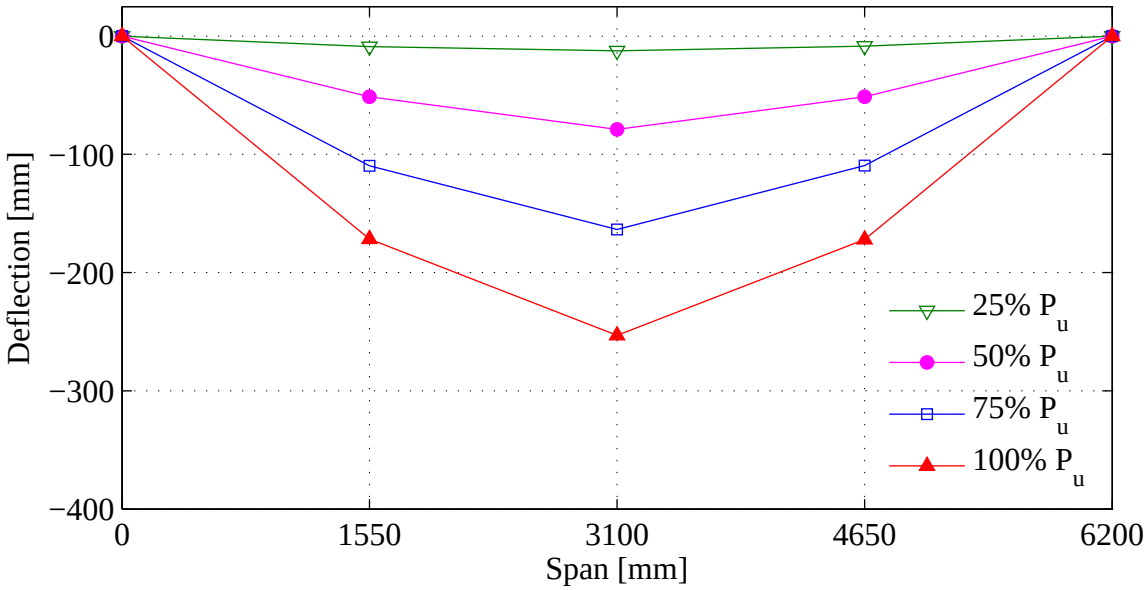

(b)

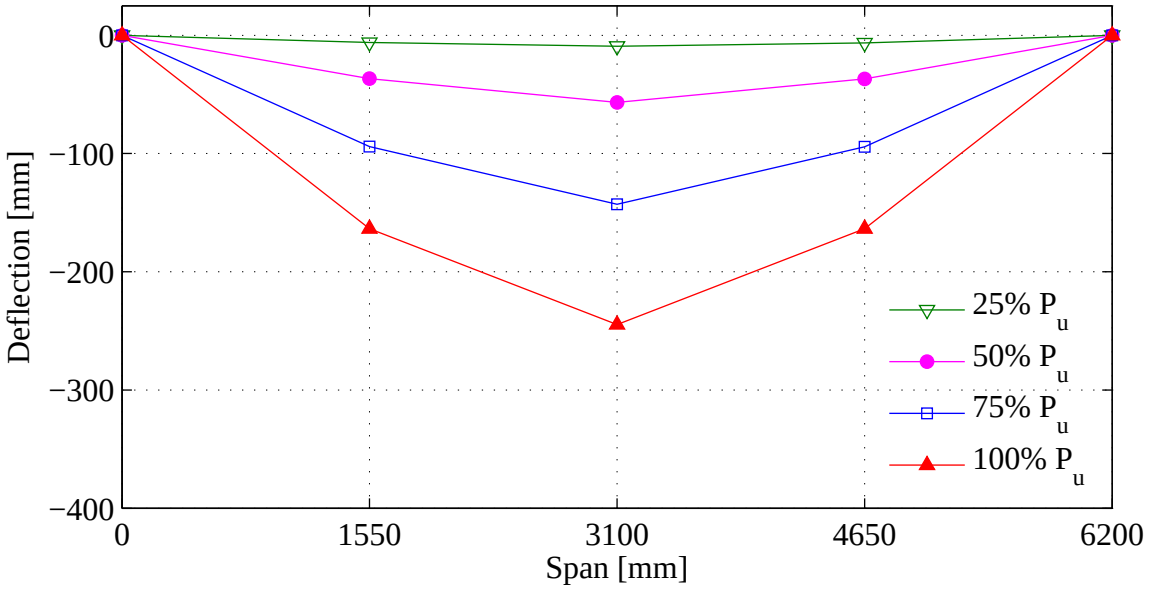

(c)

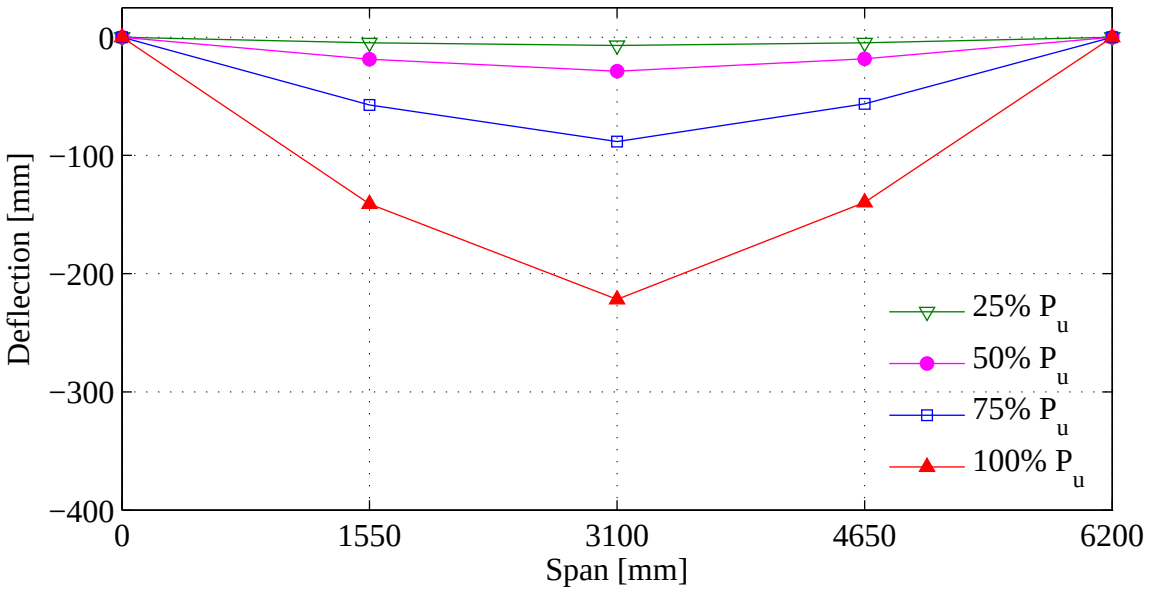

(d)

Figure B-6 Deflection Profile During Destructive Testing for (a) F-0-3, (b) F-24-3, (c) F-35-3, (d) S-65-3

The particulars of destructive tests are described below.

B-6 Test Details

In short term testing of slab F-0-3 initially the load was applied at the rate of 5 mm per minute with the 5000 kN displacement controlled MTS machine up to 7 kN, the loading

was stopped and new cracks were marked. At 7 kN load the strain in the rebars increased rapidly due to the occurrence of new cracks. It can also be seen from the load deflection curve that there is a distinguished difference in slope of the load deflection diagram at 7 kN. From 7 kN to 20 kN the rate of loading was 10 mm per minute and the cracks were marked at every 10 kN of external load up to 40 kN. From 20 to 40 kN the rate of loading was 15 mm/min and after 40 kN the rate was increased to 25 mm/min.

For slabs F-24-3, F-35-3 and S-65-3, the pre-cracking loading rate was maintained at 3mm/min. After cracking, the loading rate for the next 10 kN was kept at 10mm/min and beyond that it was increased to 15 mm/ min upto failure of slabs.

B-7 Crack Pattern

Over the period of time all three GFRP rebar non-prestressed slabs were cracked under their own weight. The crack pattern for these slabs is shown in Figure B-7

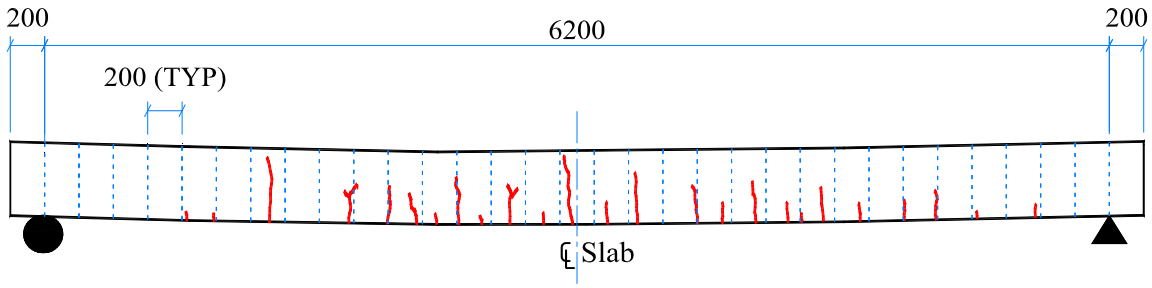

(a)

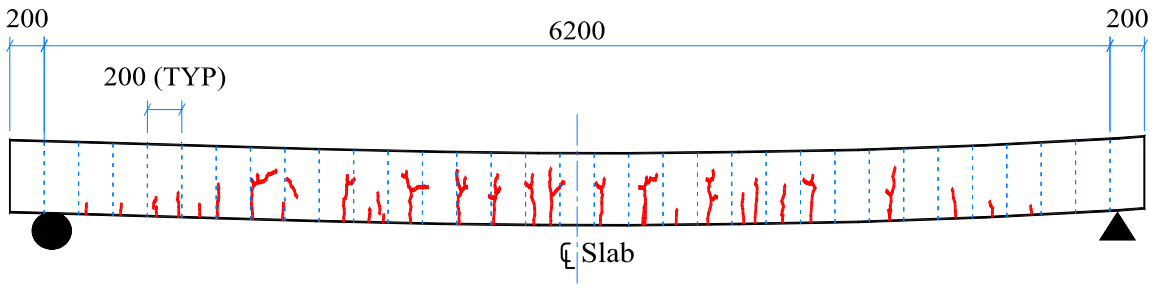

(b)

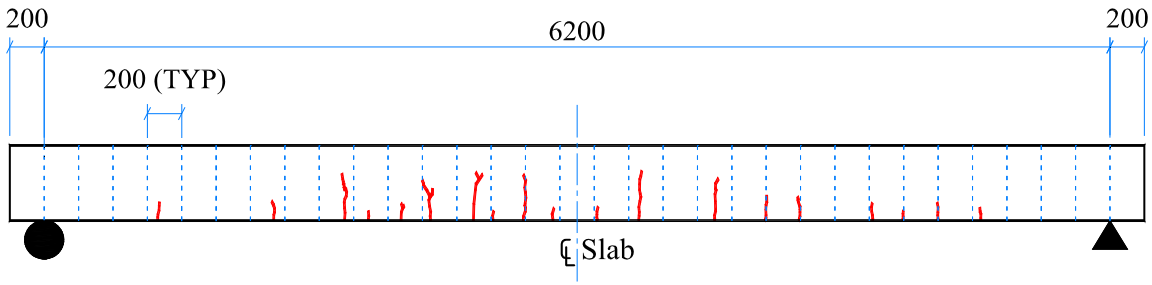

(c)

Figure B-7 Cracks Due to Self-Weight for Slabs F-0
(a) F-0-1 at Age of 266 Days, (b) F-0-2 at Age of 251 Days, (c) F-0-3 at Age of 216 Days

The slabs prestressed with GFRP and steel were pre-cracked to bring them to the same conditions of cracked GFRP reinforced slabs. The crack pattern achieved due to pre-cracking is shown from Figure B-8

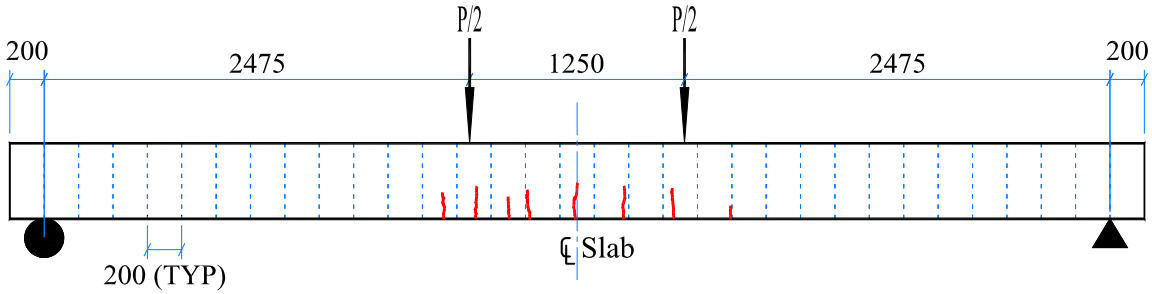

(a)

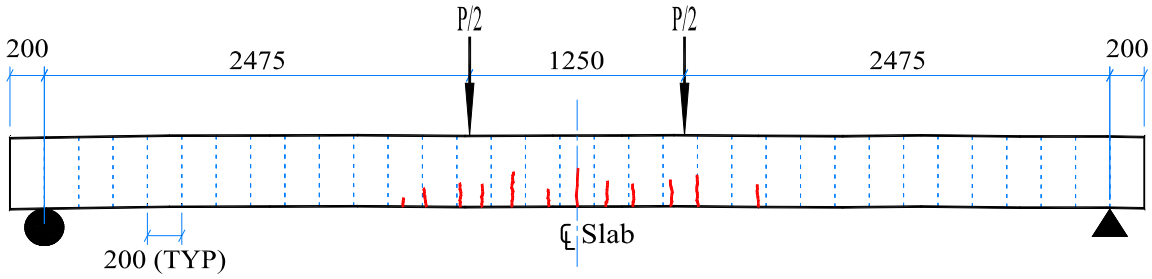

(b)

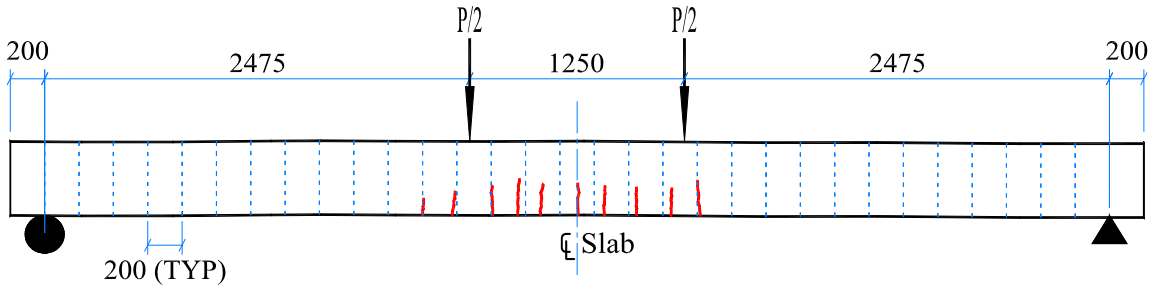

(c)

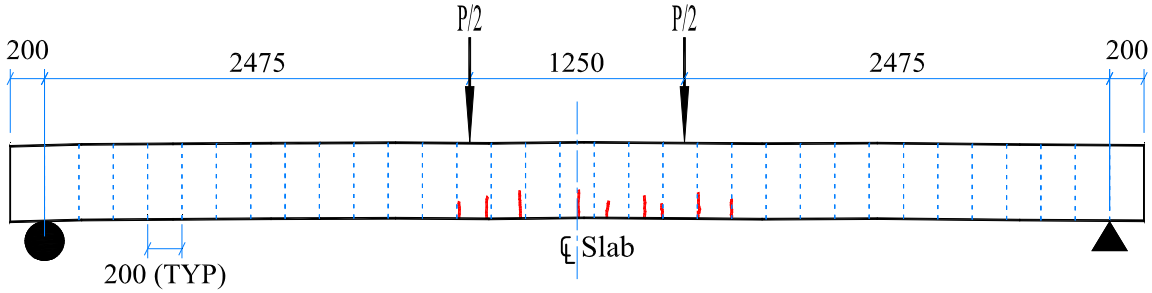

(d)

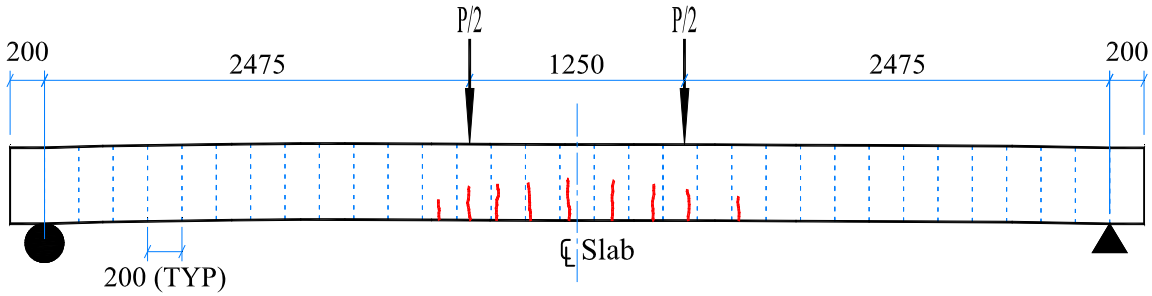

(e)

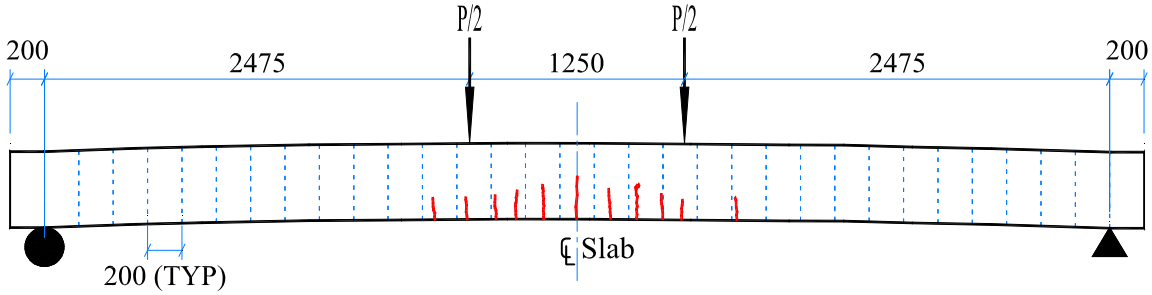

(f)

Figure B-8 Cracks due to Pre-Cracking for Slabs F-24, F-35 and S-65
(a) F-24-1 at Age of 46 Days, (b) F-24-2 at Age of 90 Days, (c) F-35-1 at Age of 46 Days, (d) F-35-2 at Age of 90 Days, (e) S-65-1 at Age of 261 Days, (f) S-65-2 at Age of 246 Days

B-8 Shrinkage of Concrete

The shrinkage results obtained from ACI 209R-92, CEB MC90-99 and Bažant-Baweja B3 are presented in Figure B-9 below.

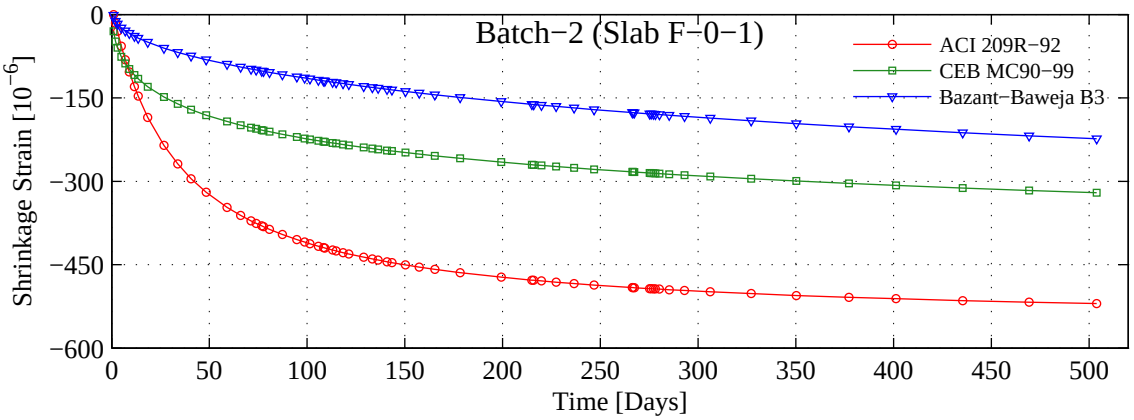

(a)

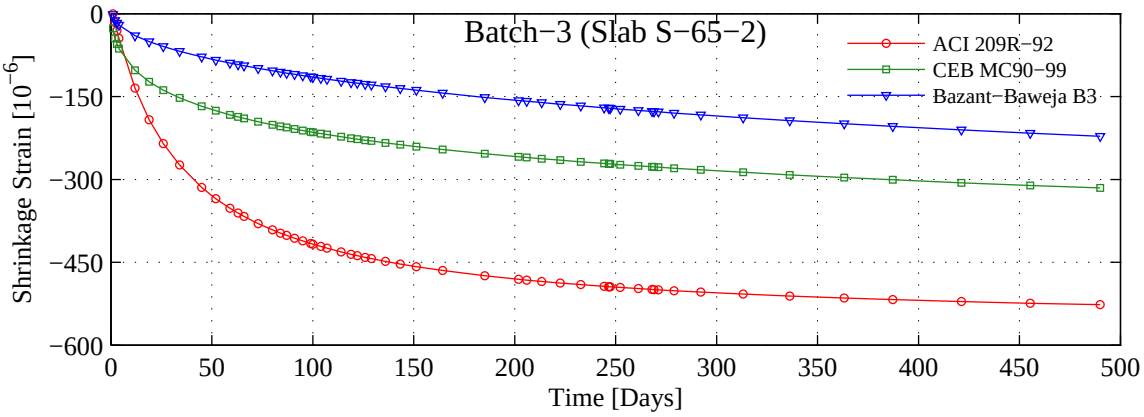

(b)

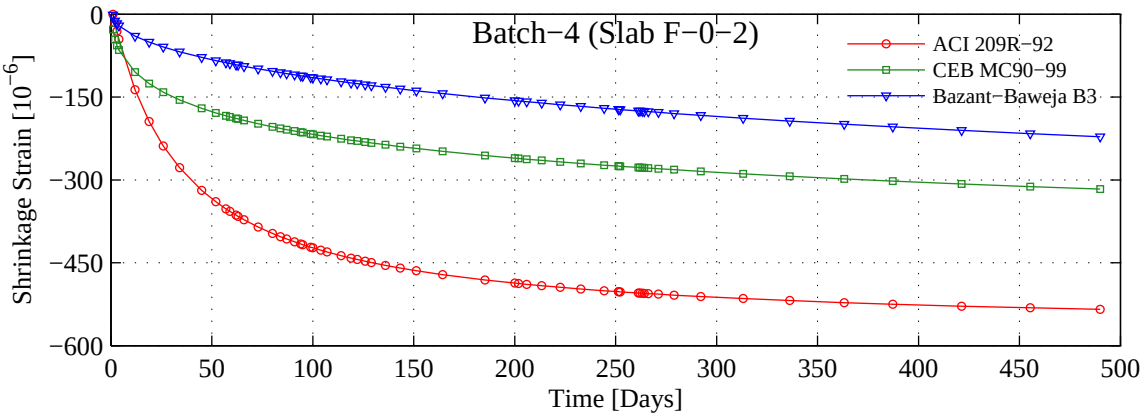

(c)

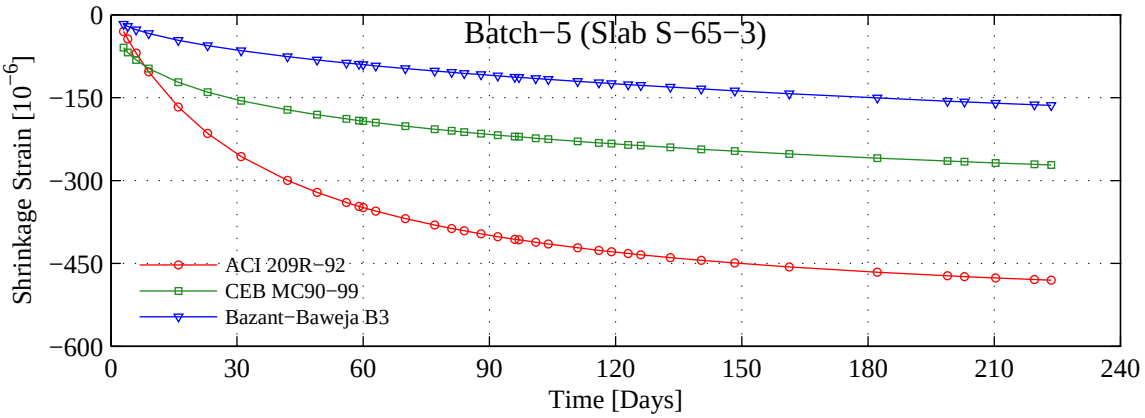
Batch−5 (Slab S−65−3)
Shrinkage Strain [10^−6]
0
−150
−300
−450
−600
0
30
60
90
120
150
180
210
240
Time [Days]
ACI 209R−92
CEB MC90−99
Bazant−Baweja B3

(d)

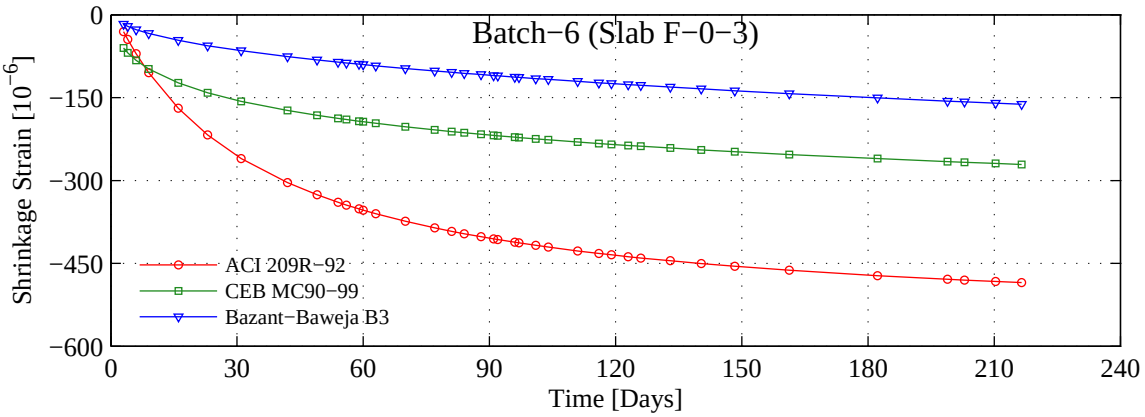
Batch−6 (Slab F−0−3)
Shrinkage Strain [10^−6]
0
−150
−300
−450
−600
0
30
60
90
120
150
180
210
240
Time [Days]
ACI 209R−92
CEB MC90−99
Bazant−Baweja B3

(e)

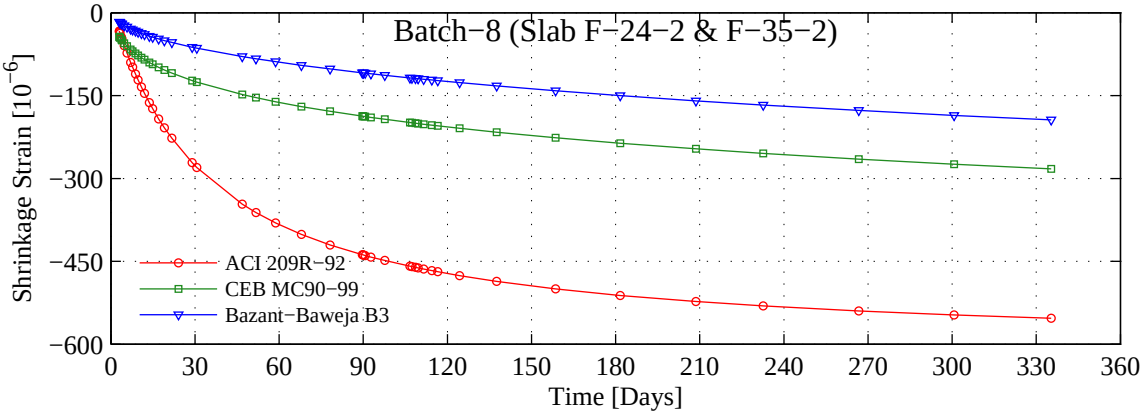
Batch−8 (Slab F−24−2 & F−35−2)
Shrinkage Strain [10^−6]
0
−150
−300
−450
−600
0
30
60
90
120
150
180
210
240
270
300
330
360
Time [Days]
ACI 209R−92
CEB MC90−99
Bazant−Baweja B3

(f)

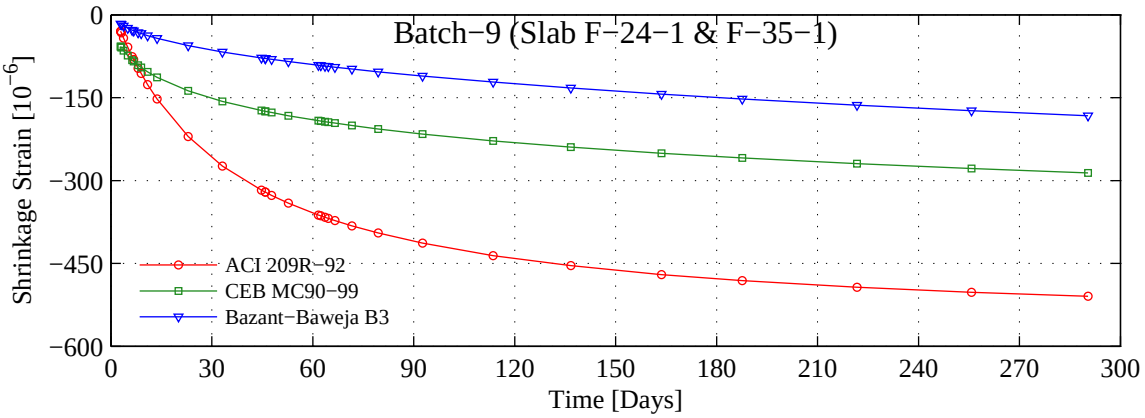

(g)

Figure B-9 Shrinkage Strain Comparison for Concrete
(a) Batch-2, (b) Batch-3, (c) Batch-4, (d) Batch-5, (e) Batch-6, (f) Batch-8,(g) Batch-9

B-9 Compliance of Concrete

The prediction of compliance obtained from ACI 209R-92 (1992), CEB MC90-99 (1999) and Bažant-Baweja B3(1995) are presented in Figure B-10 below.

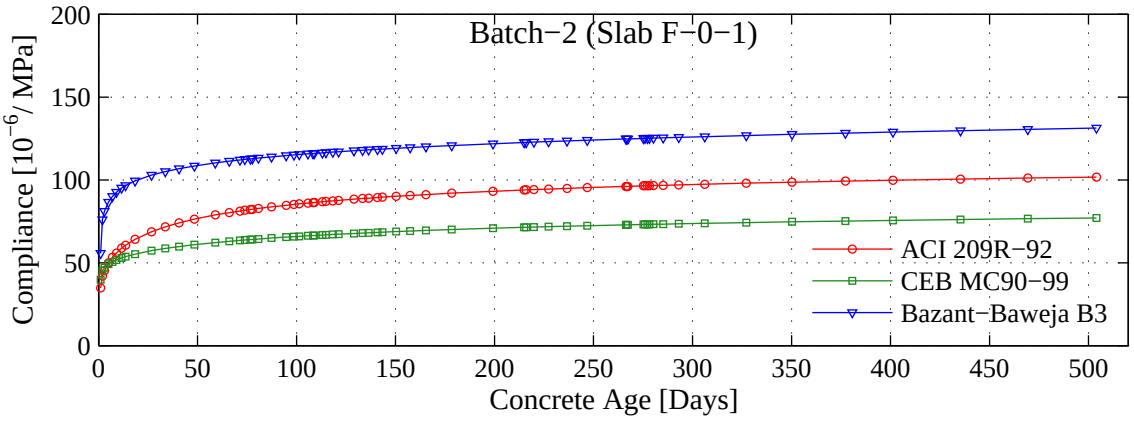

(a)

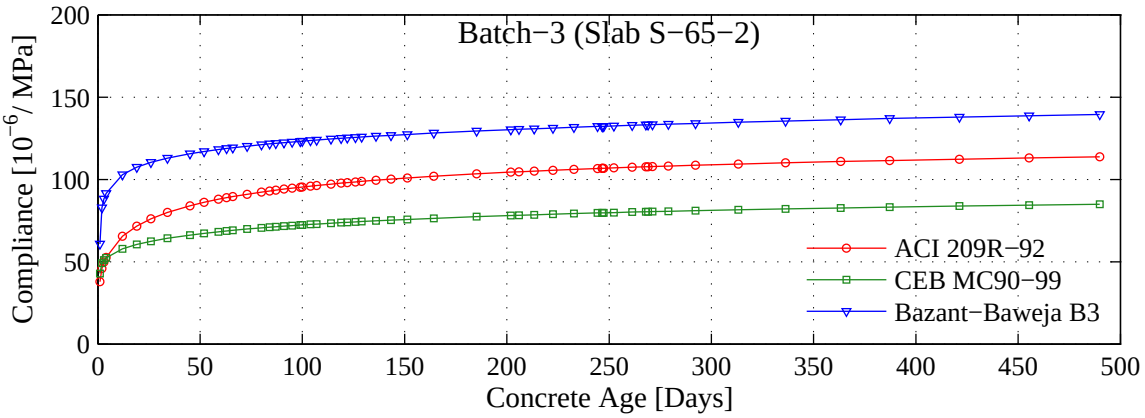
Batch−3 (Slab S−65−2)
Compliance [10−6/ MPa]
Concrete Age [Days]
ACI 209R−92
CEB MC90−99
Bazant−Baweja B3
0
50
100
150
200
250
300
350
400
450
500

(b)

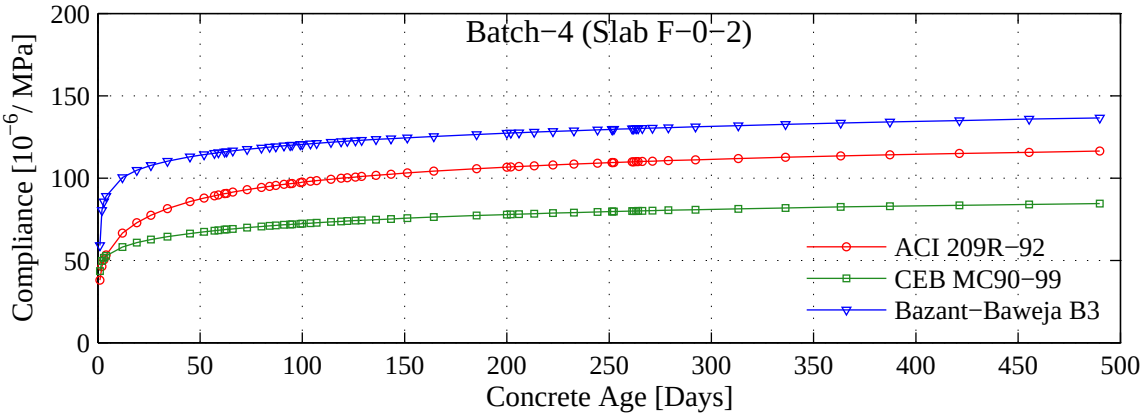
Batch−4 (Slab F−0−2)
Compliance [10−6/ MPa]
Concrete Age [Days]
ACI 209R−92
CEB MC90−99
Bazant−Baweja B3
0
50
100
150
200
250
300
350
400
450
500

(c)

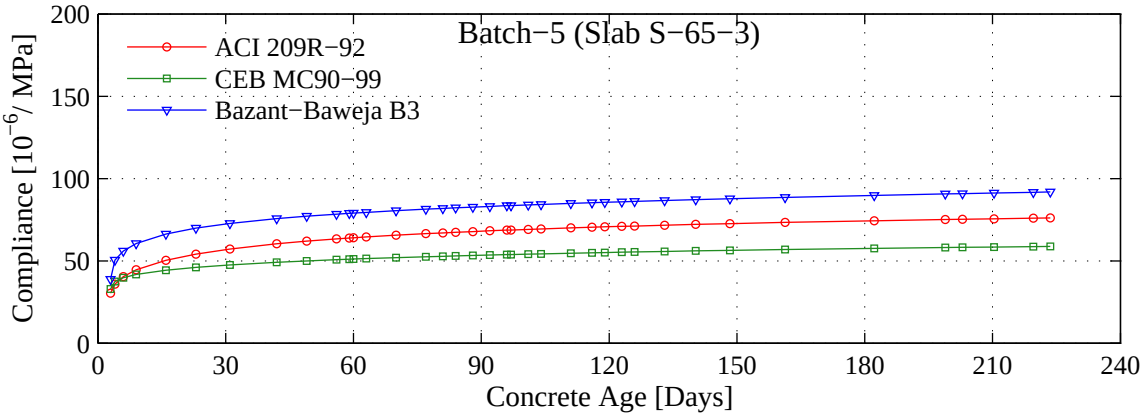
Batch−5 (Slab S−65−3)
Compliance [10−6/ MPa]
Concrete Age [Days]
ACI 209R−92
CEB MC90−99
Bazant−Baweja B3
0
30
60
90
120
150
180
210
240

(d)

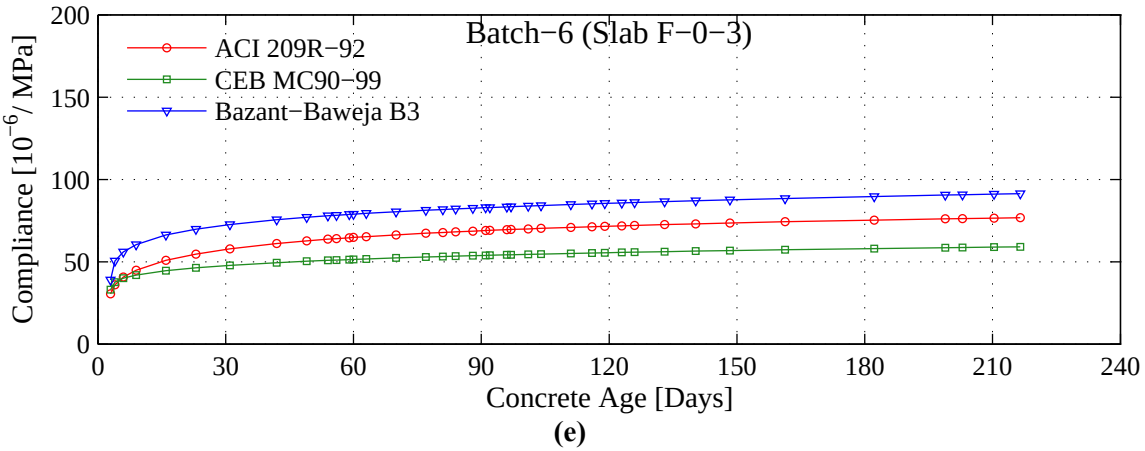

(e)

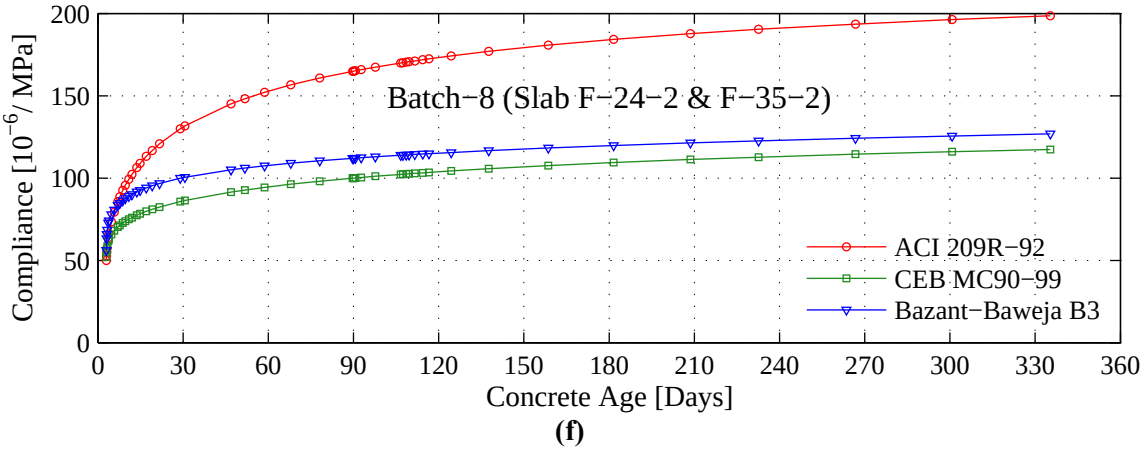

(f)

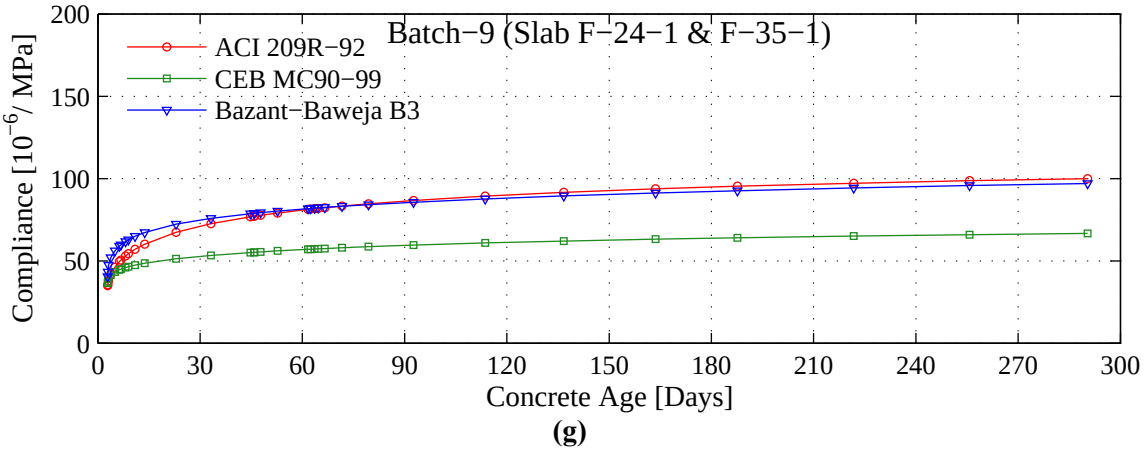

(g)

Figure B-10 Compliance Predictions of Concrete
(a) Batch-2, (b) Batch-3, (c) Batch-4, (d) Batch-5, (e) Batch-6, (f) Batch-8,(g) Batch-9

Appendix C – Theoretical Analysis

This section describes only the calculation of compressive force in concrete compression zone and its moment about the reinforcement.

In the cross-sectional analysis true stress-strain properties of concrete have been used. The slabs had trapezoidal shape in the compression zone of concrete, due to the trapezoidal shape it became essential to use the actual stress variation to achieve the required accuracy.

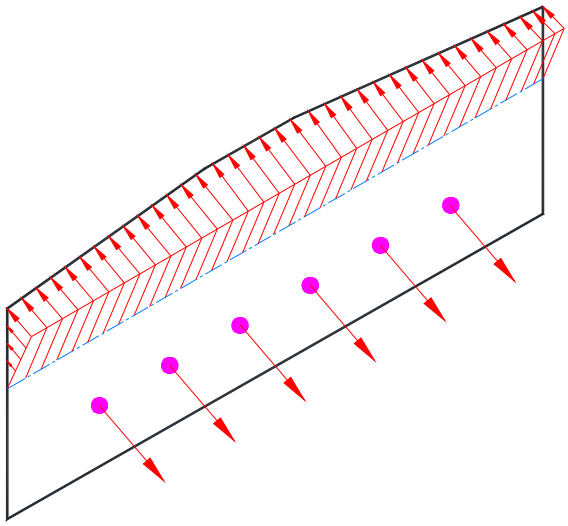

Figure C-1 Strain Diagram of Cracked Section (NTS)

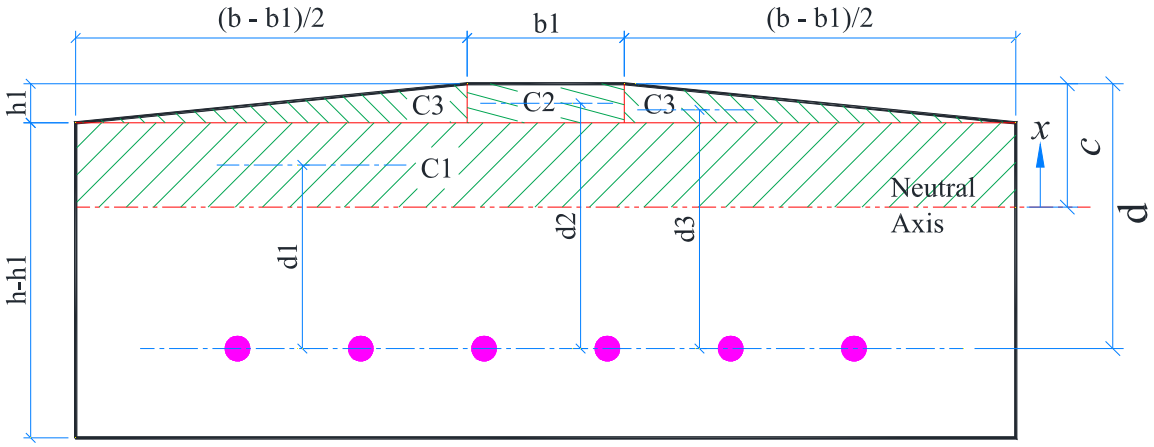

Figure C-2 Cross-Sectional Compression Zone Description

The following formulation is valid for the depth of neutral axis greater than 25.4 mm

$$C1 = \int_0^{c-h1} \{b\ \sigma_c\}\ dx$$

$$d1 = \frac{\int_0^{c-h1} \{(b\ \sigma_c)\ x\ \} dx}{\int_0^{c-h1} \{b\ \sigma_c\}\ dx} + (d - c)$$

$$C2 = \int_{c-h1}^{c} \{b1\ \sigma_c\}\ dx$$

$$d2 = \frac{\int_{c-h1}^{c} \{(b1\ \sigma_c)\ x\}\ dx}{\int_{c-h1}^{c} \{b1\ \sigma_c\ \} dx} + (d - c)$$

$$C3 = 2 \int_{c-h1}^{c} \left\{ \frac{b - b1}{2\ h1} (c - x)\ \sigma_c \right\}\ dx$$

$$d3 = \frac{\int_{c-h1}^{c} \left\{ \left(\frac{b - b1}{2\ h1} (c - x) \sigma_c \right)\ x \right\}\ dx}{\int_{c-h1}^{c} \left\{ \frac{b - b1}{2\ h1} (c - x)\ \sigma_c \right\}\ dx} + (d - c)$$

Total compressive force *C* generated due to external moment is given by

$$C = C1 + C2 + C3$$

Internal moment *M* is given by following equation

$$M = C1 \times d1 + C2 \times d2 + C3 \times d3$$